



Thermo-Elastic Analysis of Internally Cooled Structures Using a Higher Order Theory

Steven M. Arnold
Glenn Research Center, Cleveland, Ohio

Brett A. Bednarczyk
Ohio Aerospace Institute, Brook Park, Ohio

Jacob Aboudi
Tel-Aviv University, Tel-Aviv, Israel

National Aeronautics and
Space Administration

Glenn Research Center

Trade names or manufacturers' names are used in this report for identification only. This usage does not constitute an official endorsement, either expressed or implied, by the National Aeronautics and Space Administration.

Available from

NASA Center for Aerospace Information
7121 Standard Drive
Hanover, MD 21076
Price Code: A05

National Technical Information Service
5285 Port Royal Road
Springfield, VA 22100
Price Code: A05

Available electronically at <http://gltrs.grc.nasa.gov/GLTRS>

Thermo-Elastic Analysis of Internally Cooled Structures Using a Higher Order Theory

Steven M. Arnold
National Aeronautics and Space Administration
Glenn Research Center
Cleveland, Ohio 44135

Brett A. Bednarczyk
Ohio Aerospace Institute
Brook Park, Ohio

Jacob Aboudi
Tel-Aviv University
Tel-Aviv, Israel

Abstract

This paper presents the results of a study on the thermomechanical behavior of internally cooled silicon nitride structures. Silicon nitride is under consideration for elevated temperature aerospace engine applications, and techniques for lowering the operating temperature of structures composed of this material are under development. Lowering the operating temperature provides a large payoff in terms of fatigue life and may be accomplished through the use of thermal barrier coatings (TBC's) and the novel concept of included cooling channels. Herein, an in-depth study is performed on the behavior of a flame-impinged silicon nitride plate with a TBC and internal channels cooled by forced air. The analysis is performed using the higher order theory for functionally graded materials (HOTFGM), which has been developed through NASA Glenn Research Center funding over the past several years. HOTFGM was chosen over the traditional finite element approach as a prelude to an examination of functionally graded silicon nitride structures for which HOTFGM is ideally suited. To accommodate the analysis requirements of the internally cooled plate problem, two crucial enhancements were made to the two-dimensional Cartesian-based version of HOTFGM, namely, incorporation of internal boundary capabilities and incorporation of convective boundary conditions. Results indicate the viability and large benefits of cooling the plate via forced air through cooling channels. Furthermore, cooling can positively impact the stress and displacement fields present in the plate, yielding an additional payoff in terms of fatigue life. Finally, a spin-off capability resulted from inclusion of internal boundaries within HOTFGM; the ability to simulate the thermo-elastic response of structures with curved surfaces. This new capability is demonstrated, and through comparison with an analytical solution, shown to be viable and accurate.

1.0 Introduction

Cooled ceramics are under consideration for high temperature aircraft engine applications. Ceramics offer higher operating temperatures than metals, which are the traditional choices for these applications, but due to ceramics' low thermal conductivity, thermal shock induced cracking can be a problem. By lowering the operating temperature of ceramic components, through both thermal barrier coatings (TBC's) and internal cooling, the driving force for thermal shock can be reduced while the resistance to cracking and fatigue failure can be increased dramatically. One particular ceramic that shows promise as a turbine blade material is silicon nitride (Si_3N_4). Figure 1 provides sample-applied stress vs. life curves for Si_3N_4 . As Fig. 1 shows, a large payoff in fatigue life can be realized by lowering the operating temperature, even by as little as two hundred degrees F [1].

The concept of employing a low thermal conductivity TBC on a hot surface to lower the operating temperature of engine components is well known. Recent work has indicated that including internal cooling channels within ceramic engine components and forcing air through the channels might further reduce component-operating temperatures [2]. A study to evaluate the feasibility and efficacy of internally cooled Si_3N_4 is in progress at NASA Glenn Research Center. An early step in this program involves design, analysis, and testing of a Si_3N_4 plate with internal cooling channels. In addition to the manufacturing and experimental work required to develop this technology, thermo-mechanical analysis of the Si_3N_4 plate is needed to predict stresses that arise in the plate and to aid in the design of the plate to maximize cooling while minimizing resulting thermally induced stresses. Clearly, the plate geometry itself has limited applicability in aircraft engines, but the plate cooling channel analysis will serve as a template for future development of more complex shaped cooled Si_3N_4 components.

In addition, since functional grading of coatings (both thermal and environmental) and possibly of the substrate itself will be investigated in the future, the present thermal and mechanical study of the cooled Si_3N_4 plate will be conducted using a recently developed higher order theory for functionally graded materials, referred to as HOTFGM-2D in the literature [3-7], rather than employing the traditional finite element analysis (FEA) technique. HOTFGM-2D offers a comprehensive approach towards modeling the response of material systems with different microstructural details, including certain advantages not available in standard displacement based finite element analysis techniques, such as: 1) simultaneous satisfaction of displacement and traction continuity conditions between the different sub volumes of the spatially variable microstructure; 2) combined solution of the thermal and mechanical problems; 3) easy variation of cooling channel locations; 4) less mesh sensitivity; and 5) significantly less effort in constructing the required input. The HOTFGM-2D theory is extended herein to permit multiple internal boundaries of the type necessary to model a plate with internal cooling channels and now enables analysis of geometries with arbitrary internal and external boundaries, thus significantly expanding the applicability of the analysis approach to include curved cross-sections.

The paper begins with a brief review of the previously developed higher order theory for functionally graded materials, including a generalization to include boundary cell classifications and convective thermal boundary conditions. Then two applications are addressed: the first described in section 3.1, is that of a flat plate with internal cooling channels and the second, described in section 3.2, is an axisymmetric cylinder subjected to both a thermal gradient and internal pressure.

2.0 Higher Order Theory Review with Boundary Cell Generalization

HOTFGM-2D is based on a geometric model of a heterogeneous composite having finite dimensions in the $x_2 - x_3$ plane and extending to infinity in the x_1 direction, Fig. 2. In the $x_2 - x_3$ plane, the composite is functionally graded by an arbitrary distribution of fibers of arbitrary cross section. It is assumed that the composite may contain one or several "windows", which are merely holes of arbitrary cross section. The loading applied to the composite's external, as well as internal, boundaries (window boundaries) may involve an arbitrary temperature or heat flux distribution, and mechanical effects represented by a combination of surface displacements and/or tractions in the $x_2 - x_3$ plane, and a uniform strain in the x_1 - direction which is equal to zero under plane strain conditions.

The functionally graded microstructure in the $x_2 - x_3$ plane is model by discretizing the heterogeneous material cross-section into N_q and N_r generic cells in the intervals $0 \leq x_2 \leq H$, $0 \leq x_3 \leq L$, respectively. The generic cell (q, r) used to construct the material, highlighted in Fig. 2, consists of four subcells designated by the pair (β, γ) , where each index β, γ take the values 1 or 2, which indicate the relative position of the given subcell along the x_2 and x_3 axis, respectively. The

indices q and r , whose ranges are $q = 1, 2, \dots, N_q$ and $r = 1, 2, \dots, N_r$, identify the generic cell in the $x_2 - x_3$ plane. The dimensions of the generic cell along the x_2 and x_3 axes, $h_1^{(q)}, h_2^{(q)}$ and $l_1^{(r)}, l_2^{(r)}$, can vary in an arbitrary fashion such that

$$H = \sum_{q=1}^{N_q} (h_1^{(q)} + h_2^{(q)}) \quad (1)$$

$$L = \sum_{r=1}^{N_r} (l_1^{(r)} + l_2^{(r)}) \quad (2)$$

Given the applied thermomechanical loading, an approximate solution for the temperature and displacement fields is constructed based on volumetric averaging of the field equations together with the imposition of boundary conditions at the external and internal boundaries and continuity conditions in an average sense between sub volumes used to characterize the material's microstructure. As described briefly in the following (and more thoroughly in references [3-7]), this is accomplished by approximating the temperature and the in-plane displacement fields in each subcell of a generic cell using a quadratic expansion in the local coordinates $\bar{x}_2^{(\beta)}, \bar{x}_3^{(\gamma)}$ centered at the subcell's mid-point. This higher-order representation of the temperature and displacement fields is necessary in order to capture the local effects created by the thermomechanical field gradients, the microstructure of the composite with internal windows, and the finite dimensions in the functionally graded directions. The unknown coefficients associated with each term in the temperature and displacement field expansions are then obtained by constructing systems of equations that satisfy the requirements of a standard boundary-value problem for the given field variable approximations. That is, the heat and equilibrium equations are satisfied in a volumetric sense and the thermal, heat flux, displacement, and traction continuity conditions, within a given cell as well as between a given cell and its adjacent neighbors, are imposed in an average sense.

The volume discretization employed in HOTFGM-2D in the past has allowed one to represent flat rectangular plate geometries composed of different complex types of spatially variable material architectures in sufficient detail. In this work we have extended this previous capability greatly by considering two types of generic cells; namely, the standard internal cell (see insert in Fig. 2) and the new boundary cell (see Fig. 3). An important distinction between the two cells is that an internal cell is neighbored by other generic (internal or boundary (solid material)) cells in both x_2 and x_3 directions; whereas a boundary cell is located on (has as a neighbor) an internal or external boundary and may or may not be composed of a solid material.¹ Consequently, each type of generic cell requires a different analysis for establishing the required equations in the unknown field variables. Also, classification of generic cells into either internal or boundary cells provides a convenient and computationally efficient means for analyzing arbitrary shaped structures with or without, internal cooling passages, cracks, or the like.

Before outlining the basic analysis framework, distinction must be made between the global coordinates x_1, x_2 , and x_3 shown in Fig. 2, and the local in-plane coordinates $\bar{x}_2^{(\beta)}, \bar{x}_3^{(\gamma)}$ used to designate position of each subcell ($\beta\gamma$) within a generic cell (q, r). The local and global coordinate directions designated by the same subscript are parallel to each other and the subcell designation ($\beta\gamma$) identifies the subcell's relative position within a given cell along the global x_2, x_3 coordinates.

¹ Note, when a boundary cell is not composed of a solid material, it is skipped in the analysis portion of the code.

2.1 Thermal Analysis

Let the functionally graded parallelepiped shown in Fig. 2 be subjected to steady state temperature, heat flux or convection distributions on its external and internal surfaces. Under these circumstances, the heat flux, field in the material occupying the subcell $(\beta\gamma)$ of the (q,r) th generic cell in the region $|\bar{x}_2^{(\beta)}| \leq h_\beta^{(q)}/2, |\bar{x}_3^{(\gamma)}| \leq l_\gamma^{(r)}/2$ must satisfy:

$$\frac{\partial q_2^{(\beta\gamma)}}{\partial \bar{x}_2^{(\beta)}} + \frac{\partial q_3^{(\beta\gamma)}}{\partial \bar{x}_3^{(\gamma)}} = 0 \quad (\beta, \gamma = 1, 2) \quad (3)$$

The components $q_i^{(\beta\gamma)}$ of the heat flux (per unit area) vector in the subcell are derived from the temperature field according to the Fourier law,

$$q_i^{(\beta\gamma)} = -k_i^{(\beta\gamma)} \frac{\partial T^{(\beta\gamma)}}{\partial \bar{x}_i^{(\cdot)}} \quad (i = 2, 3; \text{no summation on } i) \quad (4)$$

where $k_i^{(\beta\gamma)}$ are the coefficients of thermal conductivity of the material in the subcell, and $T^{(\beta\gamma)}$ is the spatial temperature distribution in the subcell $(\beta\gamma)$ of the (q,r) th generic cell, measured with respect to a reference temperature T_{ref} , and no summation is implied by repeated Greek letters in the above and henceforth.

The temperature field in the $(\beta\gamma)$ subcell is approximated by a second order expansion in the local coordinates $\bar{x}_2^{(\beta)}, \bar{x}_3^{(\gamma)}$ as follows:

$$T^{(\beta\gamma)} = T_{(00)}^{(\beta\gamma)} + \bar{x}_2^{(\beta)} T_{(10)}^{(\beta\gamma)} + \bar{x}_3^{(\gamma)} T_{(01)}^{(\beta\gamma)} + \frac{1}{2} \left(3\bar{x}_2^{(\beta)^2} - \frac{1}{4} h_\beta^{(q)^2} \right) T_{(20)}^{(\beta\gamma)} + \frac{1}{2} \left(3\bar{x}_3^{(\gamma)^2} - \frac{1}{4} l_\gamma^{(r)^2} \right) T_{(02)}^{(\beta\gamma)} \quad (5)$$

where $T_{(00)}^{(\beta\gamma)}$, which is the temperature at the center of the subcell, and $T_{(mn)}^{(\beta\gamma)}$ ($m, n = 0, 1$, or 2 with $m+n \leq 2$) are unknown coefficients, which are determined from the conditions outlined subsequently.

Given the five unknown quantities associated with each subcell (i.e., $T_{(00)}^{(\beta\gamma)}, \dots, T_{(02)}^{(\beta\gamma)}$) and four subcells within each generic cell, $20 N_q N_r$ unknown quantities must be determined for a composite with N_q and N_r rows and columns of cells containing arbitrary specified materials.

For all cells, these quantities are determined by first satisfying the heat equation (i.e., eqn (4) substituted into eqn (3)), as well as the first and second moment of this equation in each subcell in a volumetric sense in view of the employed temperature field approximation. Subsequently, for **internal generic cells** continuity of the heat flux and temperature is imposed in an average sense at the interfaces separating adjacent subcells, as well as neighboring generic cells.

For **boundary (internal or external) generic cells** however, there are no neighboring cells in certain directions. Consequently, the conditions that reflect the continuity of temperature and heat flux between neighboring generic cells are replaced by the imposed surface boundary conditions on this type of boundary cells. There are three possible types of boundary conditions that can be applied currently to a given internal (window) or external boundary:

1. The heat flux is specified at the boundary B , namely

$$q|_B = q|_{\text{applied}} \quad (6)$$

where $q|_{\text{applied}}$ denotes the applied heat flux at the boundary.

2. The temperature is specified at the boundary B , namely

$$T|_B = T|_{\text{applied}} \quad (7)$$

where $T|_{\text{applied}}$ denotes the applied temperature at the boundary.

3. Convective boundary condition is specified at the boundary B , namely

$$q|_B = h(T|_B - T_\infty) \quad (8)$$

where h is a parameter that varies depending upon the imposed environment (i.e., the fluid beyond the boundary), and T_∞ denotes the environmental temperature.

Fulfillment of these field equations and continuity conditions, together with the imposed thermal boundary conditions on the bounding surfaces, provides the necessary $20 N_q N_r$ unknown coefficients $T_{mn}^{(\beta\gamma)}$ in the temperature field expansion in each $(\beta\gamma)$ subcell. The final form of the system of $20 N_q N_r$ equations is symbolically represented below as:

$$\mathbf{K} \mathbf{T} = \mathbf{t} \quad (9)$$

where the **structural thermal conductivity** matrix \mathbf{K} contains information on the geometry and thermal conductivities of the individual subcells $(\beta\gamma)$ in the $N_q N_r$ cells spanning the x_2 and x_3 directions, the thermal coefficient vector \mathbf{T} contains the unknown coefficients that describe the temperature field in each subcell, i.e.,

$$\mathbf{T} = [\mathbf{T}_{11}^{(11)}, \dots, \mathbf{T}_{N_q N_r}^{(22)}] \quad (10)$$

where

$$\mathbf{T}_{qr}^{(\beta\gamma)} = [T_{(00)}, T_{(10)}, T_{(01)}, T_{(20)}, T_{(02)}]_{qr}^{(\beta\gamma)} \quad (11)$$

and the thermal force vector \mathbf{t} contains information on the boundary conditions. Solution of this eqn. (9) provides the unknown thermal coefficients, which, in turn give the temperature field (see eqn. (5)) in each subcell throughout the solid.

2.2 Mechanical Analysis

Given the temperature field generated by the applied inner and outer surface temperatures, heat fluxes, and/or convective conditions obtained in the preceding section, we proceed to determine the resulting displacement and stress fields. These mechanical fields are induced not only by the temperature distribution but also by arbitrary mechanical loading applied to the surfaces (be they internal or external) of the structure.

The stress field in the subcell $(\beta\gamma)$ of the (q,r) th generic cell must satisfy the equilibrium equations

$$\frac{\partial \sigma_{2j}^{(\beta\gamma)}}{\partial \bar{x}_2^{(\beta)}} + \frac{\partial \sigma_{3j}^{(\beta\gamma)}}{\partial \bar{x}_3^{(\gamma)}} = 0 \quad (j = 2, 3) \quad (12)$$

The components of the stress tensor $\sigma_{ij}^{(\beta\gamma)}$, assuming that the material occupying the subcell $(\beta\gamma)$ of the (q, r) th generic cell is isotropic, are related to the strain components $\epsilon_{ij}^{(\beta\gamma)}$ through the familiar Hooke's law:

$$\sigma_{ij}^{(\beta\gamma)} = \lambda^{(\beta\gamma)} \epsilon_{kk}^{(\beta\gamma)} \delta_{ij} + 2\mu^{(\beta\gamma)} \epsilon_{ij}^{(\beta\gamma)} - \sigma_{ij}^{T(\beta\gamma)} \quad (13)$$

where $\lambda^{(\beta\gamma)}$ and $\mu^{(\beta\gamma)}$ are the Lamé's constants of the material filling the given subcell $(\beta\gamma)$, δ_{ij} is the Kronecker delta and $\sigma_{ij}^{T(\beta\gamma)}$ is the thermal stress consisting of the products of the stiffness tensor components, thermal expansion coefficients, and the temperature change from a reference temperature. The components of the strain tensor in the individual subcells are obtained from the strain-displacement relations.

The displacement field in the subcell $(\beta\gamma)$ of the (q, r) th generic cell is approximated by a second-order expansion in the local coordinates $\bar{x}_2^{(\beta)}$ and $\bar{x}_3^{(\gamma)}$ as follows:

$$u_2^{(\beta\gamma)} = W_{2(00)}^{(\beta\gamma)} + \bar{x}_2^{(\beta)} W_{2(10)}^{(\beta\gamma)} + \bar{x}_3^{(\gamma)} W_{2(01)}^{(\beta\gamma)} + \frac{1}{2} \left(3\bar{x}_2^{(\beta)^2} + \frac{1}{4} h_\beta^{(q)^2} \right) W_{2(20)}^{(\beta\gamma)} + \frac{1}{2} \left(3\bar{x}_3^{(\gamma)^2} + \frac{1}{4} l_\gamma^{(r)^2} \right) W_{2(02)}^{(\beta\gamma)} \quad (14)$$

$$u_3^{(\beta\gamma)} = W_{3(00)}^{(\beta\gamma)} + \bar{x}_2^{(\beta)} W_{3(10)}^{(\beta\gamma)} + \bar{x}_3^{(\gamma)} W_{3(01)}^{(\beta\gamma)} + \frac{1}{2} \left(3\bar{x}_2^{(\beta)^2} + \frac{1}{4} h_\beta^{(q)^2} \right) W_{3(20)}^{(\beta\gamma)} + \frac{1}{2} \left(3\bar{x}_3^{(\gamma)^2} + \frac{1}{4} l_\gamma^{(r)^2} \right) W_{3(02)}^{(\beta\gamma)} \quad (15)$$

where the 40 unknown coefficients $W_{i(00)}^{(\beta\gamma)}$ (which are the displacements at the center of the subcell) and $W_{i(mn)}^{(\beta\gamma)}$ ($i = 2, 3$) (the higher-order terms) must be determined from conditions similar to those employed in the thermal problem. Here, for the mechanical problem, the heat equation is replaced by the two equilibrium equations, and the continuity of tractions and displacements at the various interfaces replaces the continuity of heat fluxes and temperature. Here again we need to distinguish between internal generic cells and boundary cells as was done in the thermal problem. For external boundary cells, the continuity of displacements and tractions is replaced by the applied mechanical boundary conditions.

Application of the above equations and conditions in a volumetric and average sense, respectively, produces a system of $40 N_q N_r$ algebraic equations in the unknown coefficients $W_{i(mn)}^{(\beta\gamma)}$. The final form of this system of equations is symbolically represented by

$$\mathbf{KU} = \mathbf{f} \quad (16)$$

where the structural stiffness matrix \mathbf{K} contains information on the geometry and thermomechanical properties of the individual subcells $(\beta\gamma)$ within the cells comprising the functionally graded material, the displacement coefficient vector \mathbf{U} contains the unknown coefficients that describe the displacement field in each subcell, i.e.,

$$\mathbf{U} = [\mathbf{U}_{11}^{(11)}, \dots, \mathbf{U}_{N_q N_r}^{(22)}] \quad (17)$$

where

$$\mathbf{U}_{qr}^{(\beta\gamma)} = [W_{i(00)}, W_{i(10)}, W_{i(01)}, W_{i(20)}, W_{i(02)}]_{qr}^{(\beta\gamma)} \quad (i = 2, 3) \quad (18)$$

and the mechanical force vector \mathbf{f} contains information on the boundary conditions and the thermal loading effects generated by the temperature distribution.

It should be noted that the above discussion pertains to the plane strain case in which the overall out of plane strain of the composite vanishes, i.e., $\bar{\epsilon}_{11} = 0$. If a generalized plane strain however is considered, $\bar{\epsilon}_{11} \neq 0$ and is not known in advance. In such a case an additional equation must be added to the above system for the determination of the additional unknown out of plane strain. This equation expresses the fact that the overall out of plane stress must be zero, namely, $\bar{\sigma}_{11} = 0$. This stress is given by

$$\bar{\sigma}_{11} = \frac{1}{HL} \sum_{q=1}^{N_q} \sum_{r=1}^{N_r} \sum_{\beta=1}^2 \sum_{\gamma=1}^2 h_{\beta}^{(q)} l_{\gamma}^{(r)} \bar{\sigma}_{11}^{(\beta\gamma)(qr)} \quad (19)$$

where $\bar{\sigma}_{11}^{(\beta\gamma)(qr)}$ is the averaged induced stress in subcell $(\beta\gamma)$, which is located in the generic cell (q,r) . The corresponding displacement in subcell $(\beta\gamma)$ is then taken to be proportional to the out of plane strain, that is,

$$u_1^{(\beta\gamma)} = x_1 \bar{\epsilon}_{11} \quad (20)$$

3.0 Applications

3.1 Internally Cooled Rectangular Plate Problem

The primary problem that will be examined herein involves a long thin plate with ten cooling channels subjected to flame impingement (see Fig. 4). The substrate, which contains the cooling channels, consists of silicon nitride. The plate surface that is subjected to the flame has a thermal barrier coating (TBC) consisting of a mullite bondcoat and a porous zirconia topcoat. As the plate is free to move in the x_1 -direction (out of the plane), the problem can be treated as generalized plane strain. Similarly, since the plate exhibits symmetry in the $x_2 - x_3$ plane (about the x_2 -axis), we need only consider the cross-section geometry shown in Figs. 5 and 6. Figure 5 provides the dimensions for the baseline plate configuration wherein the cooling channels have identical square cross-sections and are equally spaced in the half cross-section. The choice of the cooling channel cross section shape was motivated primarily by ease of analysis at this early juncture in the cooled silicon nitride evaluation program. While in reality the channels will likely be circular or oval in cross-section, the square channels examined in this study are sufficient to evaluate the efficacy of internal cooling and to examine the effects illustrated herein.

Figure 6 indicates the thermal and mechanical boundary conditions imposed in the HOTFGM analysis of the plate. Note that the boundary conditions indicated for the channel nearest to the symmetry boundary were applied to all cooling channels. All mechanical boundary conditions (except symmetry) are traction-free. All thermal boundary conditions (except symmetry) are convective for this "baseline" case. The values employed for the convection coefficients (h) and surrounding air temperatures T_{∞} are admittedly not well known and were taken to be representative. For the external boundary free convection coefficients and the cooling channel forced convection coefficients, text book values were taken from [8] so as to simulate free air flow along a flat plate and forced airflow in a tube, respectively. The values employed for the air temperature inside the cooling channels and at the bottom and free edge ($x_3 = 0.5$ in.) boundaries are estimates provided by experimentalists [9], as is the flame thermal boundary condition far field temperature (T_{∞}). The flame convection coefficient was estimated based on achieving a reasonable TBC surface temperature in early work on the problem [9]. On the portion of the top surface not subjected to flame impingement, the free convection thermal boundary condition was employed along with the linear T_{∞} profile shown in Fig. 6. This profile simulates the decreasing air temperature that would occur as the distance from the flame increases and serves to decrease the discontinuity in the thermal boundary conditions. Note that a discontinuity remains at the edge of the flame as the convection

coefficient changes from $3 \times 10^{-4} \text{ BTU/in}^2 \cdot \text{s} \cdot ^\circ\text{F}$ to $2.04 \times 10^{-6} \text{ BTU/in}^2 \cdot \text{s} \cdot ^\circ\text{F}$, see Fig. 5. Heat transfer due to radiation was assumed to be a higher order effect and was thus neglected.

The temperature dependent material properties for the three plate materials (top coat, bond coat, and substrate) are given in Table 1. The HOTFGM analysis utilizes linear interpolation to determine the material properties between the given temperatures, and this analysis approach (outlined in previous section) involves two steps, both of which are performed during a single execution of the analysis code. First, the thermal problem is solved to determine the temperature field throughout the plate, immediately followed by the mechanical solution that determines the corresponding stress, strain, and displacement fields throughout the plate.

3.1.1 Accuracy Assessment via Grid Refinement

In order to determine the level of geometric refinement necessary to model accurately the response of the internally cooled plate, five subcell grids were constructed. The grids are shown in Fig. 7. The first (Fig. 7a) represents the fewest number of subcells that may be used, given the geometry of the plate and the top surface boundary conditions; as HOTFGM2-D requires the geometry of the material as well as the cooling channels to be described by generic cells, which contain 2×2 subcells. Note that the subcells within a given generic cell may all contain different materials if desired. This least refined grid consists of 8 subcells in the x_2 -direction and 24 subcells in the x_3 -direction. In Fig. 7b, the number of subcells in each direction has been doubled to yield a grid of 16×48 subcells. For Figs. 7c – 7e, the grid increases to 26×74 , 48×136 , and 96×272 subcells, respectively. As required for any consistent mesh refinement study, each refined grid contains the previous less refined (coarser) grid; that is, simply further subdividing the previous grid subcells forms each successive refinement.

Model results in the form of contour plots for the temperature and stress fields in the plate are shown in Figs. 8 – 12 for the five different grid refinements. Note that, in the contour plots, the average value of the quantity (temperature or stress) for each subcell is plotted. Thus, variation of the quantities within the subcells is not depicted. From Fig. 8, it is clear that the 8×24 grid is not sufficiently refined to allow accurate prediction of the temperature field in the plate. Comparing Figs. 8a and b indicates that a significant change in the predicted temperature field has occurred by refining the grid from 8×24 to 16×48 subcells. The maximum average subcell temperature (which occurs in the TBC) is slightly higher in the 16×48 case, but the temperature in the bulk of the plate is significantly lower (typically more than 100°F). Thus it appears that the effect of the coarser 8×24 mesh is to lower the amount of cooling that occurs in the plate.

Comparing Figs. 8b, c, d, and e, it is clear that further refinement does not have a significant effect on the temperature field for the bulk of the plate. Rather, the further refinement mainly affects the temperature in the TBC directly under the flame. The maximum average subcell temperature, which occurs in this region, increases from 2552°F (16×48 , Fig. 8b) to 2638°F (26×74 , Fig. 8c) to 2669°F (48×136 , Fig. 8d) to 2672°F (96×272 , Fig. 8e). This trend can be attributed to the fact that an average temperature is plotted for each subcell. For the less refined grids, subcells are larger, and thus the averaging occurs over a larger area. The subcell results are then “smeared” to a larger extent, and some concentrations are not depicted. As will be shown later, the point-wise temperature at the very top of the plate is actually highest in the case of the 8×24 grid. The minute differences in the temperature field between the 48×136 case and the 96×272 case indicate that, for the thermal problem, the 48×136 grid can be considered sufficiently refined.

Examining the contour plots associated with the extreme grid refinements for the four present stress components² (σ_{11} , σ_{22} , σ_{33} , and σ_{23}), we see that grid refinement has a similar effect on mechanical behavior, see Figs. 9 – 12. In that, greater refinement does not significantly affect the general

² Note σ_{12} and σ_{23} are zero due to the generalized plane strain condition.

character of the stress component fields; rather it affects the magnitude and geometric details of the stress component concentrations. This can be clearly observed by comparing the 8×24 grid results (Fig. 9a – 12a) with the 96×272 grid results (Fig. 9b – 12b). For example, comparing Figs. 9a and 9b indicates that the general geometric nature and magnitude of the out-of-plane (x_1 direction) normal stress, σ_{11} , field are similar given either extreme of grid refinement. However, examining the concentration that occurs near the free edge in the region of the bondcoat/substrate interface indicates that the 8×24 grid is insufficiently refined to capture the fine details of the stress field. The same is true for the remaining normal stress components, the peel stress, σ_{22} , (shown in Fig. 10) and the in-plane (x_3 -direction) normal stress, σ_{33} , (shown in Fig. 11). In the case of the in-plane shear stress, σ_{23} , see Fig. 12, the concentration evident in 12b is so localized that the 8×24 grid (illustrated in Fig. 12a) can hardly begin to capture it. However, as the level of refinement increases, the geometric details and magnitude of the concentration(s) are better approximated. For all stress components only a slight difference is discernable between the results of the 48×136 grid and those of the 96×272 grid. Thus, we conclude that, as was the case for the thermal problem, the 48×136 grid is sufficiently refined to model the mechanical response of the plate as well.

Additional details regarding the effects of grid refinement are observable by plotting the field quantities along certain lines within the plate. Figure 13a illustrates the through thickness temperature (along the x_2 -direction) directly under the flame (i.e., at the center of the plate along the plane of symmetry). Clearly, the plotted temperature field converges rapidly as the level of refinement increases. Note that in x - y plots such as Fig. 13a, the actual values of the field variables are plotted at five points within each subcell. Recall that in the contour plots, only average subcell values were plotted. This explains why, in the contour plot (see Fig. 8), the 8×24 grid appeared to have the lowest maximum TBC temperature, while in Fig. 13a, the 8×24 grid has the highest TBC temperature. Alternatively, Fig. 13b illustrates the horizontal (i.e., along the x_3 -direction) thermal profile along the top and bottom of the plate. Clearly, the temperature field has converged for the 48×136 and 96×272 grids. However, for the 16×48 and 26×74 grids a perturbation is present in the temperature field along the top of the plate in the region of the flame edge. This perturbation is not present in the 48×136 grid results indicating that the further refinement eliminated the problem.

Figure 14a shows the predicted horizontal (x_3 -direction) displacement (u_3) through the thickness of the plate along the free edge. The plotted results show the degree to which the plate expands laterally. Once again it is evident that the response of the 48×136 and 96×272 grids have converged. Figure 14b shows the predicted vertical (x_2 -direction) displacement (u_2) along the top and bottom surfaces of the plate. Note that at the bottom of the plate at the symmetry boundary, a pinned boundary condition was employed (see Fig. 6), making this the origin for displacements. Consequently, the plotted results show the degree to which the plate bends. In this case all grid refinements beyond 8×24 appear to be reasonably well converged.

From the contour plots of the individual stress components (Figs. 9 – 12) it is apparent that stress concentrations occur (as expected) in the region of the bondcoat/substrate interface near the free edge due to dissimilar materials. Figure 15 provides plots of the stress components along the bondcoat/substrate interface (in the x_3 -direction). For the out-of-plane stress (σ_{11}) component, Fig. 15a shows that while the 8×24 grid captures the general nature of the plotted σ_{11} field, jumps occur at the subcell interfaces and the location of the maximum occurs further within the plate (away from the free edge) as compared to the more refined cases. Refinement of the grid improves these shortcomings, and the results from the 48×136 and 96×272 grids are nearly identical. However, small jumps are still present in the 48×136 curve, and the maximum is slightly lower as compared to the 96×272 curve. Note that, at the free edge ($x_3 = 0.50$ in.), σ_{11} is not a traction component and thus should not vanish at this point, as illustrated in Fig. 15a.

The peel stress, σ_{22} , along the bondcoat/substrate interface is similar to the out-of-plane normal stress (σ_{11}) in terms of the effect of grid refinement, as increased refinement leads to increased smoothness of the plotted curve and better representation of the concentration, Fig. 15b. Note that, at the

free edge ($x_3 = 0.50$ in.), the peel stress is again not a traction component and thus is not expected to vanish at this point. In fact, after reaching a low magnitude tensile peak just inside the free-edge, the peel stress becomes highly compressive, which should be beneficial, as it will help prevent delamination at the free edge.

Figure 15c shows the in-plane normal stress, σ_{33} , along the bondcoat/substrate interface. Again, refinement improves the predictions, and the curves coming from the finer grids tend to converge. A large tensile concentration is present just inside the free edge, and in this localized region, there is a significant difference between the results obtained with the 48×136 grid and those obtained with the 96×272 grid. At the free edge ($x_3 = 0.50$ in.), σ_{33} is a traction component and thus should vanish at this point. Clearly, Fig. 15c shows that, while σ_{33} is rapidly decreasing near the free edge, it does not vanish. This is merely due to the fact that boundary conditions are applied in an average sense to each subcell. Thus it is only the average of the in-plane normal stress along the subcell boundary face that should (and does) vanish at the free edge, not the in-plane normal stress at each point within a given subcell (i.e., here the point plotted is at the top of the subcell).

Lastly, the in-plane shear stress, σ_{23} , along the bondcoat/substrate interface is plotted in Fig. 15d. As was the case with σ_{33} , σ_{23} reaches a maximum magnitude just inside the free edge, with the magnitude of the concentration again being somewhat lower for the 48×136 grid as compared to the 96×272 grid. Also, like σ_{33} , σ_{23} is a traction component at the free edge, and thus should vanish. But, as before, since the results shown are along the topmost integration points within the subcells, and boundary conditions are applied in an average sense, the in-plane shear stress shown at the point does not vanish.

Given the results presented in this section, it is reasonable to conclude that the 48×136 grid is sufficiently refined for the purposes of this study. Although this grid refinement does not completely capture the magnitudes of the highest stress concentrations in the plate, the vast majority of the predicted fields are nearly identical to those predicted using the 96×272 grid. Consequently, since the main purpose of this study is to demonstrate new technology and highlight certain effects of internal cooling, the 48×136 grid has been deemed sufficient to 1) locate concentrations, 2) determine the effect of changing the plate configuration or boundary conditions on the concentrations, and 3) demonstrate that the model presented herein is effective.³ The reason that it is desirable to minimize the size of the grid (while maintaining accuracy) is two fold; 1) the creation and alteration of the model input data becomes cumbersome as the grid becomes large and 2) execution time increases significantly with grid size. However, as described in the next section, thanks to a state-of-the-art linear equation solver now implemented within HOTFGM, execution times are no longer a primary driving factor.

3.1.2 Solution Optimization via Sparse Equation Solver

In the version of HOTFGM employed in this study, the number of linear equations that must be solved is five times the number of subcells for the thermal problem and ten times the number of subcells for the mechanical problem (see Section 2). As the number of subcells and number of equations become large, execution times increase as well. Thus, it is desirable to employ the most efficient solution procedure possible. This section outlines the steps taken to improve the efficiency of HOTFGM by employing more efficient linear equation solvers.

The solver originally employed [3] was a subroutine called LEQT1B that is part of the IMSL Fortran library and is available from Visual Numerics, Inc (<http://www.vni.com>). This subroutine uses banded storage to reduce memory requirements and uses L-U decomposition to factor the coefficient matrix. This solver however is known to be quite inefficient for sparse matrices; consequently, to improve the computational efficiency, a sparse solver was sought. This was motivated by the fact that even within

³ Though not shown, comparison to finite element solutions for certain configurations of the silicon nitride plate also indicated the accuracy of HOTFGM and the selected grid.

the bandwidth considered by LEQT1B, the coefficient matrix is typically over 95% sparse for the cases considered in this study. A free sparse solver subroutine known as Y12MAF was thus located. (<http://www.netlib.org/y12m>). This solver proved to be significantly more efficient than LEQT1B, but was limited by the number of equations it could handle. Finally, a state of the art sparse linear equation solver known as UVSS, originally developed by NASA Langley and now distributed and maintained by SolverSoft Co. (<http://www.solversoft.com>) was incorporated. UVSS has proved to be quite efficient and able to handle a large number of equations. Sample execution times for the three linear equation solvers utilized are given in Table 2 for the five levels of grid refinement discussed in the previous section. These execution times are plotted (on a log-log scale) in Fig. 16. For the 26×74 grid, the UVSS solver was 1.898 times faster than the LEQT1B solver and 50 times faster than the Y12MAF solver. Considering the required level of refinement for this study (48×136 subcell grid), UVSS clearly demonstrated its superiority as it was able to solve the problem in slightly more than one minute, whereas Y12MAF was incapable of solving the problem due to the large memory requirements. Compared to LEQT1B, which required almost a week to solve the problem, UVSS represents a significant (four orders of magnitude) improvement in efficiency.

3.1.3 Effect of Cooling Channels and Flame Boundary Condition

As previously stated, it is of significant technological importance to determine the effectiveness of internal cooling channels within a ceramic substrate. That is, do the channels provide a sufficient amount of cooling to justify their presence (considering the added manufacturing expense associated with them as well as any stress concentration they induce)? To this end, we have modeled an identical plate (with the baseline 48×136 subcell grid) with and without cooling channels. The subcell grid geometry is shown in Fig. 17a, with the corresponding temperature and I_1 and J_2 stress invariant profiles for each case being illustrated in Figs. 18a – 20a, respectively. Note that a more narrow scale (than that employed for the cooled plate) was used in Fig. 21 for the case of no cooling channels in order to highlight the fact that, although the temperature gradient is small (approximately 100 °F), one is still present.

In concert with assessing the viability of cooling, we also wish to demonstrate the importance of the assumed thermal boundary conditions by including an additional case for comparison, in which the boundary condition employed for the flame has been altered. That is, the flame thermal boundary condition is taken (in Figs. 18c – 20c) to be a fixed temperature instead of the more realistic convective boundary conditions employed previously (baseline case, Figs. 18b – 20b). Specifically, in this case, the cooling channels are present and active, but now the temperature at the top of the TBC under the flame is prescribed to be 3507 °F. This temperature corresponds to that under the flame for the case of the uncooled plate with convective flame boundary condition (see Fig. 18a).

The temperature results for the fixed temperature flame boundary condition case are shown in Fig. 18c. Note that an increased number of subcells were required in the region of the flame edge to eliminate perturbations in the temperature field similar to those depicted in Fig. 13b. Consequently, the size of the grid increased from 48×136 to 48×166 (see Fig. 17b). The corresponding thermally induced stress fields (i.e., I_1 and J_2) for the cooled convective and cooled fixed temperature boundary condition cases are shown in Figs. 19b, 20b, 19c, and 20c, respectively.

To further highlight the differences among the three cases examined thus far (no cooling channels, baseline cooling channels with the convective flame boundary condition, and cooling channels with the fixed temperature flame boundary condition), detailed x - y plots of the temperature and mechanical fields (stress and displacement components) along specific lines of interest are shown in Figs. 22 – 24. The lines of interest were determined from examination of the various contour plots in Figs. 18 – 20. Examining Figs. 18 and 22, one immediately sees the major impact that internal cooling has on the temperature profile within the plate; in that internal cooling within the substrate itself typically lowers the temperature at a point by approximately 900 °F. Also, by adding the cooling channels (baseline case - convective flame boundary condition cooling), the TBC surface temperature is

significantly reduced. Thus, in the context of convective cooling, the presence of the cooling channels has, in a sense, increased the effectiveness of the TBC and created, even within the substrate, a noticeable though-thickness temperature drop. Alternatively, in the case of a fixed temperature flame boundary condition (Figs. 18c and 20b), the cooling channels still have a significant effect, but the resulting overall plate temperature remains much higher than in the baseline case, as one might expect, particularly when one considers the surface temperature of the TBC. The temperature profile associated with the fixed temperature flame boundary condition is similar in form to that of the baseline case, but because the TBC surface temperature under the flame was forced to remain at 3507 °F, the additional cooling introduced via the channels was unable to affect the surface temperature. Consequently, a much higher temperature field throughout the plate, as well as a higher gradient through the TBC layer itself, is produced. These points are reinforced by Fig. 22b. Note that the larger top to bottom temperature difference present for the fixed flame boundary condition case (as compared to the baseline case) is expected because convective cooling is driven by the difference between the temperature at the convective surface and T_∞ (see eqn. (8)). Hence, since the overall temperature is greater for this case, the temperature difference created by the convective cooling channels is larger, which leads to more cooling. Finally, considering the plate with no cooling channels, the small temperature drop that does occur is mainly through the TBC.

Turning our attention to the mechanical response for the three cases considered, it should be noted that three major effects impact the thermomechanical response. First, the overall plate temperature (the highest being the case with no internal cooling and the lowest being the baseline case) drives the overall thermal expansion of the plate as well as the thermal expansion mismatch between the TBC and the substrate. The overall plate temperature also affects the temperature dependent material properties of the constituents. Second, the thermal gradient within the plate itself causes bending (Fig. 24b) and also sets up a gradient in the material properties. This thermal gradient is largest for the cooled plate with fixed temperature flame boundary condition and lowest for the uncooled plate. Third, the geometric asymmetry of the plate, caused by the off-center cooling channel location and the presence of the TBC, causes additional bending. The degree of geometric asymmetry is identical for the two plate configurations with cooling channels but lower for the uncooled plate. All three of these influences work in concert to bring about the trends that are evident in the results presented.

Examining the I_1 stress invariant ($I_1 = \sigma_{11} + \sigma_{22} + \sigma_{33}$) contour plots given in Fig. 19, one can immediately see the potential regions where brittle damage (crack initiation or void nucleation) could be a problem (i.e., regions of high tensile hydrostatic stress). Obviously, in all three cases this region is located within the substrate near the free edge at the bondcoat/substrate interface, with the uncooled plate having the highest value (73,550 psi) and the baseline (internally cooled) case having the lowest (48,987 psi). Also, it is clear that hydrostatic failure within the bondcoat is not an issue as the entire bondcoat is subjected to compression (with the maximum compressive stress occurring under the flame), as is the top coat and large portions of the substrate. Alternatively, examining the J_2 invariant ($J_2 = \sqrt{\frac{3}{2} S_{ij} S_{ij}}$, where S_{ij} are the deviatoric stress components) contour plots given in Fig. 20, one immediately sees regions where shear induce damage could potentially be a problem. From Fig. 20 we see that the bondcoat layer is subjected to the overall largest magnitudes of J_2 ; with the maximum occurring within the bondcoat near the centerline of the plate (under the flame). Similarly the maximum J_2 within the substrate appears to be underneath the flame. Consequently, given this stress overview, we have displayed the individual stress components as a function of horizontal (x_3) position within the substrate along the bondcoat/substrate interface, see Fig. 23, for all three cases.

From Fig. 23a, it is clear that the largest tensile out-of-plane stress (σ_{11}) occurs just inside the plate near the free edge. Note that the σ_{11} concentration has the greatest magnitude for the fixed temperature flame boundary condition and the smallest magnitude for the plate with no cooling channels. Thus it appears that this tensile concentration is brought about mainly by the thermal gradient (which is largest for the fixed temperature flame boundary condition) rather than the overall plate temperature

(which is highest for the plate with no cooling channels). Alternatively, as suggested previously by Fig. 19a, but not specifically shown, the maximum compressive out-of-plane stress occurs within the bondcoat and is largest for the plate with no cooling and smallest in the cooled convective (baseline) case. This suggests that the overall plate temperature drives the maximum compressive σ_{11} stress.

Figures 23b and contour plots (not shown) of the peel stress (σ_{22}) component illustrate that for all three cases considered, the peel stress is close to zero throughout the plate except in the vicinity of the free edge, as one might expect. Further, as noted previously, the peel stress at the free edge, located at the substrate/bondcoat interface is highly compressive, which may help prevent delamination. The magnitude of the compressive peel stress concentration is greatest for the uncooled plate and smallest for the baseline case and thus appears to be driven by the overall plate temperature. The maximum tensile peel stress at the substrate/bondcoat interface (see Fig. 23b) is also greatest for the uncooled plate. However, although not shown, this local maximum is not the maximum in the entire plate for any of the three cases. For in both cases with cooling channels, the absolute maximum occurs at the upper right corner of the cooling channel closest to the free edge, i.e., point A of Fig. 19c. This concentration is significantly higher for the fixed temperature flame boundary condition as compared to the baseline (convective) case. Alternatively, for the uncooled case, the maximum occurs within the bondcoat at the free edge. Note that the peel stress is a traction component at the substrate/bondcoat interface and is thus continuous (in an average sense) across this interface.

Now considering the in-plane normal stress (σ_{33}) (shown in Fig. 23c) it is clear that, as was the case with the out-of-plane stress (σ_{11}), σ_{33} attains a maximum tensile magnitude in the substrate near the free edge along the substrate/bondcoat interface. Alternatively, as suggested by Fig. 19a but not explicitly shown, the maximum compressive σ_{33} occurs in the bondcoat in the region under the flame. The trend in the magnitudes of both of these stress concentrations appears to be driven by the absolute temperature, as the magnitudes are largest for the plate with no cooling and lowest for the baseline (convective) case. The reduction in the maximum tensile in-plane normal stress (σ_{33}) associated with the introduction of the cooling channels (shown in Fig. 23c) may be of significant importance as this stress component was reduced from 54 ksi (for the uncooled case) to 30 ksi (for the baseline case). Particularly, since the tensile strength of the silicon nitride substrate (at 2552 °F) is 58 ksi [10] the predicted temperature (for the uncooled plate) in this region of the plate is 3418 °F. Alternatively, in the case of cooling the predicted temperature is reduced to 1833°F and consequently the strength should be greater as well.

In-plane shear stress (σ_{23}) results for the three cases considered thus far are illustrated in Fig. 23d, where, similar to the peel stress component, the shear stress is low throughout the plate except near the free edge where a concentration develops at the substrate/bondcoat interface. The magnitude of the concentration is largest for the uncooled plate and smallest for the cooled baseline (convective) case and thus again appears to be driven by the plate's overall temperature. Clearly this large interfacial shear stress represents a potential failure mechanism for the plate that could lead to interfacial delamination, depending on the interfacial bond strength of the substrate/bondcoat interface.

Finally, considering both the horizontal displacement (u_3) at the free edge (Fig. 24a) and the vertical displacement (u_2) along the top and bottom of the plate (Fig. 24b) for all three cases, one can see the manifestation of the influence of temperature (overall magnitude, gradient or profile), geometry (layer configuration and thickness, channel presence and location), and material properties (temperature dependence, mismatch). Given the temperature profiles (overall magnitude and through-thickness gradient) displayed in Fig. 22, one can explain the ordering of the resulting displacement profiles given in Fig. 24. To do this it is important to remember the following key factors:

1. Given the current layered system's asymmetry (wherein the topcoat and bondcoat have higher CTE than the substrate, see Table 1) downward bending would occur even under a uniform temperature field.

2. This bending would increase in proportion to the overall temperature rise.
3. Superposition of a positive through-thickness temperature gradient (i.e., higher temperature in the topcoat, lower temperature in the substrate) would increase bending; whereas a negative through-thickness temperature gradient (lower temperature in the topcoat, higher temperature in the substrate) would decrease bending. This effect is, however, muted by the temperature dependence of the Si_3N_4 elastic modulus (see Table 1), which causes cooler regions to be stiffer and thus offer greater resistance to bending.
4. Introduction of channels within the substrate effectively reduces the substrate's structural stiffness (resistance to bending) and thus increases the amount of overall bending.
5. The vertical location of the channels can either increase or decrease the overall system on bending through the effect of plate asymmetry.

Clearly, the ordering in Fig. 24a is determined by the overall (or average) plate temperature. That is, the plate with no cooling channels is hottest and thus exhibits the greatest amount of lateral expansion (u_3), followed by the cooled fixed temperature flame boundary condition case, and finally by the baseline case, which is coolest. However, the bending profiles (measured by the displacement of the bottom of the plate) in Fig. 24b do not follow this simple trend. That is, based on overall temperature, one would expect the ordering (from least to most bending) to be: baseline, fixed temperature boundary condition, no cooling channels. Based on temperature gradient, this trend would be: no cooling channels, baseline, fixed temperature case and lastly, based solely on geometric considerations, the baseline and fixed temperature cases would be expected to bend more than the uncooled plate. Apparently, the observed trend in bending in Fig 24b is: baseline, no cooling, followed by fixed temperature case.

Given the aforementioned facts, one can explain the observed ordering of the bending results in Fig. 24b in terms of the interactive nature of the three influencing factors. First let us examine the uncooled case, which has almost no through-thickness temperature gradient, but the highest overall temperature. This case exhibited more bending than the cooled (convective) baseline case that had a relatively significant through-thickness temperature gradient. Clearly, the effect of the higher overall temperature in the uncooled plate has dominated the influence of the greater thermal gradient and lower effective substrate stiffness in the baseline case. Next considering similar geometries, i.e., the two cases with cooling channels, one sees the anticipated ordering wherein the case with the larger through-thickness thermal gradient and overall temperature (fixed temperature flame boundary condition) bends significantly more than the baseline convective flame boundary condition case with its smaller gradient and overall temperature. Finally, comparing the fixed temperature flame boundary condition case (which exhibits the most bending) we see that here the effects of the higher thermal gradient coupled with those of the reduced effective substrate stiffness dominate over the influence of the higher overall temperature in the uncooled plate. These results clearly demonstrate the important interaction of temperature, geometry, and material properties and point to the positive impact of reducing the overall temperature through cooling on the plate's deformation behavior.

In summary, this section clearly illustrates the benefits of introducing cooling channels into the plate. The temperature throughout the plate can be significantly reduced, which, as discussed previously, can significantly improve the fatigue life of the plate (or a similar component). But the benefits go further. The presence of the cooling channels also reduces the magnitudes of the stress components (except for the tensile σ_{11} concentration) and displacements. These effects can also be expected to improve the failure and fatigue life characteristics of a cooled plate or similar component. Furthermore, from a modeling viewpoint, the importance of employing realistic thermal boundary conditions (particularly when evaluating the effectiveness of internal cooling) was demonstrated. In that, if a prescribed surface temperature instead of convective boundary conditions is used to model the effect of the flame on the plate, the impact of cooling channels on reducing surface temperatures under the flame is artificially reduced. Consequently, an unrealistically high temperature field throughout the plate, which also leads to greater predicted stresses and displacements, results. As for the effects that contribute to the mechanical behavior of the plate (overall temperature, temperature gradient, geometric asymmetry, and material

properties), the results in this section indicate that the overall temperature is usually the most significant of these factors, with the temperature gradient followed by the degree of plate asymmetry being less important.

3.1.4 Effect of Cooling Channel Location

Here, the effect of moving the cooling channel locations with respect to each other and the plate boundaries is examined. HOTFGM is ideally suited for conducting such parametric studies as 1) the input is considerably more simplistic than that of similar finite element models, and 2) the thermal and mechanical analyses are performed sequentially within a single execution of the code. Hence, employing the HOTFGM analysis code significantly reduces turnaround time for a large number of cases. When defining the allowable cooling channel locations, a geometric constraint was imposed so as to prevent the channels from becoming too close to a plate boundary or each other, thereby avoiding excessive thermal or mechanical gradients from being introduced. A minimum distance of 0.01 inches was used for this purpose.

Horizontal Channel Location

The influence of perturbing the channel positions along the same horizontal line is examined first. Four cases are considered: 1) the baseline, 2) uniformly distributed channels but shifted left, 3) uniformly distributed channels but shifted right, and 4) channel spacing increasing linearly from left to right. Thermal and mechanical contour plots for these cases are provided for comparison in Figs. 25 – 27. Recall that the left boundary (center line) of the plate has symmetric boundary conditions, thus the placement of the left-most cooling channel a distance of 0.005 inches from this boundary actually represents a channel spacing of 0.01 inches. Figures 28 – 30 provide *x-y* plots and a bar chart for the four plate configurations presented in this section.

Comparing the plate temperature field (Figs. 25 and 28) among the four cases, it is clear that the horizontal location of the channels has a noticeable effect. By moving the channels to the left (Fig. 25b), the temperature in the substrate under the flame is reduced. On the bottom surface, at the midpoint of the plate, the temperature is reduced by nearly 100 °F compared to the baseline case (Fig. 25a). Further, the temperature on the plate surface (surface of the topcoat) directly under the flame increases slightly as a result of shifting the channels to the left, as does the temperature at the bondcoat/substrate interface (Fig. 28c). At the free edge of the plate, the temperature is higher than the baseline case by approximately 18 °F when the channels are shifted to the left.

Alternatively, if the channels are shifted to the right (Fig. 25c), the temperature in the plate near the flame increases significantly compared to the baseline case (from 2058 °F to 2123 °F at the bottom surface of the plate directly under the flame), while near the free edge, the temperature decreases slightly. Thus, the results of shifting the channels horizontally indicate that by moving the channels to the left, which is closer to the heat input, the cooling of the plate is improved. Conversely, moving the channels to the right (away from the heat source) is detrimental to the overall cooling of the plate. The exception is near the free edge, where the stress concentrations are highest.

To capitalize on the improved overall cooling provided by the horizontal shift toward the heat source (left), yet diminishing the temperature increase near the free edge, one could employ a linear channel distribution (Fig. 25d). By placing the first two channels close to the heat source, the overall cooling of the plate is improved compared to the baseline case (see Fig. 28). However, by allowing the right-most channel to be positioned closer to the free edge as compared to the uniformly distributed left-shift case (Fig. 25b), the temperature near the free edge is increased only slightly (approximately 1.5 °F) as compared to the baseline case.

Turning our attention to the resulting thermally induced invariant stress profiles (i.e., I_1 and J_2 depicted in Figs. 26 and 27, respectively) one immediately sees how the regions of high hydrostatic tensile stress move with channel placement and how the overall maximum compressive and tensile states

are modified. Note however that the sign of the stress state within a given layer is not fundamentally changed (due to channel placement) from that of the baseline discussed previously. Furthermore, we see that the magnitude of the hydrostatic stress, I_1 , is increased and shifted by moving the channels to the right and decreased by moving the channels to the left. Also, the presence of the cooling channels near the free edge is clearly detrimental in that both I_1 and J_2 stress invariants as well as the σ_{11} component (Fig. 29a) are increased and a large damaging stress concentration arises in the lower half of the plate at the free edge. Similar concentrations also arise internally in regions of the substrate between the channels. Finally, neither the in-plane normal stress, σ_{33} , (Fig. 29c) nor the in-plane shear stress, σ_{23} , (Fig. 29d) are significantly affected by the horizontal placement of the cooling channels.

In Fig. 30 the displacement profile for both the free edge and the top and bottom surface of the plate are illustrated. As mentioned previously, depending on the particular application of a given internally cooled component, the amount of displacement may or may not be of criticality to achieve design performance. With this in mind, Fig. 30 illustrates that the plate with the channels shifted to the right would perform more poorly, as it exhibits the greatest amount of extension and bending. Both the plate with the channels shifted left and the plate with the linear channel spacing exhibit decreased extension in the x_3 -direction yet increased bending compared to the baseline case. Among these three configurations, a trade-off is present between the beneficial effects of the increased cooling and reduced extension and the detrimental effects of the increased thermal gradient and bending. Shifting the channels to the right produces only detrimental effects and suggests that placing cooling channels away from the heat source (near the plate's free edge) should be avoided.

Vertical Channel Location

Next, the influence of altering the vertical position of the cooling channels is examined. As in the previous horizontal location study, contour plots for the comparison of the resulting temperature and stress profiles are shown in Figs. 31 – 33. The positioning of the channels within the plate is most easily seen by examining the temperature profiles given in Fig. 31 wherein again four cases are examined: 1) the baseline (Fig. 31a), 2) the case in which the channels have been moved up toward the TBC layer as far as possible while still maintaining the 0.01 inch minimum distance from the bottom of the TBC layer as discussed previously (Fig. 31b), 3) a configuration in which the channels have been moved as far downward as allowable (Fig. 31c) and 4) a configuration which produced the minimum bending discussed later in this section (shown in Fig. 31d). Obviously, altering the vertical position of the cooling channels affects the temperature field within the plate in a similar (yet less significant) manner than did shifting the horizontal channel position. However, the vertical movement of the channels has the additional effect of changing the through-thickness asymmetry of the plate and thus influencing the bending of the plate as well through this additional asymmetry mechanism. Consequently, as will be shown later in this section, it is possible to determine the vertical location of the channels such that the amount of plate bending is minimized.

Again from Fig. 31, it is clear that moving the channels up toward the flame does lower the overall plate temperature somewhat even though the topcoat temperature increases. For example, at the midpoint of the lower plate surface (beneath the center of the flame), the temperature is reduced by 8.7 °F compared to the baseline case; whereas along the lower surface at the free edge, this reduction is 21.4 °F. Alternatively, by moving the channels down (Fig. 31c), the resulting temperature at these locations is increased by 15.7 °F and 14.0 °F, respectively, as compared to the baseline configuration. Perhaps most interesting is the local increase in temperature that occurs directly under the flame when the channels are moved up (see Fig. 34c). The temperature increase within this region is a result of the fact that the volume of the substrate material into which the heat from the flame can flow has been reduced. However, as evidenced by the lower plate temperature outside this region, heat flow into the cooling channels increases as well. Thus, if the material can withstand the higher local temperature directly under the flame, the configuration shown in Fig. 31b could be beneficial.

Examining the contours of hydrostatic (I_1) and von Mises (J_2) stress in Figs. 32 and 33, one immediately observes that moving the cooling channels upward (toward the heat source), see Figs. 32b and 33b, results in a significant increase in both tensile I_1 and J_2 stress invariants within the substrate material just below the bondcoat. Moving the channels downward (Figs. 32c and 33c) lowers both of these invariant quantities. The maximum tensile hydrostatic state appears always to be in the vicinity of the free edge at the substrate/bondcoat interface. The maximum J_2 invariant is always in the bondcoat layer under the flame; whereas the maximum J_2 within the substrate typically occurs near the free edge at the substrate/bondcoat interface. The only exception is when the channels are moved upward.

Figure 35a indicates that the out-of-plane normal stress (σ_{11}) component concentrations are somewhat increased by moving the cooling channels vertically upward, whereas moving the channels downward has very little effect on this component. Alternatively, the tensile peel stress, σ_{22} , concentration near the free edge is unaffected by vertical channel movement, although the beneficial compressive magnitude at the free edge is significantly increased by moving the channels up (see Fig. 35b). Considering the in-plane normal stress, σ_{33} , distribution it is evident that this component is only slightly affected by moving the channels down, whereas moving the channels up significantly increases the magnitude of this stress component (see Fig. 35c). Similarly, moving the cooling channels up increases the magnitude of the in-plane shear stress, σ_{23} , concentration near the free edge at the bondcoat/substrate interface; whereas moving the channels downward has only a small effect on this σ_{23} component (see Fig. 35d).

Figure 36 shows the displacement results for the cases in which the vertical location of the channels has been altered while maintaining the baseline horizontal positions. As Fig. 36b indicates, moving the channels both up and down results in increased bending of the plate. The fact that both configurations produce more bending than the baseline case seems counterintuitive since from a purely mechanical standpoint resistance to downward bending should be increased by moving the channels up, whereas moving the channels downward should decrease the resistance of the plate to bending. However, one must realize that two competing effects are at work: 1) the through-thickness temperature gradient and 2) the plate asymmetry (due to vertical channel location). Additionally, it must be remembered that the temperature gradient is significantly impacted by the cooling channel placement (asymmetry) in that if the channels are moved upward the through-thickness gradient increases whereas if the channels are moved toward the bottom of the plate the gradient is decreased. Note that the sign of the gradient is always maintained, thus increasing (or decreasing) the gradient only magnifies (or lessens) the downward bending of the plate. Results indicate that the thermal gradient is the more dominant driving force for bending as compared to the plate asymmetry. Consequently, it should be possible to find a vertical channel location that minimizes the induced bending. Figure 36c shows the displacement of the bottom plate surface for five different vertical channel locations. If the deflection of the lower right corner of the plate is used to quantify the amount of plate bending, we see in Fig. 36d that, indeed, a minimum bending configuration exists when the bottom of the cooling channels are located 0.022 inches from the bottom of the plate. Note that this configuration fortuitously is only slightly different from the baseline case and consequently produces only a slight reduction in the amount of bending as compared to the baseline case. This minimum bending study is intended to be an illustrative example, rather than an important design conclusion for the particular internally cooled plate investigated in this study, as optimization considered only vertical channel placement. The influence of combining vertical and horizontal channel placement will be studied in the next section.

Combined Horizontal and Vertical Channel Location

As a final set of illustrations of channel location effects, we examine two cooling channel configurations in which the channels have been shifted both horizontally and vertically. Fig. 37b shows the first configuration in which the channels are shifted as far left and as far up as possible considering the self-imposed 0.01 inch minimum spacing. This configuration represents an attempt to maximize the

overall cooling of the plate. Alternatively, Fig. 37c shows a configuration in which the left-most channel has been placed as far up and to the left as possible, with the remaining channels having their horizontal positions linearly increased in the x_3 -direction. Note, the second channel (from the left) is placed (vertically) in the center of the substrate, while the remaining three channels' vertical positions have been moved towards the bottom of the plate. This configuration represents an attempt to capitalize on the increased cooling associated with placing a cooling channel close to the flame-impinged surface while diminishing some of the negative effects associated with the previous configuration.

As shown in Figs. 37 and 38, the two new channel configurations offer noticeable temperature reductions throughout the plate with the exception of the region above the first channel directly under the flame (the reason behind this local heating was discussed previously). In the first configuration (Fig. 37b), the temperature at the midpoint of the bottom of the plate is reduced by more than 100 °F compared to the baseline case (Fig. 37a). Similarly, as was the case when the channels were just moved left (Figs. 26b and 29a), the magnitude of the out-of-plane normal stress, σ_{11} , concentration near the free edge is also reduced for this configuration (Fig. 41a); even though the magnitude of I_1 (see Fig. 39) and specifically σ_{11} is increased elsewhere in the plate, particularly above the channels and at the free edge. In contrast, for the linearly spaced and vertically arranged channels, the tensile hydrostatic stress maximum is reduced slightly as compared to the baseline case, however now a tensile concentration arises for this configuration near the top left corner of the second cooling channel from the left. This concentration is potentially problematic as this is also an area of high temperature (lower material strength).

The first significant detrimental effect associated with moving the channels up and to the left is in the in-plane normal stress (σ_{33}) field, as the magnitude of the highest σ_{33} concentration (located at the bondcoat/substrate interface near the free edge) is increased noticeably compared to the baseline case (see Fig. 41c). Also, the magnitude of this stress component is increased throughout the region of the substrate located above the cooling channels thereby potentially increasing the probability of failure due to the larger volumetric sampling of flaws. The alternative configuration with linear spacing and vertical arrangement **reduces** the in-plane normal stress near the free edge (as compared to the previous case), but now a concentration arises at the upper right corner of the left-most channel (not shown). Note however, that this new concentration may potentially be more detrimental to the plate than the higher concentration in the plate with the previous arrangement as this new concentration is in a region of higher temperature and thus lower strength.

The in-plane shear stress, σ_{23} , in the plate behaves in a similar manner to that of the σ_{33} component in that the magnitude of stress is increased by moving the channels up and to the left as compared to the baseline configuration. Whereas, for the linear horizontal and vertical channel arrangement, the magnitude decreases somewhat. Once again, a concentration arises at the upper right corner of the left-most cooling channel for this configuration (not shown), but in the case of σ_{23} , the magnitude of this new concentration is not very large. Note that along the bondcoat/substrate interface (Fig. 41d) no real difference is observed in the σ_{23} results.

Figure 42 shows the most significant consequence of locating the cooling channels as far up and to left as possible, in that both displacement components are increased significantly as compared to the baseline case. The amount of bending undergone by the plate is almost doubled compared to the baseline case. As discussed previously, this may or may not be of concern for a particular application. However, recall that if the plate were fixed rather than free and thus unable to bend or extend, the stresses in the plate would be increased, perhaps significantly, due to this channel configuration. As Fig. 42 illustrates, a great deal of the increased bending associated with moving the channels up and left can be eliminated by employing the linearly spaced and vertically arranged cooling channel configuration. Clearly to obtain the best overall design a full thermal-mechanical optimization study (taking into account an appropriate failure criterion) must be undertaken due to the inherent complex thermomechanical coupling present in the problem.

3.2 Modeling Curved Cross-Sections

Now with the introduction of boundary cells, the modeling capability of the higher order micromechanics theory, HOTFGM, has been extended to include arbitrary-shaped structures as well as those containing internal cooling passages. To illustrate this new capability, the thermo-elastic behavior of components with curved cross-sections will be examined. First, the thermo-elastic behavior of a thick-walled cylinder subjected to internal and external pressure and thermal convection loading will be modeled. In this way, the HOTFGM results can be validated against the corresponding analytical solution results derived in the Appendix.

For consistency a cylinder composed of silicon nitride was examined. The temperature independent material properties are given in Table 1 at 77 °F and the remaining required analysis input parameters describing the problem are given in Table 3. The geometry and boundary conditions associated with the cylinder problem are shown in Fig. 43a, while Fig 43b show the differential volume element employed in the analytical solution. The HOTFGM geometric idealization of the cylinder being analyzed is shown in Fig. 44. Due to symmetry considerations, only one quarter of the cylindrical cross-section was actually modeled and analyzed. As Fig. 44 indicates, curved boundaries must be represented with steps, as the current HOTFGM analysis methodology still requires rectangular subcells. The impact of this geometric constraint on the accuracy of the analysis will be discussed and illustrated later.

Accurately reproducing the required cylindrical coordinate boundary conditions in the inherently Cartesian HOTFGM framework is challenging but feasible. Simply applying a normal stress on every boundary face in Fig. 44b is not sufficient, as the actual pressure boundary conditions require a radial stress to be applied, see Fig 43a. Consequently, for use as boundary conditions in HOTFGM, the in-plane stresses in Cartesian coordinates must be related to the in-plane stresses in cylindrical coordinates through the known transformation equations:

$$\begin{aligned}\sigma_2 &= \sigma_r \sin^2(\theta) + \sigma_\theta \cos^2(\theta) + 2\sigma_{r\theta} \sin(\theta)\cos(\theta) \\ \sigma_3 &= \sigma_r \cos^2(\theta) + \sigma_\theta \sin^2(\theta) - 2\sigma_{r\theta} \sin(\theta)\cos(\theta) \\ \sigma_{23} &= (\sigma_r - \sigma_\theta)\sin(\theta)\cos(\theta) + \sigma_{r\theta}(\cos^2(\theta) - \sin^2(\theta))\end{aligned}\tag{22}$$

On the cylinder boundaries, σ_r is the only stress component present, but as eqns. (22) indicate, in general this leads to the imposition of all three Cartesian stress components. In HOTFGM, however, it is not possible to apply all three components on each face of the boundary since only one of the in-plane normal stress components represents a traction on each face. Toward this end, eqn. (22) was used to determine the Cartesian stress components for each boundary subcell face, given the value of σ_r and the value of θ for the midpoint of the boundary subcell face. The shear stress and one of the two normal stresses were then applied as the boundary conditions to simulate the internal and external pressure.

A similar procedure was employed relative to thermal boundary conditions; since applying convection normal to each boundary face in HOTFGM is unrealistic, as the actual heat flux due to convection occurs in the radial direction, not in a given Cartesian direction. However, unlike stress, heat flux is a first-order tensor and thus must obey the applicable transformation equations:

$$\begin{aligned}q_2 &= q_r \sin(\theta) + q_\theta \cos(\theta) \\ q_3 &= q_r \cos(\theta) + q_\theta \sin(\theta)\end{aligned}\tag{23}$$

For the present cylindrical problem, only q_r is present on the boundary and consequently is applied (in the analytical solution) through convection as shown in eqn (A.8) of the appendix. As this equation shows, for convection, the heat flux q is proportional to the convection coefficient h . Thus, we can replace eqns. (23) with,

$$\begin{aligned}h_2 &= h_r \sin(\theta) \\h_3 &= h_r \cos(\theta)\end{aligned}\tag{24}$$

and use these equations to determine the appropriate value of the convection coefficient to apply to each boundary subcell face given the direction of the normal to that face (2-direction or 3-direction); that is, the actual value of the radial convection coefficient for the boundary and the value of θ for the midpoint of the subcell face.

The actual subcell grid geometry for the HOTFGM idealization of the cylindrical problem analyzed is shown in of Fig. 44b. The grid consists of 100 subcells in each direction, but since only 2828 of the total 10,000 subcells are material occupied, the execution of the HOTFGM code is still very rapid. Note that the boundaries located on and along the x_2 and x_3 axes have symmetric boundary conditions imposed, thus the entire cylinder is, in effect, being modeled. Figure 45 shows the temperature field for the cylinder predicted with HOTFGM. Recall that the simulated thermal problem involves a cool internal fluid with a high convection coefficient and a hot external fluid with a lower convection coefficient (see Table 3 and Fig. 43a). Thus, the temperature profile of the cylinder must increase from the inner to outer surface. The temperature field shown in Fig. 45 also shows little angular (θ) dependence (i.e., the temperature remains essentially constant at a particular radial position as the angle changes). Recall that, due to the axisymmetry of the problem, the analytical thermal solution depends only on radial position (see eqn (A.7) of the Appendix).

The analytical and HOTFGM solutions are compared in Fig. 46, where the temperature versus radial position is shown given an angle of approximately 84.5 degrees from horizontal, see Fig. 44b. The value of the radial position of every point along this line was determined from the Cartesian position of the subcell centroid via rotation equations. Note, this line is a sufficient distance from the left boundary ($x_3 = 0$) to avoid any local effects (disturbances) that this boundary might cause. It is clear from Fig. 46 that agreement between HOTFGM and the analytical thermal solution is excellent.

Figure 47 shows individual stress component contour plots resulting from the HOTFGM thermomechanical problem, involving both the applied temperature field and the high internal pressure and lower external pressure (see Table 3 and Fig. 43a). The cylindrical coordinate stress components plotted in Figs. 47b – d were determined via rotation equations, given the Cartesian coordinates of the subcell centroids and the values of the Cartesian coordinate stresses. As was the case with the temperature field, the symmetry of the problem dictates that the resulting stresses should depend only on radial position, not on angular location. The longitudinal (along the long axis of the cylinder) stress field (Fig. 47a) exhibits this angular independence reasonably well, although along the inner surface of the cylinder, the longitudinal stress does not remain completely constant. However, this discrepancy is expected since the mechanical boundary conditions imposed to simulate radial pressure were not absolutely correct as **only one** of the two normal stress components needed to represent perfectly the radial pressure could be applied.

Figure 47b shows the radial stress component in the cylinder as predicted by HOTFGM. Note that the magnitude of this stress is smaller than that of the longitudinal stress, thus smaller variations appear more significant. The basic character, however, of the lack of angular independence is present in the radial stress field given the inaccuracies associated with the application of the pressure boundary conditions being present once again. Similarly, it also appears that the presence of the stair step (subcell corners) along both inner and outer surfaces of the cylinder leads to perturbations in the stress field. The hoop stress (Fig. 47c) appears to be better behaved. Note that the magnitude of the hoop stress is larger than both that of the radial and axial stress, and the inaccuracy at the inner cylinder surface persists. Figure 47d shows (in cylindrical coordinates) the in-plane shear stress field. Once again, from symmetry arguments, the in-plane shear strain, and thus the in-plane shear stress, must be zero. Clearly, from Fig. 47d, this shear stress component is not zero, although it is relatively small throughout most of the cylinder. As before, some deviation occurs at the inner and outer surfaces of the cylinder.

As in the pure thermal case, in Fig. 48 the HOTFGM stress results are compared with the corresponding analytical solution along a given angle (i.e., 84.5 degrees) from the horizontal axis. The overall agreement between the analytical solution and HOTFGM once again is excellent, even though a small deviation does occur in the hoop stress near the inner surface. Note that the analytical solution shear stress plotted in Fig. 48 is identically zero. Clearly, the shear stress coming from HOTFGM is quite close to zero, except near the inner surface. Again, this deviation is expected given the method employed to apply the radial pressure boundary conditions. Note that the deviation of the HOTFGM solution from the analytical solution near the inner surface could increase if the results were plotted along a line that passed through one of the larger perturbations shown in Fig. 47.

It is clear from the above cylindrical analysis example that HOTFGM (although originally developed to model flat plates) with the incorporation of boundary cells can now be used to accurately model components with curved surfaces. Thermal problem solutions for such structures can be considered accurate, even in the vicinity of the curved boundary, whereas mechanical problem solutions can be considered only accurate in general, where in the immediate vicinity of the curved surfaces, **some perturbations should be expected.**

As a final illustrative example, we will consider a technologically important thermal problem with curved surfaces that does not have an exact analytical solution: a hollow airfoil cross-section. The geometry is shown in Fig. 49a, where only the upper half of the airfoil need be analyzed due to the employment of symmetric boundary conditions. The actual subcell grid employed consists of 30×154 subcells and can only be used to perform a thermal analysis as the subcell grid is not sufficiently refined to accurately model the mechanical response of the airfoil. The thermal boundary conditions imposed consist of a convective flame along the flat leading edge boundary with free convection on all other external boundaries. Internally, we consider two convective boundary conditions: free convection to model a hollow airfoil with no internal cooling and forced convection to model a hollow airfoil with internal forced air cooling. The values of the convection coefficient and T_∞ employed for the flame are those used previously, that is, $0.0003 \text{ BTU/in.}^2 \cdot \text{s} \cdot ^\circ\text{F}$ and $3600 ^\circ\text{F}$, respectively. For the free convective boundary conditions, these values are $2.04 \times 10^{-6} \text{ BTU/in.}^2 \cdot \text{s} \cdot ^\circ\text{F}$ and $1292 ^\circ\text{F}$, and for the forced convective boundary conditions these values are $3.87 \times 10^{-5} \text{ BTU/in.}^2 \cdot \text{s} \cdot ^\circ\text{F}$ and $1292 ^\circ\text{F}$. To account for the surface curvature along the stepped boundaries, the convection coefficient values were multiplied by the sine or cosine of the angle formed by the step, depending on whether the face was normal to the x_2 or x_3 direction.

The resulting temperature profile for the case with no internal cooling is shown in Fig. 49b, while the case with internal cooling is shown in Fig. 49c. Clearly, internal cooling has a significant effect, in that the temperature at the airfoil leading edge is reduced from $3228 ^\circ\text{F}$ to $2450 ^\circ\text{F}$ and that at the trailing edge is reduced from $2874 ^\circ\text{F}$ to $1614 ^\circ\text{F}$. Consequently, armed with the current HOTFGM capabilities (i.e., generic boundary cell formulation and convective boundary condition capability) there is no reason that an airfoil with inter-wall cooling channels, like those shown in Fig. 50, could not be modeled as well. Such a study will be the topic of future study as experimental results become available.

4.0 Conclusion

This paper presents a brief summary of a Cartesian-based higher order theory for functionally graded materials which has been extended to include boundary (both internal and external) cells that enables the thermoelastic analysis of arbitrary shaped, actively cooled, structures with spatially varying microstructures in two orthogonal directions. A new convective thermal boundary condition and sparse solver were also added. Both the flat plate and cylinder applications discussed herein were only composed of monolithic rather than functionally graded layers of materials and therefore did not exercise the full capability of the theory. In particular, the viability of introducing cooling channels into a ceramic plate with a thermal barrier coating was examined in detail. It was demonstrated that the temperature

throughout the plate can be significantly reduced by the introduction of **internal cooling channels**, thus significantly improving the fatigue resistance of the plate (or a similar component). But the benefits go further, in that the presence and location of the cooling channels also reduce the magnitudes of the stress components (except for the tensile σ_{11} concentration) and displacement field, which in turn can positively impact the failure and fatigue life characteristics of a cooled plate or similar component. As for the effects that were shown to contribute to the mechanical behavior (deformation) of the plate (overall temperature, temperature gradient, geometric asymmetry, and material properties), the results indicate that the overall temperature is typically the most significant of all factors, with the temperature gradient followed by the degree of plate asymmetry as the next most important factors. Specific observations regarding the influence of cooling hole placement are as follows:

- Channel placement has approximately an order of magnitude less impact on temperature reduction as compared to the existence or nonexistence of cooling channels.
- Moving cooling channels horizontally toward (away from) heat source improves (is detrimental to) the overall cooling of the plate, relative to uniform cooling channel spacing; whereas extension and bending are increased. Grading the horizontal spacing of the cooling channels will increase overall cooling while reducing extension and other detrimental effects such as increased thermal gradient and bending.
- Vertical channel placement has only a slight impact on temperature distribution but can have a noticeable influence on bending and local induced stresses, as two competing effects are at work: i) through thickness temperature gradient and ii) plate asymmetry. A vertical location can be determined that will minimize overall bending.
- Combining both horizontal and vertical channel location movement allows one to balance the objective of maximizing cooling while minimizing all detrimental effects.

Furthermore, two important factors from a modeling viewpoint were also examined in this paper; 1) the importance of imposing realistic thermal boundary conditions (particularly when evaluating the effectiveness of internal cooling) and 2) the degree of required grid refinement. With regard to thermal boundary conditions, it was clearly shown, as expected, that if a prescribed surface temperature were imposed instead of convective boundary conditions to model the effect of the flame on the plate's boundary, the impact of cooling channels on reducing surface temperatures under the flame was artificially reduced. Consequently, an unrealistically high temperature field throughout the plate (which also leads to greater predicted stresses and displacements) would result. Similarly it was shown that the higher order theory does indeed have some sensitivity toward grid refinement, however this mesh sensitivity is not as severe as one might find when using the traditional finite element method.

Finally, due to the new generalized internal and external boundary capabilities, HOTFGM can now be applied to model structures with curved surfaces. This is a significant advance as previously, the Cartesian version of HOTFGM was restricted to simulating the response of flat plates. As an illustration of this new capability, a cylinder subjected to internal and external pressure and convective thermal boundary conditions was modeled and the results compared to an analytical solution. The results indicated that HOTFGM can be used to model the thermomechanical behavior of structures with curved surfaces, however, some perturbations should be expected in the mechanical results in regions near the curved boundaries.

References:

1. Property Characterization Summary for SN-253, Effects of Environment on the Mechanical Behavior of High Performance Ceramics, University of Dayton Research Institute Report, www.udri.udayton.edu/handbook/SN253tot.pdf.
2. Tsuchiya, T.; Furuse, Y.; Yoshino, S.; Chikami, R.; Tsukagoshi, K.; and Mori, M.: Development of Air-Cooled Ceramics Nozzles for a Power Generating Gas Turbine, International Gas Turbine and Aeroengine Congress and Exposition, Houston, TX, ASME, 95-GT-105, pp. 1–9, 1995.
3. Aboudi, J., Pindera, M-J., and Arnold, S.M.: Thermoelastic Theory for the Response of Materials Functionally Graded in Two Directions, *Int. J. Solids and Structures*, Vol. 33, No. 7, 1996, pp. 931–966.
4. Aboudi, J., Pindera, M-J., and Arnold, S.M.: Thermoplasticity Theory for Bidirectionally Functionally Graded Materials, *J. Thermal Stresses*, Vol. 19, 1996, pp. 809–861.
5. Aboudi, J., Pindera, M-J., and Arnold, S.M.: Higher-Order Theory for Functionally Graded Materials, *Composites: Part B (Engineering)*, Vol. 30, No.8, 1999, pp. 777–832.
6. Pindera, M-J., Aboudi, J., and Arnold, S.M.: Higher-Order Theory for the Analysis of Functionally Graded Materials, in *Advanced Multilayered and Fiber-Reinforced Composite*, Y.M. Haddad (Ed.), Kluwer Academic Publishers, The Netherlands, 1998, pp. 111–132.
7. Pindera, M-J., Aboudi, J., and Arnold, S.M.: Thermomechanical Analysis of Functionally Graded Thermal Barrier Coatings with Different Microstructural Scales, *J. American Ceramics Society*, Vol. 81, No. 6, 1998, pp.1525–36.
8. Rohsenow, W.M., Hartnett, J.P., and Gani, E.N. (eds.): *Handbook of Heat Transfer Fundamentals*. McGraw-Hill: New York, 1985.
9. Bhatt, R.T., Private Communication, NASA Glenn Research Center, 1999.
10. Battelle, Engineering Property Data on Selected Ceramics Vol. I, Nitrides, MCIC-HB-07, 1981.
11. Richardson, D.W. (Ed.), *Modern Ceramic Engineering*, Marcel Dekker, Inc., NY, 1982.
12. Battelle, Engineering Property Data on Selected Ceramics, Vol. III, Single Oxides, MCIC-HB-07, 1981.

Appendix: Thermal/Mechanical Analytical Solution for Thick-Walled Cylinder

The analytical solution for the cylinder depicted in Fig. 43a is constructed in two steps. First, the thermal problem is solved, and then knowing the resulting temperature field distribution throughout the cylinder, the mechanical problem is solved. The problem is axisymmetric, and the cylinder is assumed to be infinitely long in the out of plane (z -coordinate) direction.

Thermal Analysis

To begin the thermal analysis, consider Fourier's Law of heat conduction,

$$q_r = -k \frac{dT(r)}{dr} \quad (\text{A.1})$$

where q_r is the radial component of heat flux per unit area at a point in the cylinder, k is the thermal conductivity of the cylinder material, and $T(r)$ is the radially-dependent temperature. No other heat flux component is present as the problem is axisymmetric (no variation of temperature in the circumferential direction) and the temperature is assumed constant along the length of the cylinder. To obtain the total radial heat flow at a particular radial location, Q_r , we simply multiply q_r by the area over which the heat flux occurs;

$$Q_r = -2\pi r l k \frac{dT(r)}{dr} \quad (\text{A.2})$$

where l is the length of the cylinder. The governing differential equation for the thermal problem is obtained by considering the differential volume element shown in Fig. 43b; wherein since the problem involves steady-state heat flow, the total heat flow in and out of the differential element must be balanced, that is:

$$Q_r^{in} = Q_r^{out} \quad (\text{A.3})$$

The total heat flow in and out of the differential element can be written in terms of the total heat flow at the element midpoint and the radial rate of change of the total heat flow,

$$Q_r^{in} = Q_r - \frac{dQ_r}{dr} \frac{dr}{2}, \quad Q_r^{out} = Q_r + \frac{dQ_r}{dr} \frac{dr}{2} \quad (\text{A.4})$$

Substituting these expressions into eqn. (A.3) yields,

$$\frac{dQ_r}{dr} = 0 \quad (\text{A.5})$$

Substituting eqn. (A.2) into eqn. (A.5) yields the governing differential equation for the thermal problem:

$$\frac{d}{dr} \left(r \frac{dT(r)}{dr} \right) = 0 \quad (\text{A.6})$$

Upon integration we obtain the radial temperature distribution,

$$T(r) = c_1 \ln(r) + c_2 \quad (\text{A.7})$$

The thermal boundary conditions for the problem are convective at both the inner and outer surfaces of the cylinder. The general equation for this type of boundary condition is,

$$q = h(T_s - T_\infty) \quad (\text{A.8})$$

where h is the convection coefficient of the fluid beyond the boundary, T_s is the surface temperature at the boundary, and T_∞ is the temperature of the fluid beyond the boundary. Equation (A.8) is applied to the inner and outer boundaries of the cylinder such that the total heat flow at the inner and outer boundaries are:

$$Q_r(r=r_i) = -2\pi r_i h_i l [T(r_i) - T_i] \quad (\text{A.9})$$

$$Q_r(r=r_o) = 2\pi r_o h_o l [T(r_o) - T_o] \quad (\text{A.10})$$

where the subscripts i and o refer to inner and outer, respectively. Note that the sign of the boundary condition at the inner surface, (A.9), is reversed as the normal to this surface is negative. Utilizing eqn. (A.2) and (A.7) in combination with eqns. (A.9) and (A.10) the two constants of integration can be obtained; they are,

$$c_1 = \frac{T_i - T_o}{\ln(r_i/r_o) - k(1/r_i h_i + 1/r_o h_o)} \quad (\text{A.11})$$

$$c_2 = \frac{T_i - T_o}{\ln(r_i/r_o) - k(1/r_i h_i + 1/r_o h_o)} \left(\frac{k}{r_i h_i} - \ln(r_i) \right) + T_i \quad (\text{A.12})$$

Mechanical Analysis

Assuming elastic, isotropic material behavior the corresponding constitutive equations (in cylindrical coordinates) are:

$$\begin{bmatrix} \sigma_r \\ \sigma_\theta \\ \sigma_z \end{bmatrix} = \frac{E}{(1+\nu)(1-2\nu)} \begin{bmatrix} (1-\nu) & \nu & \nu \\ \nu & (1-\nu) & \nu \\ \nu & \nu & (1-\nu) \end{bmatrix} \begin{bmatrix} \epsilon_r - \alpha \Delta T(r) \\ \epsilon_\theta - \alpha \Delta T(r) \\ \epsilon_z^0 - \alpha \Delta T(r) \end{bmatrix} \quad (\text{A.13})$$

where, ϵ_i are the total strain components, σ_i are the stress components, $\Delta T(r)$ is the temperature change from a reference temperature, and α , E , and ν are the classic elastic material properties (i.e., coefficient of thermal expansion, elastic modulus, and Poisson ratio, respectively). The problem is treated as generalized plane strain, where ϵ_z^0 is the known uniform longitudinal strain throughout the cylinder. Consequently,

$$\sigma_r = Q_1 \epsilon_r + Q_2 \epsilon_\theta + Q_2 \epsilon_z^0 - \Gamma \Delta T(r) \quad (\text{A.14})$$

$$\sigma_\theta = Q_2 \epsilon_r + Q_1 \epsilon_\theta + Q_2 \epsilon_z^0 - \Gamma \Delta T(r) \quad (\text{A.15})$$

where,

$$Q_1 = \frac{E(1-\nu)}{(1+\nu)(1-2\nu)}, \quad Q_2 = \frac{E\nu}{(1+\nu)(1-2\nu)}, \quad \Gamma = \frac{E\alpha}{(1-2\nu)} \quad (\text{A.16})$$

The known cylindrical kinematic equations are:

$$\epsilon_r = \frac{du}{dr}, \quad \epsilon_\theta = \frac{u}{r}, \quad \epsilon_z = \frac{dw}{dz} \quad (\text{A.17})$$

where u and w are the radial and longitudinal components of displacement, respectively. Since the longitudinal strain is known, the last equation in (A.17) is not needed. Combining eqns. (A.14) – (A.17)

and substituting the resulting expressions for the radial and tangential stress components into the equation of equilibrium,

$$\frac{d\sigma_r}{dr} + \frac{\sigma_r - \sigma_\theta}{r} = 0 \quad (\text{A.18})$$

yields the following governing differential equation for the mechanical problem:

$$\frac{d^2u}{dr^2} + \frac{1}{r} \frac{du}{dr} - \frac{u}{r^2} - \frac{\Gamma}{Q_1} \frac{d}{dr} [\Delta T(r)] = 0 \quad (\text{A.19})$$

Equation (A.19) can then be rearranged to yield,

$$\frac{d}{dr} \left[\frac{1}{r} \frac{d(ru)}{dr} \right] = \frac{\Gamma}{Q_1} \frac{d}{dr} [\Delta T(r)] \quad (\text{A.20})$$

which can be integrated directly. The resulting expression for the radial displacement is,

$$u(r) = \frac{\Gamma}{Q_1} \frac{1}{r} \int_{r_i}^r \Delta T(r) r dr + c_3 r + \frac{c_4}{r} \quad (\text{A.21})$$

Note that the integral appearing in eqn. (A.21) can be evaluated given the solution to the thermal problem, eqn. (A.7), and the fact that $\Delta T(r) = T(r) - T_{ref}$, where T_{ref} is a reference temperature. Evaluating the integral, and assigning a function, $F_1(r)$, to represent the integral yields,

$$F_1(r) = \int_{r_i}^r \Delta T(r) r dr = \frac{r^2}{2} \left[c_1 \ln(r) - \frac{c_1}{2} + c_2 - T_{ref} \right] - \frac{r_i^2}{2} \left[c_1 \ln(r_i) - \frac{c_1}{2} + c_2 - T_{ref} \right] \quad (\text{A.22})$$

In order to determine the constants of integration appearing in eqn. (A.21), the mechanical boundary conditions must be applied to the cylinder, that is

$$\sigma_r(r = r_i) = -P_i, \quad \sigma_r(r = r_o) = -P_o \quad (\text{A.23})$$

Consequently, substituting eqn. (A.21) into eqn. (A.17) and the results into eqn. (A.14) followed by eqn. (A.23) the two constants of integration can be determined and they are:

$$c_4 = \frac{-\left(1 - \frac{Q_2}{Q_1}\right) \frac{\Gamma}{r_o^2} F_1(r_o) + P_o - P_i}{(Q_1 - Q_2) \left(\frac{1}{r_o^2} - \frac{1}{r_i^2} \right)} \quad (\text{A.24})$$

$$c_3 = \frac{-Q_2 \epsilon_z^0 - P_i + \frac{c_4}{r_i^2} (Q_1 - Q_2)}{Q_1 + Q_2} \quad (\text{A.25})$$

Finally, the uniform longitudinal strain, ϵ_z^0 , can be determined by imposing the constraint that the average axial stress, $\bar{\sigma}_z$, must vanish, that is:

$$\bar{\sigma}_z = \frac{1}{\pi(r_o^2 - r_i^2)} \int_0^{2\pi} \int_{r_i}^{r_o} \sigma_z(r) r dr d\theta = 0 \quad (\text{A.26})$$

The expression for $\sigma_z(r)$ is obtained from the third of eqns. (A.13) wherein ε_r and ε_θ are eliminated by substituting into eqn. (A.17) the solution for the radial displacement given in eqn. (A.21). The radial integration in eqn (A.26) can then be performed, and the resulting equation can be solved for ε_z^0 . This procedure yields,

$$\varepsilon_z^0 = \frac{2\nu}{E} \left[\frac{c_4}{r_i^2} (Q_1 - Q_2) - P_i \right] - \frac{2F_1(r_o)}{E(r_o^2 - r_i^2)} \left[-2\Gamma\nu - E\alpha + \frac{\Gamma\nu}{Q_1} (Q_1 + Q_2) \right] \quad (\text{A.27})$$

Thus, given the thermal and mechanical boundary conditions, the uniform ε_z^0 that results in the vanishing of the average longitudinal stress is known.

Table 1: Material Properties.

Material	T (°F)	E (psi)	ν	α ($10^{-6}/^{\circ}\text{F}$)	K (BTU/in·s·°F)
Silicon	77	4.35×10^7	0.22	1.83	4.01×10^{-4}
Nitride [10]	2552	3.63×10^7	0.19	1.83	1.61×10^{-4}
Mullite [11]	77	2.10×10^7	0.20	2.94	7.84×10^{-5}
	2552	2.10×10^7	0.20	2.94	5.04×10^{-5}
Porous	77	3.63×10^2	0.25	6.25	2.68×10^{-6}
Zirconia [12]	2552	3.63×10^2	0.25	6.25	6.69×10^{-6}

Table 2: Execution times (in seconds) for the different linear equation solvers.

N_{β}	N_{γ}	Number of Subcells	LEQT1B	Y12MAF	UVSS
8	24	192	140	0.74	0.44
16	48	768	3,162	21.0	2.07
26	74	1,924	16,149	424	8.51
48	136	6,528	587,823	—	69.23
96	272	26,112	—	—	652

Table 3: Cylinder parameters and dimensions.

Parameter	Value
r_o	1 in.
r_i	0.8 in.
T_o	3600 °F
T_i	70 °F
T_{ref}	70 °F
h_o	0.0003 BTU/in. ² · s · °F
h_i	0.0385 BTU/in. ² · s · °F
P_o	1000 psi
P_i	10,000 psi

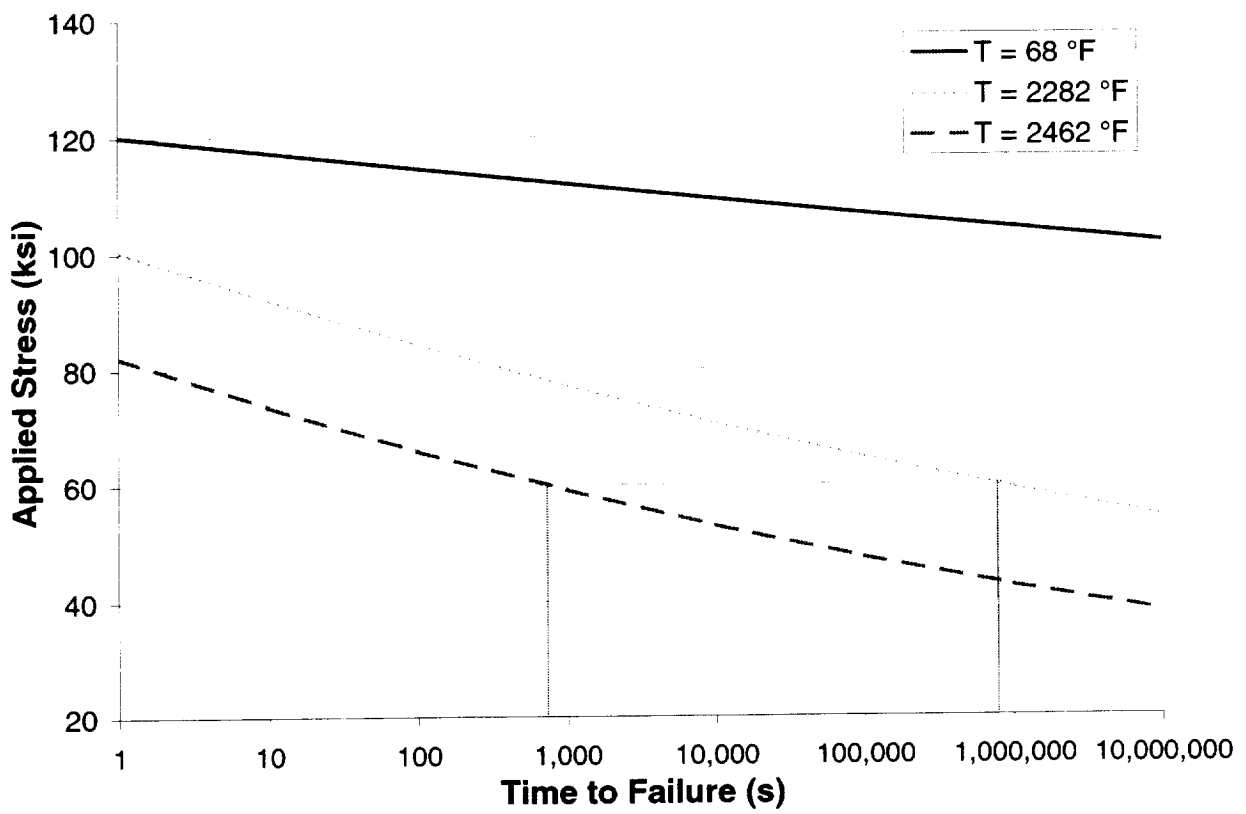


Figure 1: Sample applied stress vs. life curves for Si_3N_4 [1].

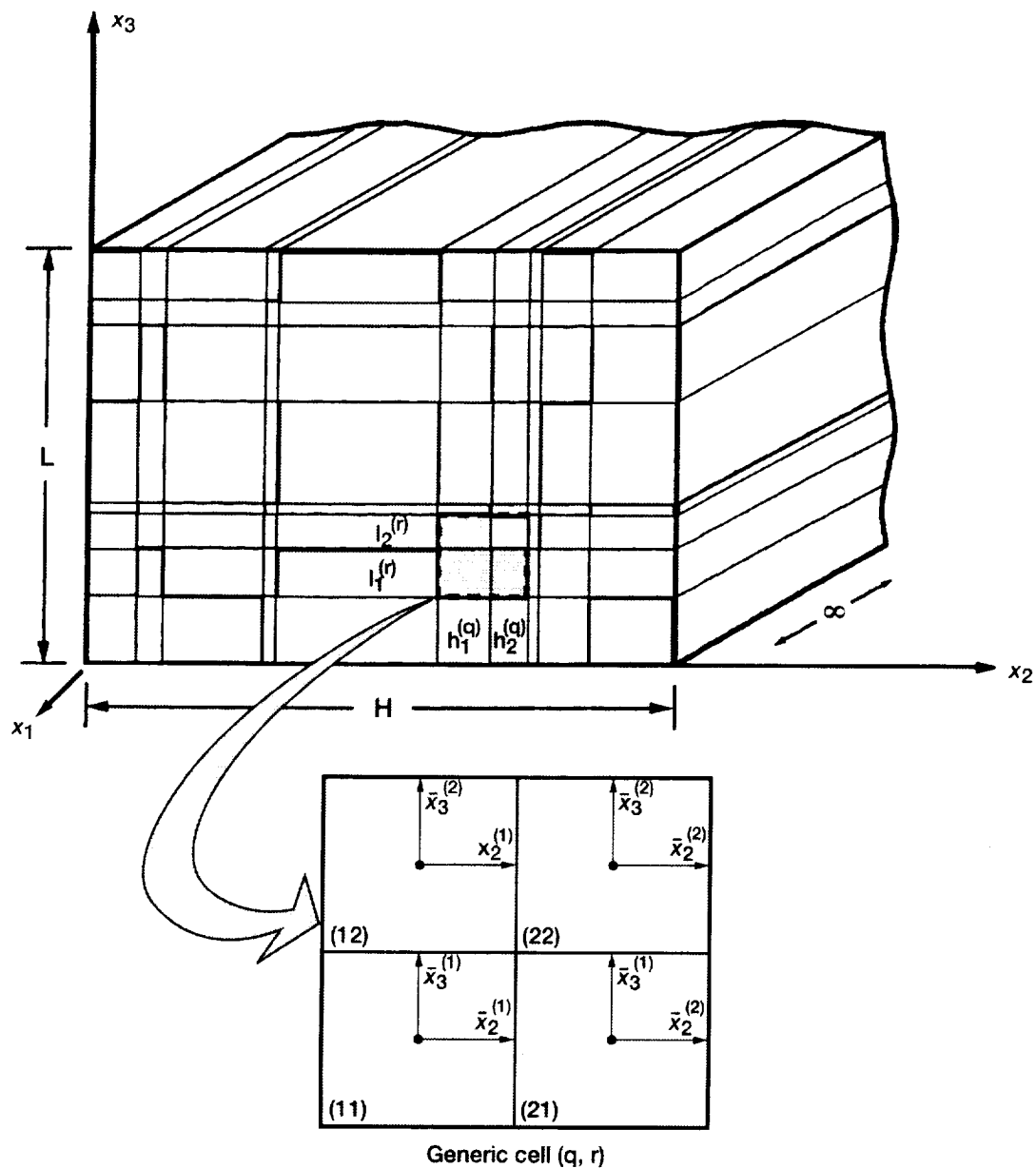


Figure 2: A geometric model of a heterogeneous graded material in the $x_2 - x_3$ plane illustrating the volume discretization employed in HOTFGM-2D.

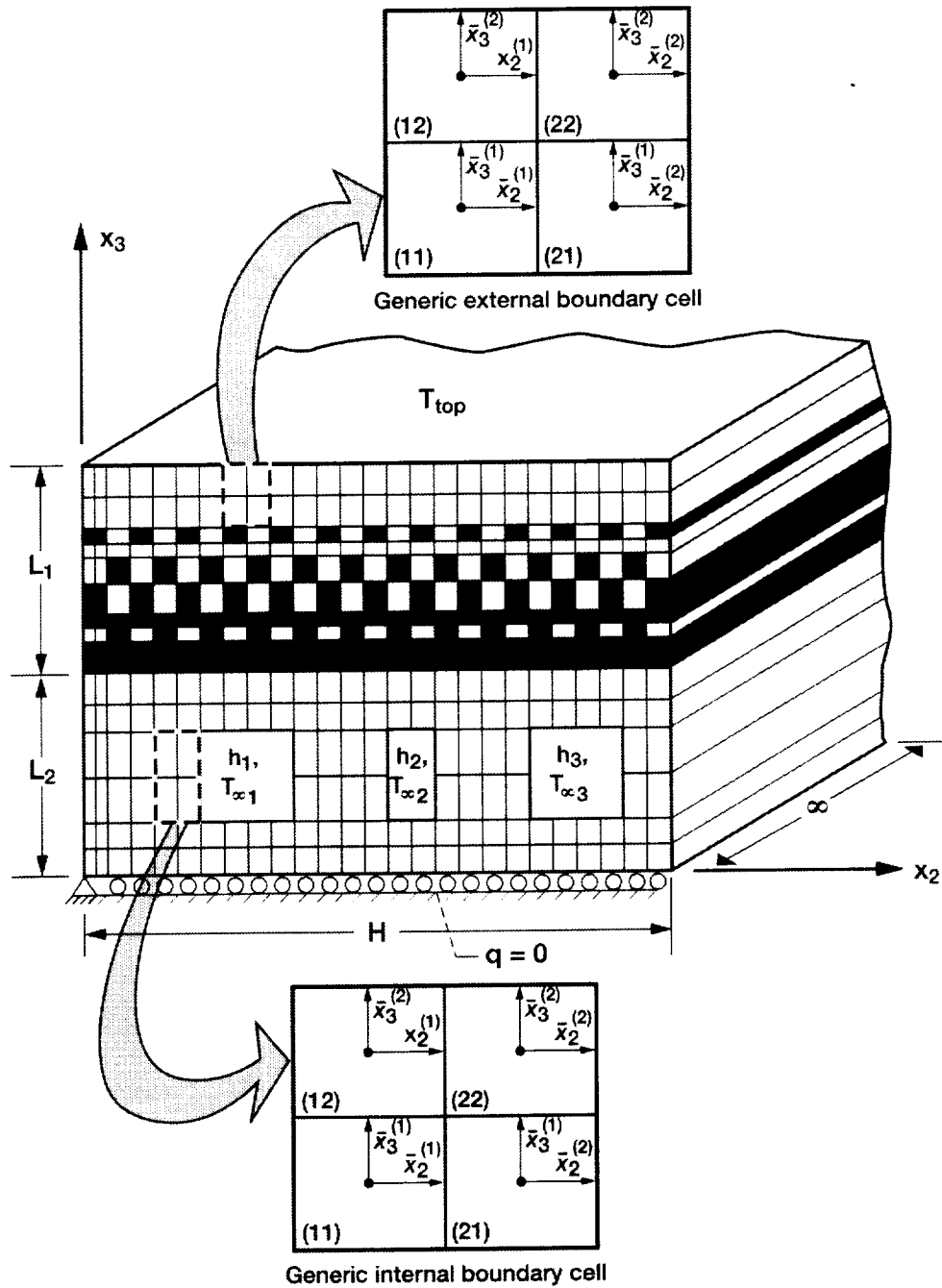


Figure 3: Illustration of the generic internal and external boundary cells given a functionally graded (region L_1 by H) internally cooled plate.

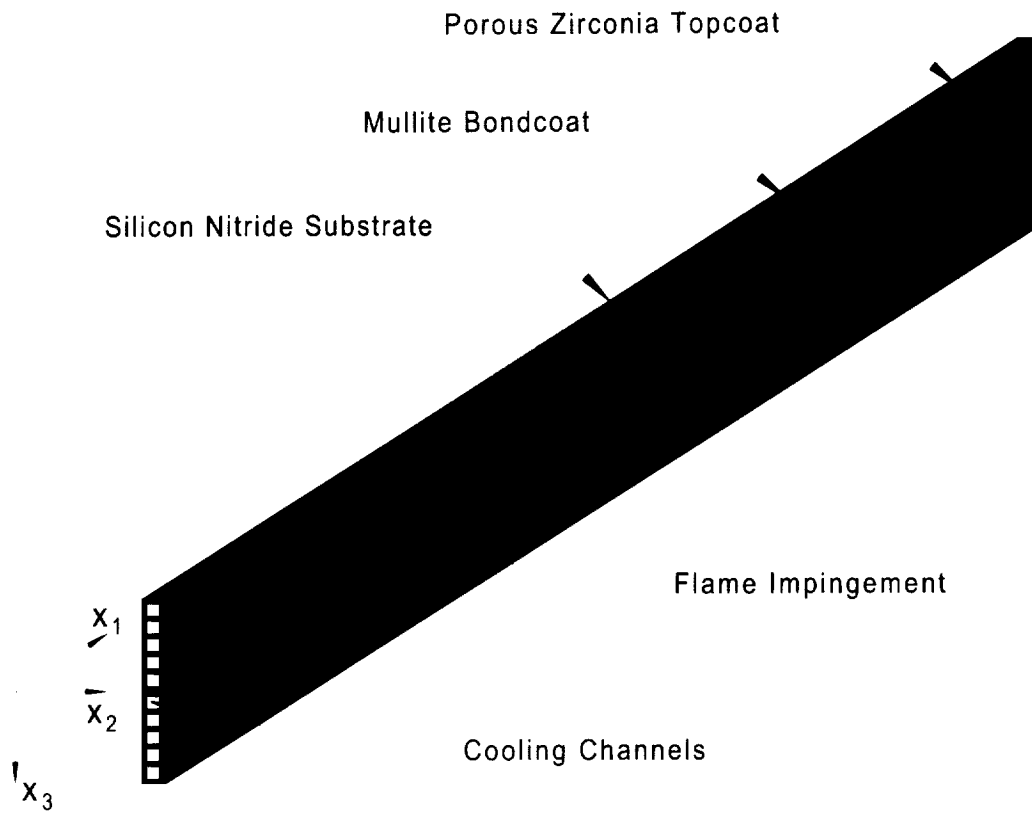


Figure 4: Cooled plate overall geometry.

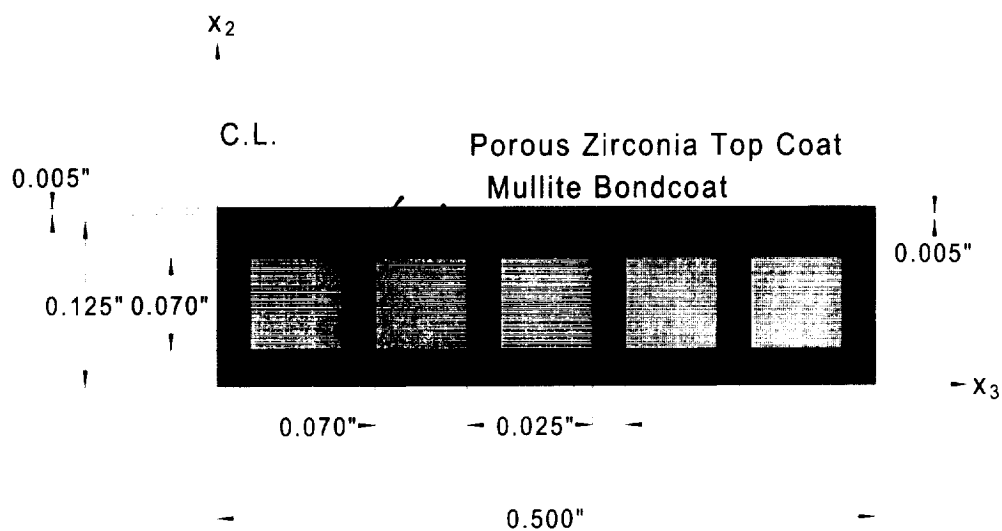


Fig. 5: Cooled plate dimensions.

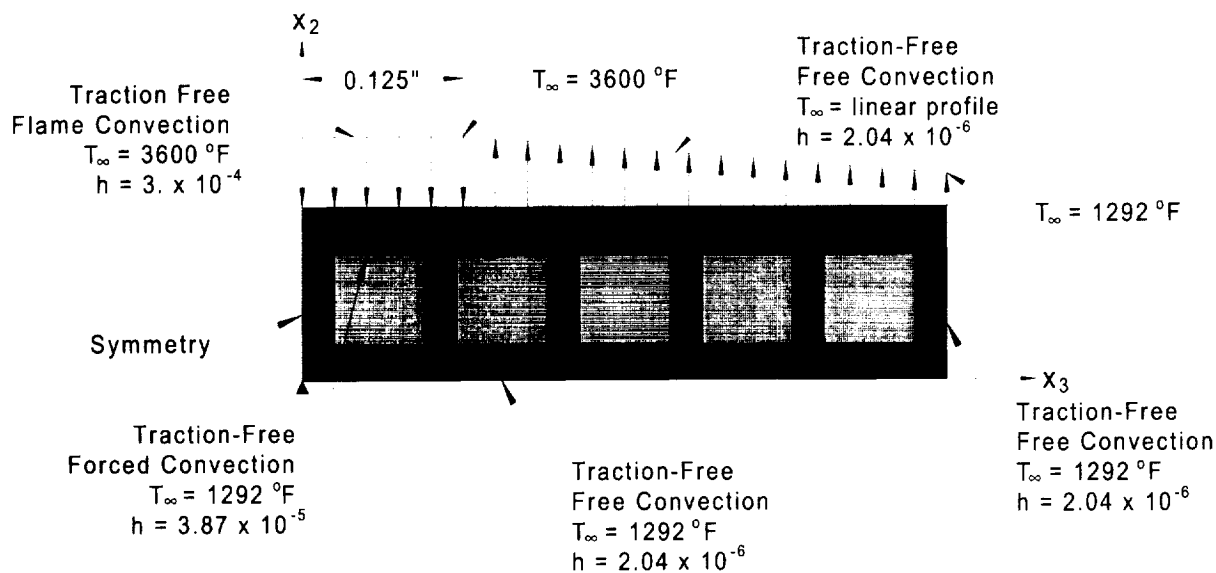


Figure 6: Cooled plate boundary conditions. Note: units for h are $\text{BTU}/(\text{in}^2 \text{ s } ^{\circ}\text{F})$.

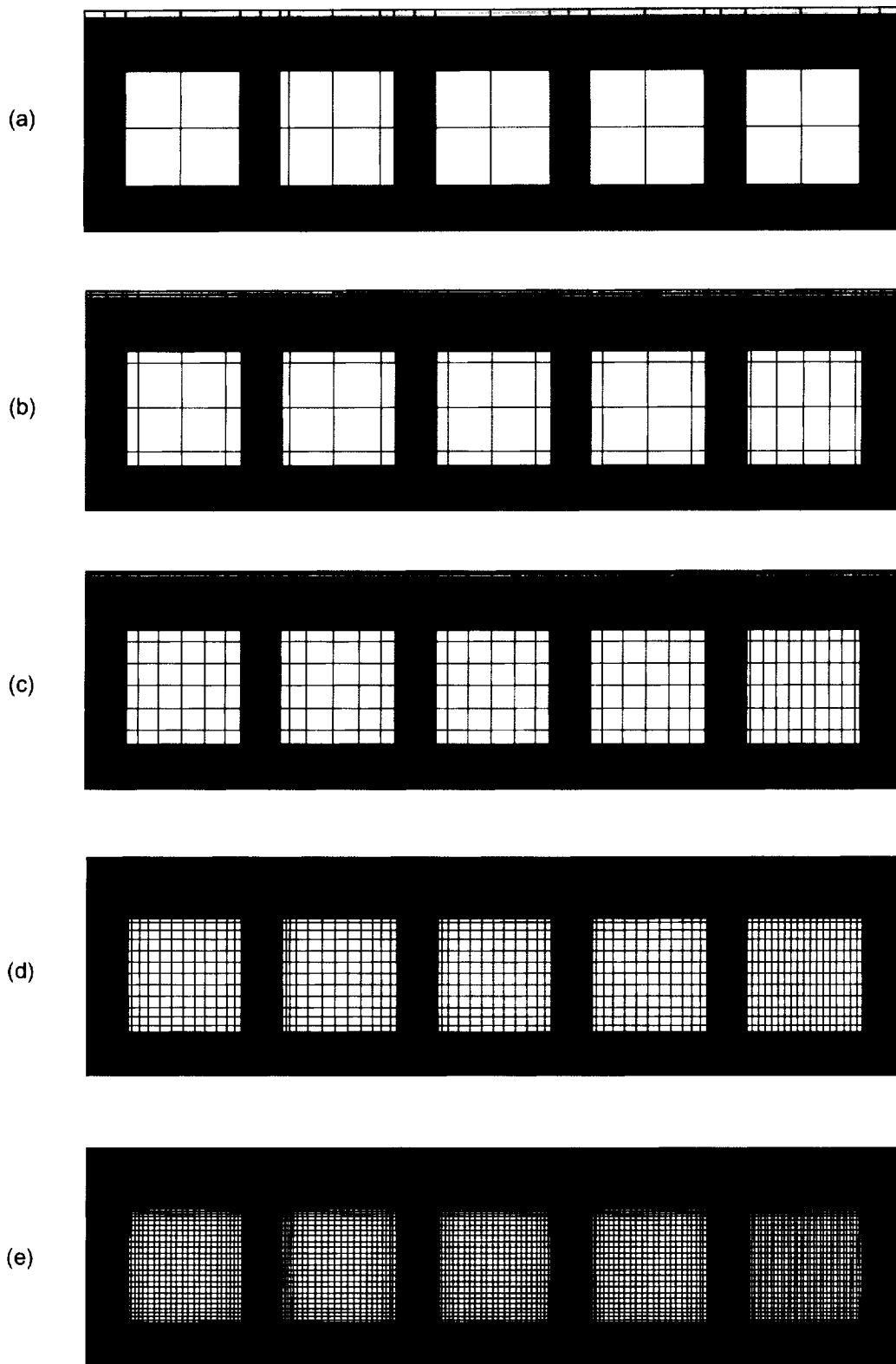


Figure 7: Five levels of subcell grid refinement: (a) 8x24, (b) 16x48, (c) 26x74, (d) 48x136, (e) 96x272.

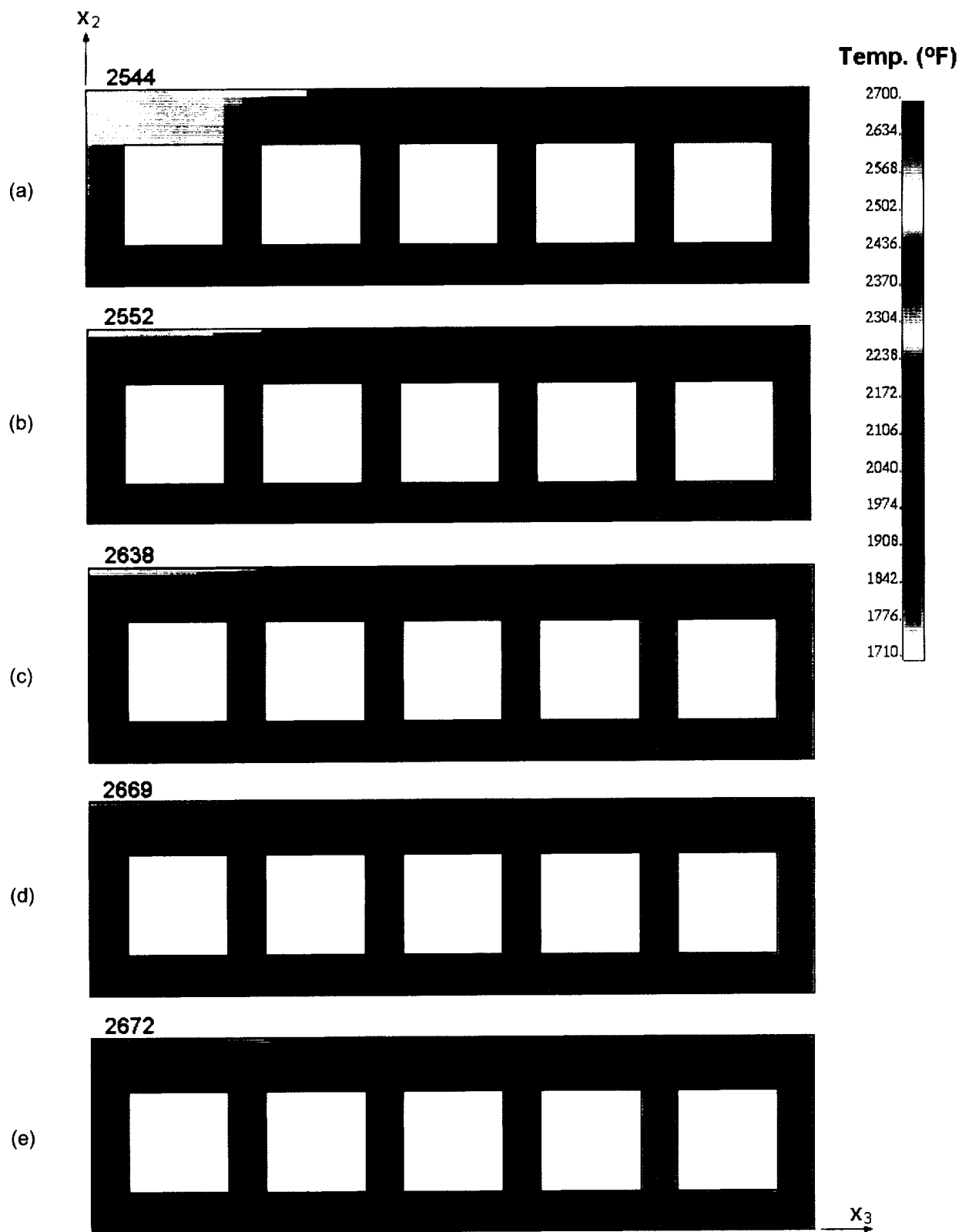


Figure 8: Temperature fields for the different levels of grid refinement. (a) 8x24, (b) 16x48, (c) 26x74, (d) 48x136, (e) 96x272.

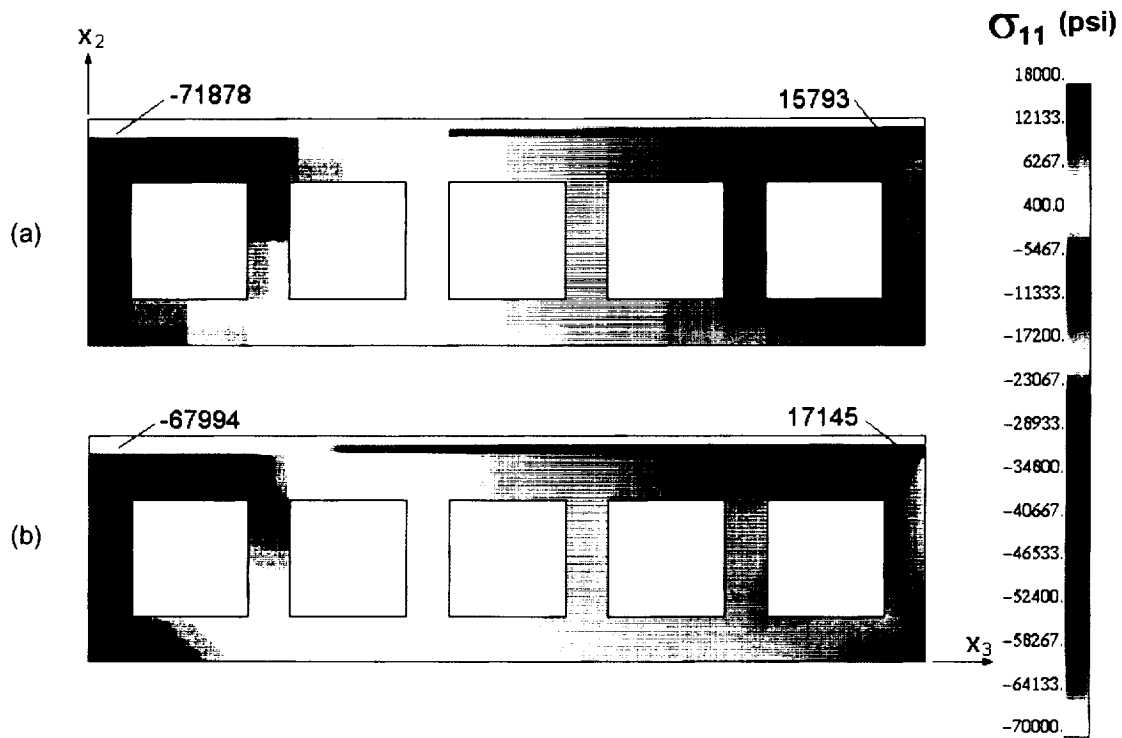


Figure 9: Out of plane stress, σ_{11} , for the: (a) least and (b) most refined grids.

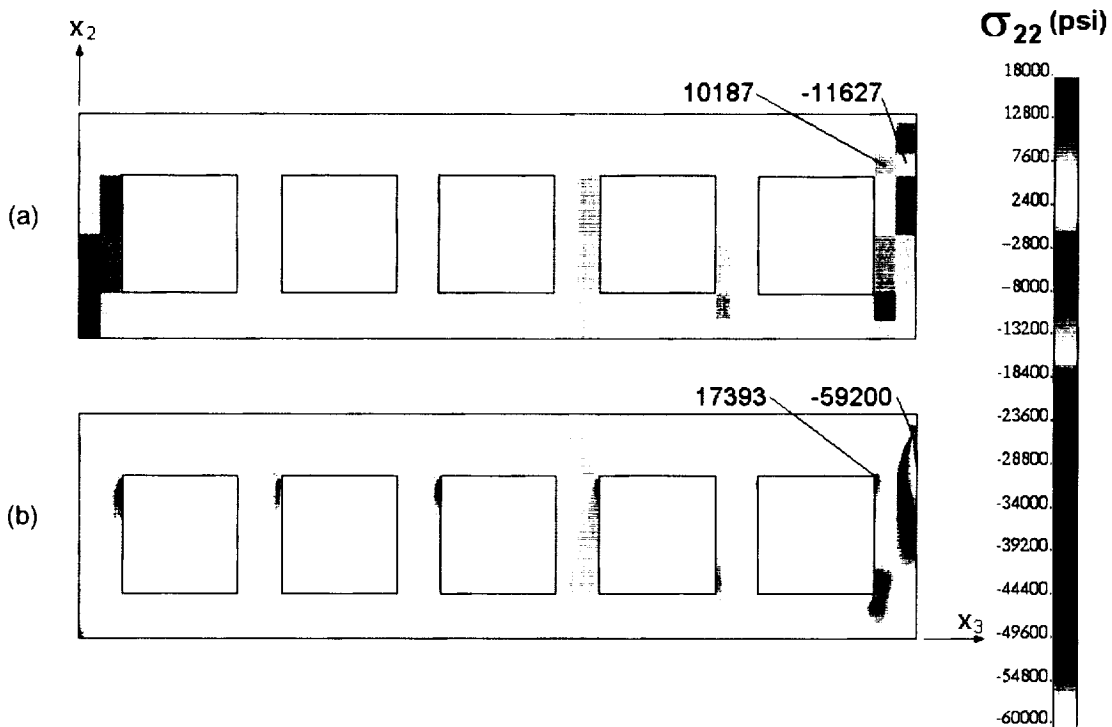


Figure 10: Peel stress, σ_{22} , for the: (a) least and (b) most refined grids.

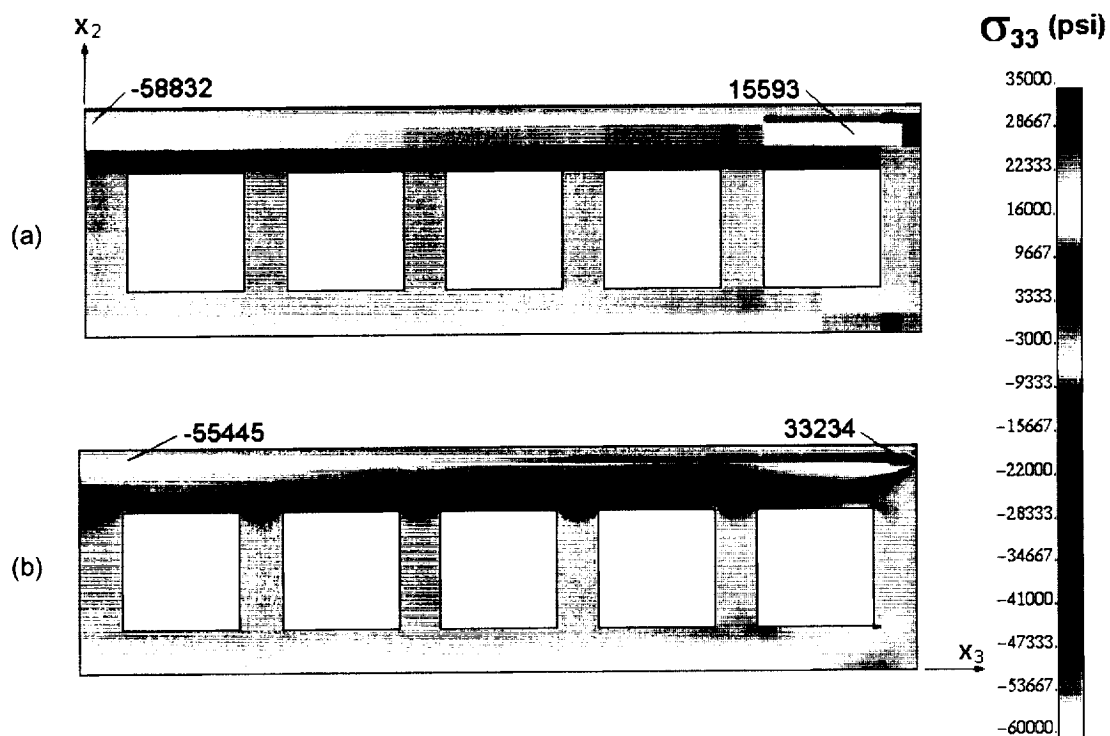


Figure 11: In-plane normal stress, σ_{33} , for the: (a) least and (b) most refined grids.

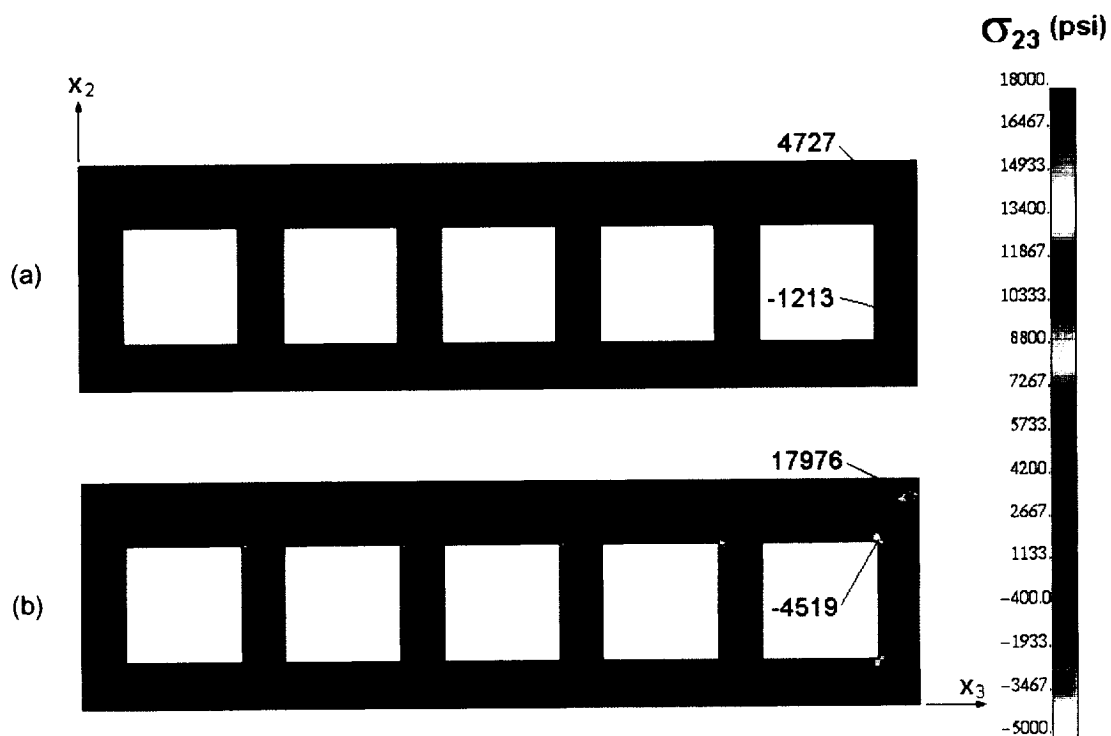


Figure 12: In-plane shear stress, σ_{23} , for the: (a) least and (b) most refined grids.

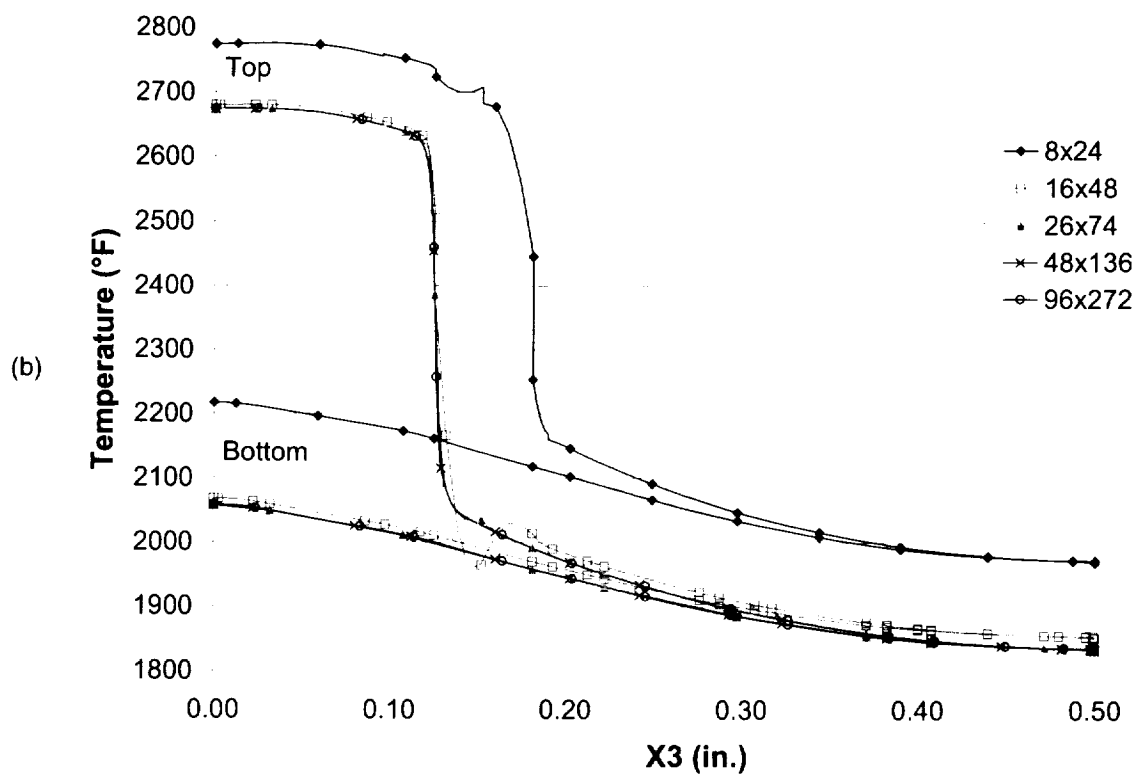
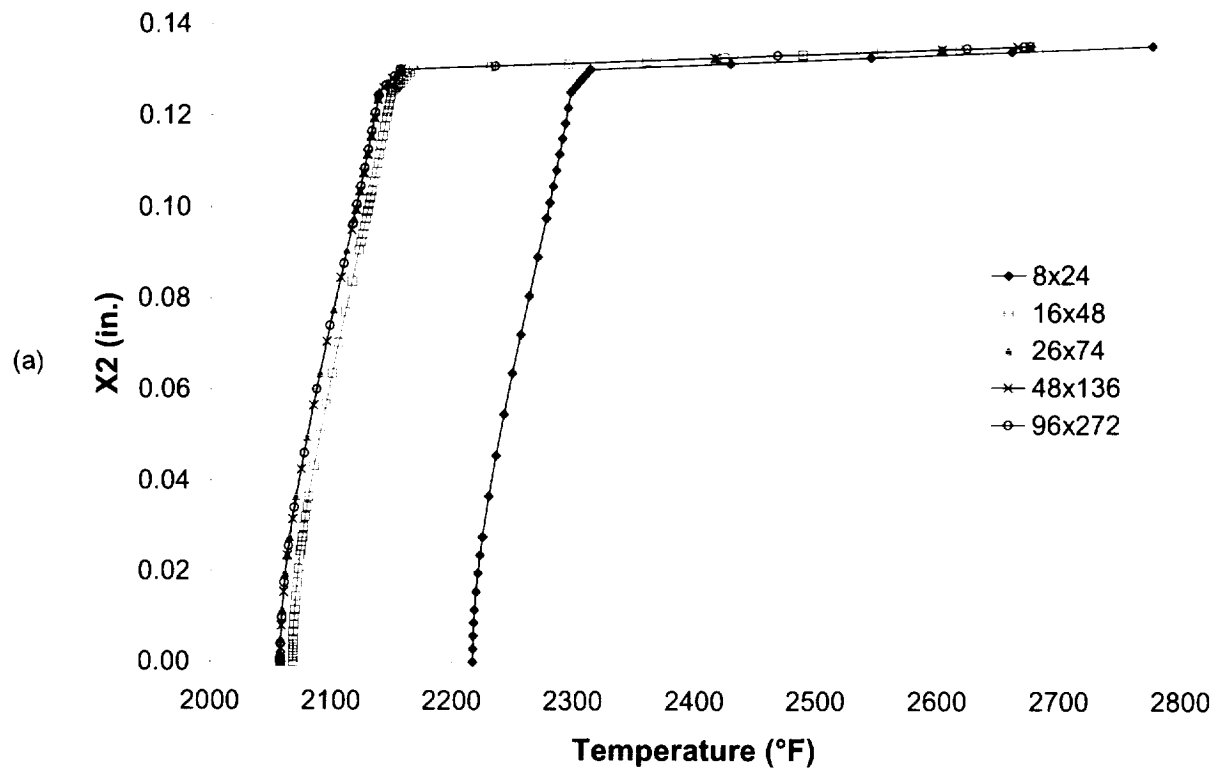


Figure 13: (a) Through-thickness temperature under flame, b) Temperature along top and bottom of plate. Effect of grid refinement is shown.

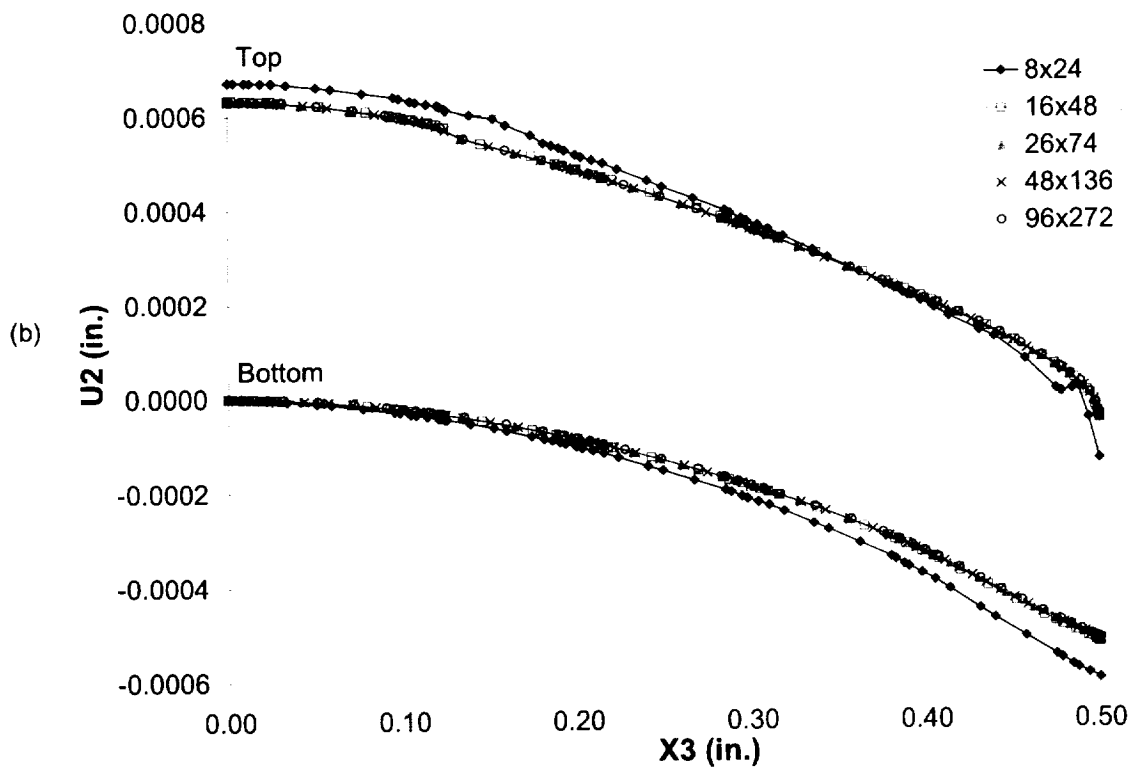
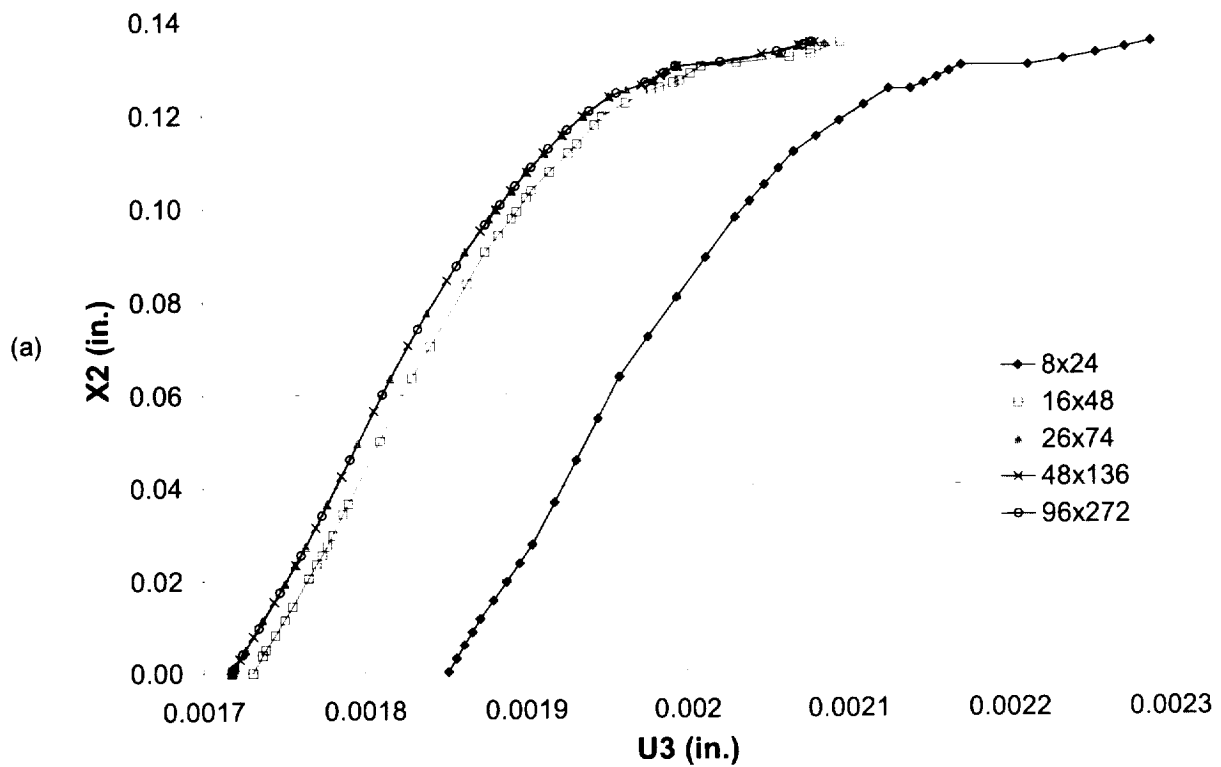


Figure 14: (a) Through-thickness x_3 -direction displacement at free edge, (b) x_2 -direction displacement along top and bottom of plate. Effect of grid refinement is shown.

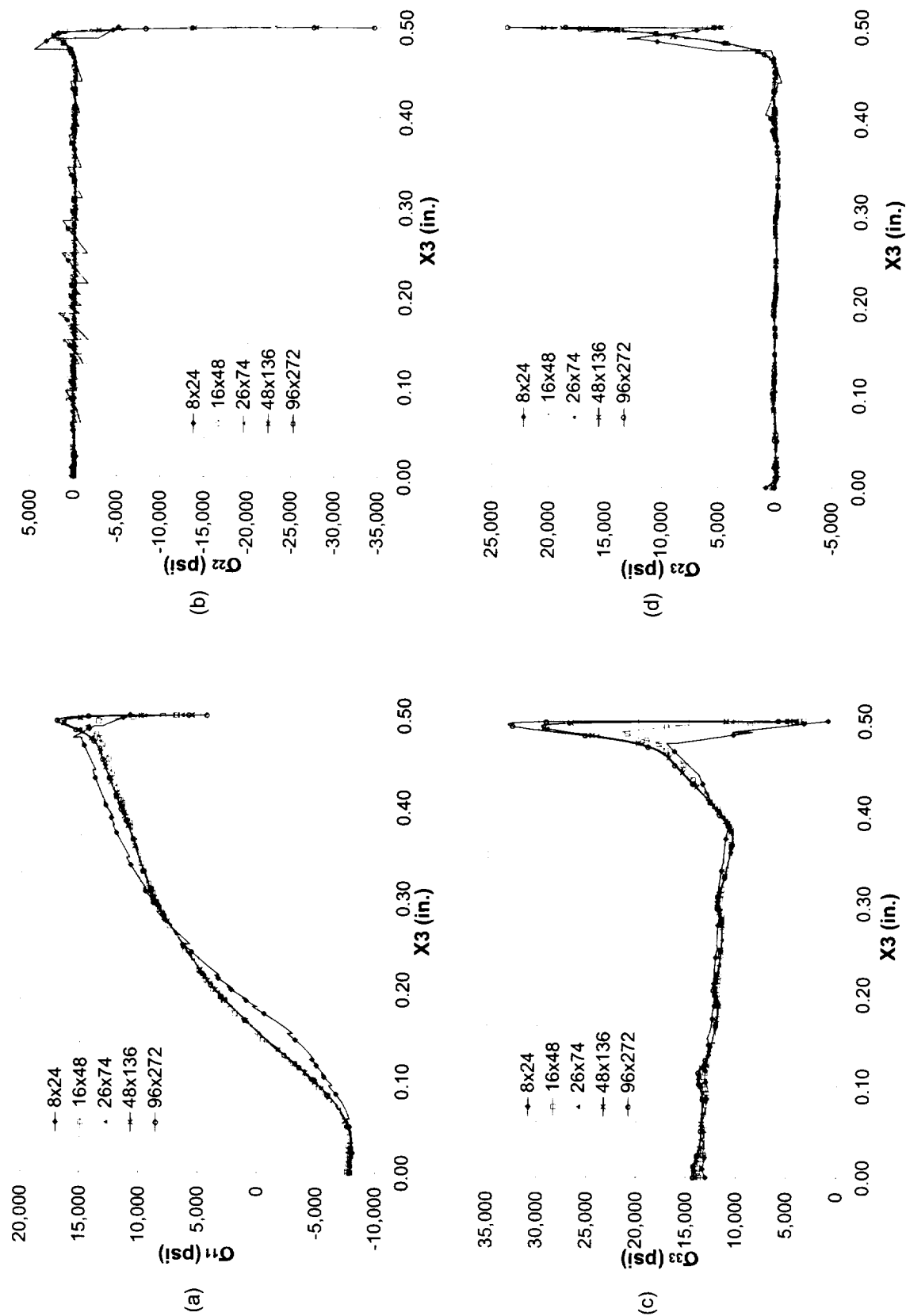


Figure 15: (a) σ_{11} in substrate along substrate/bondcoat interface, (b) σ_{22} in substrate along substrate/bondcoat interface, (c) σ_{33} in substrate along substrate/bondcoat interface, (d) σ_{33} in substrate along substrate/bondcoat interface. Effect of grid refinement is shown.

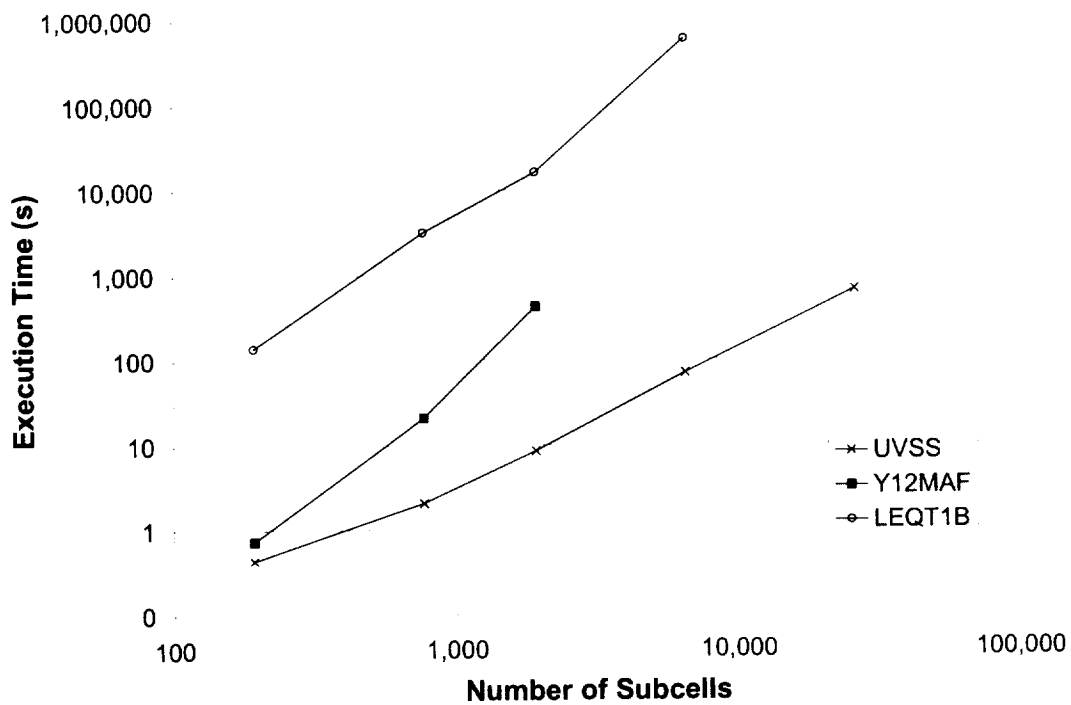


Figure 16: Model execution times as a function of the number of subcells in the analyzed geometry utilizing three different linear equation solvers.

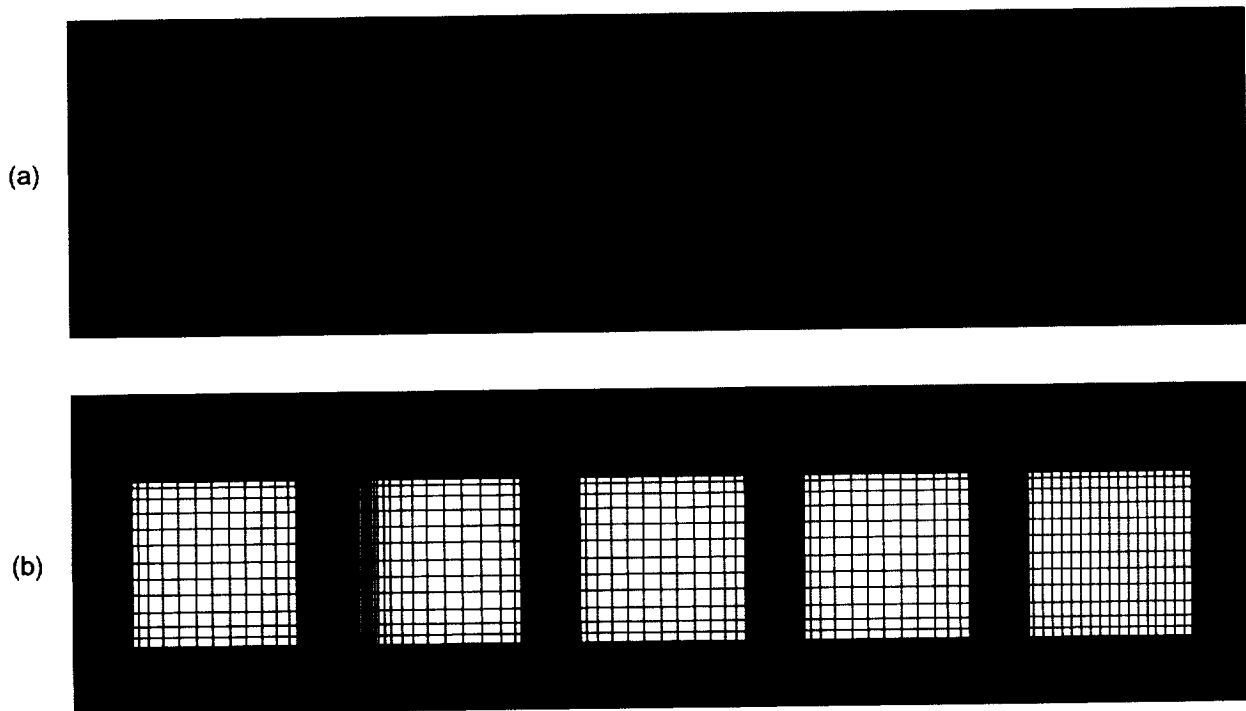


Figure 17: (a) Subcell grid for the plate with no cooling channels, (b) Subcell grid for the plate with the fixed temperature flame boundary conditions.

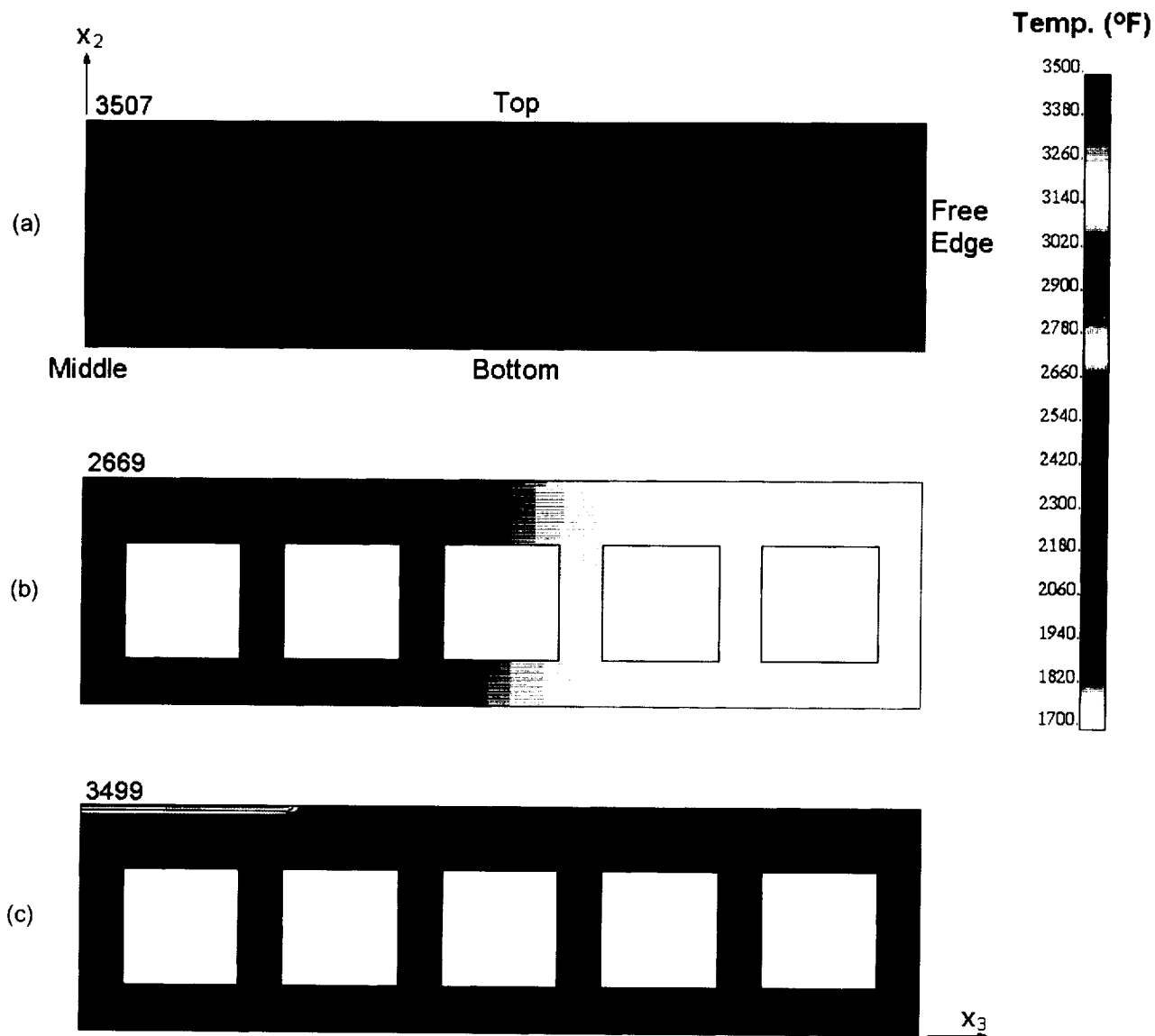


Figure 18: Temperature profiles. (a) No Internal cooling: convective flame boundary condition, (b) Internal cooling: convective flame boundary condition, (c) Internal cooling: fixed temperature flame boundary condition.

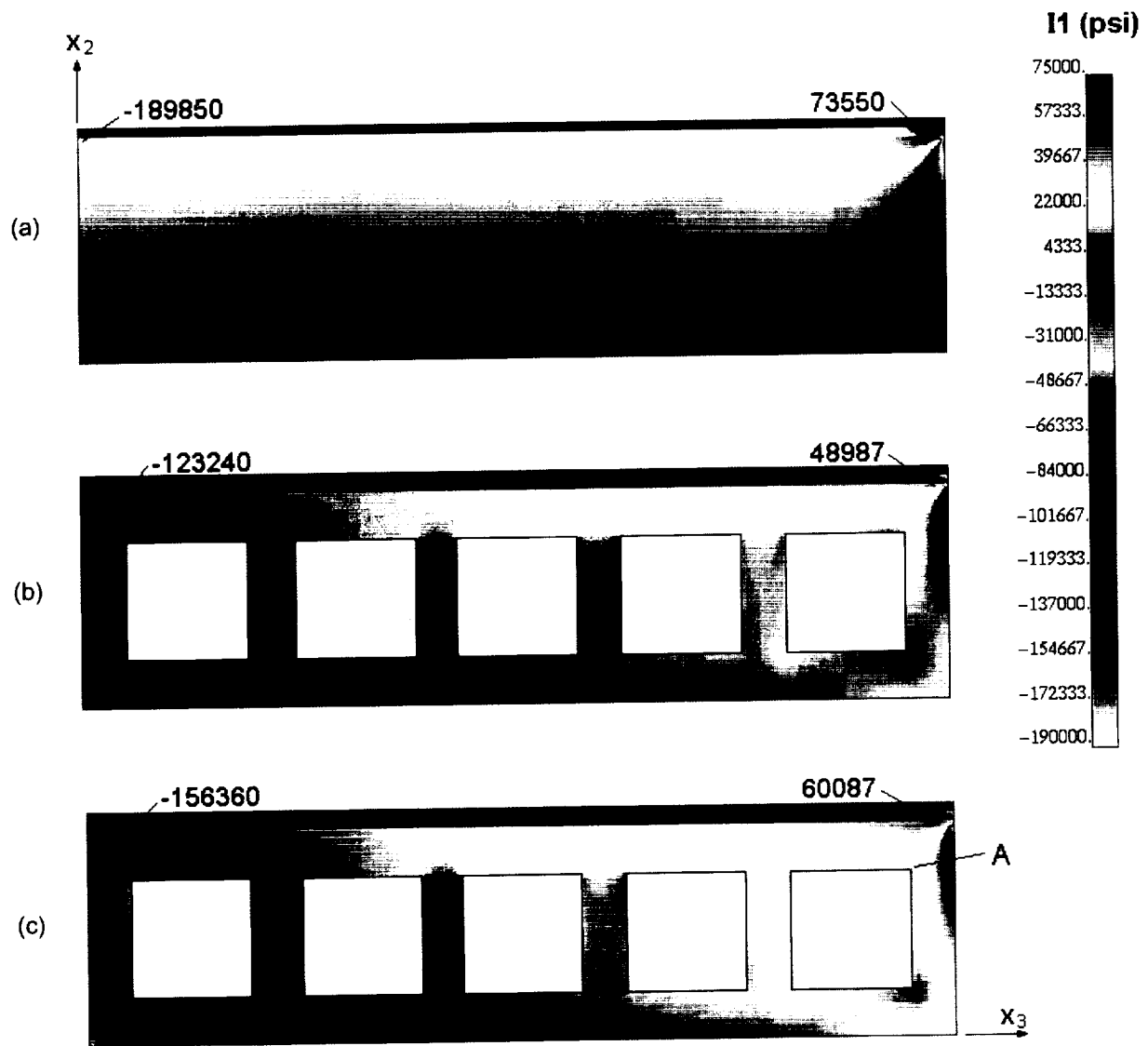


Figure 19: I_1 stress invariant profiles: (a) No Internal cooling: convective flame boundary condition, (b) Internal cooling: convective flame boundary condition, (c) Internal cooling: fixed temperature flame boundary condition.

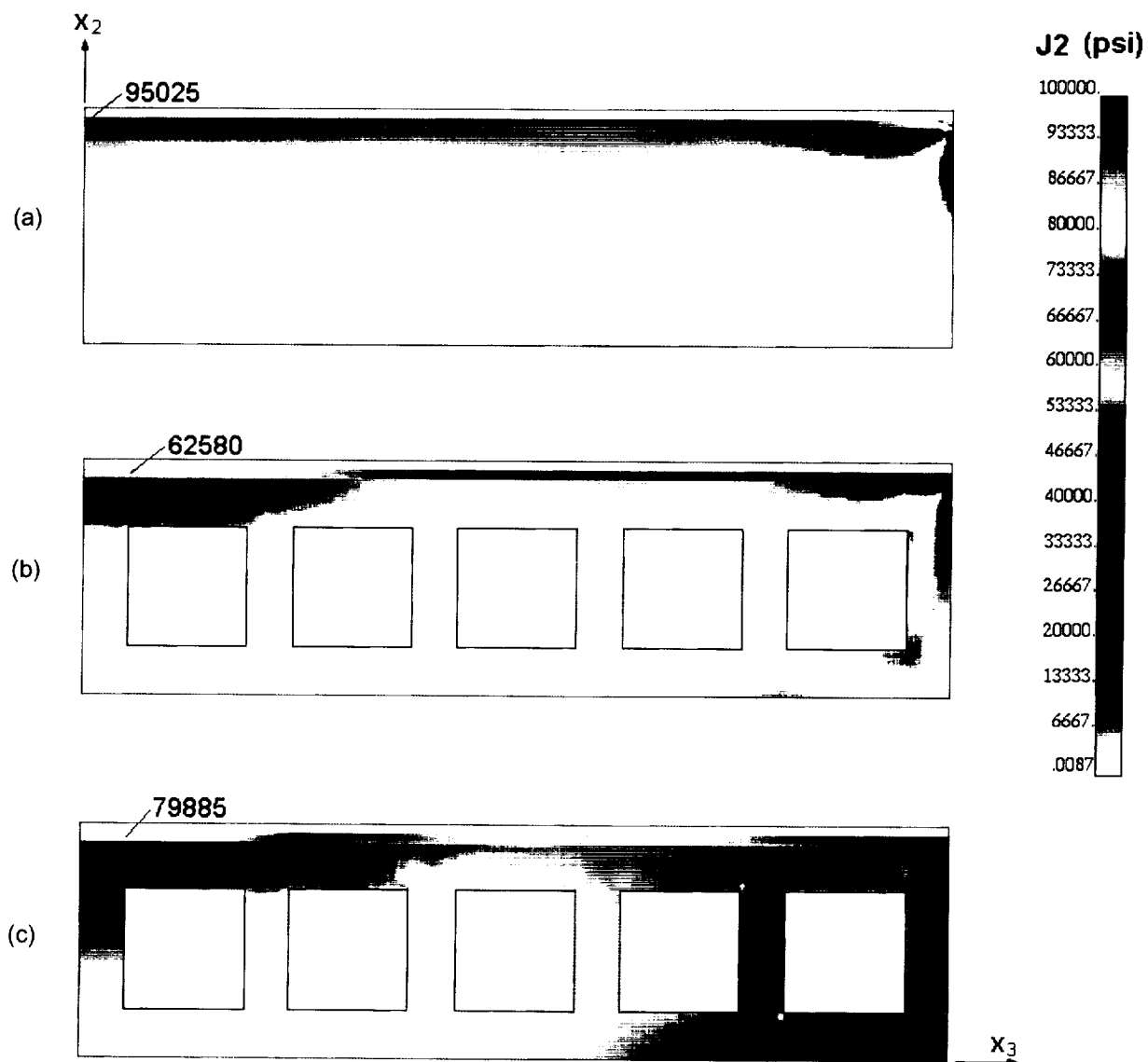


Figure 20: J_2 stress invariant profiles: (a) No Internal cooling: convective flame boundary condition, (b) Internal cooling: convective flame boundary condition, (c) Internal cooling: fixed temperature flame boundary condition.



Figure 21: Detailed temperature field for the plate with no cooling (reduced range of scale).

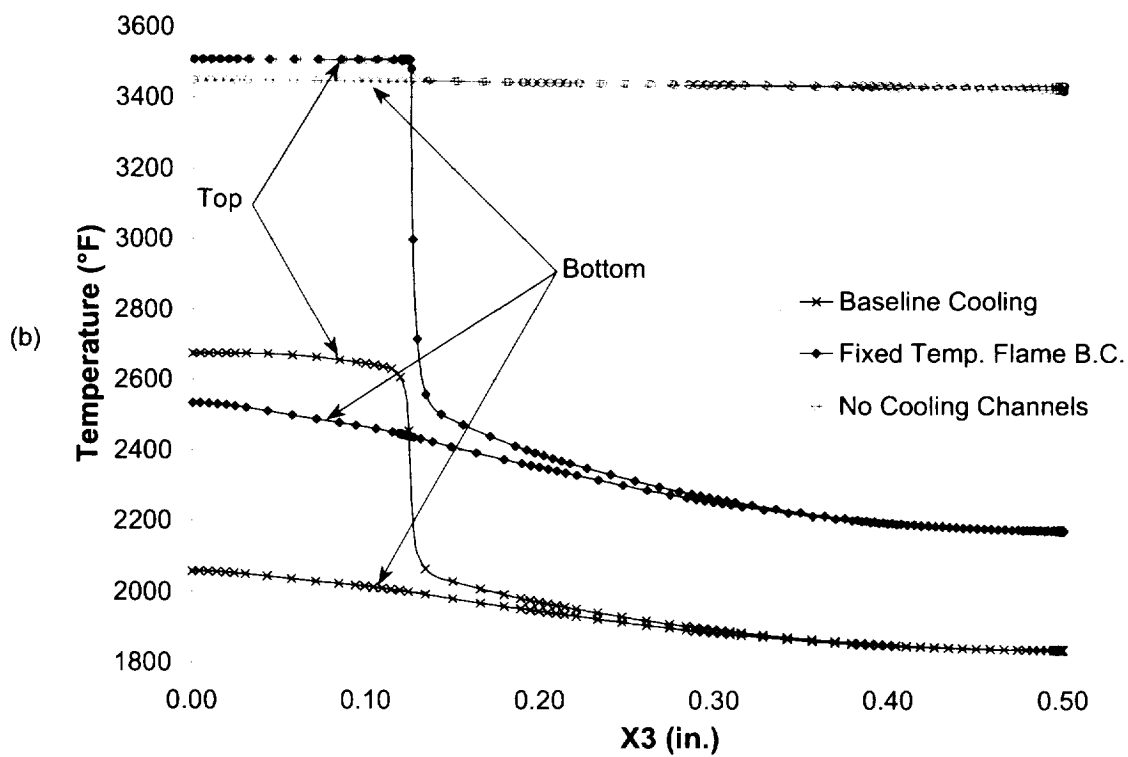
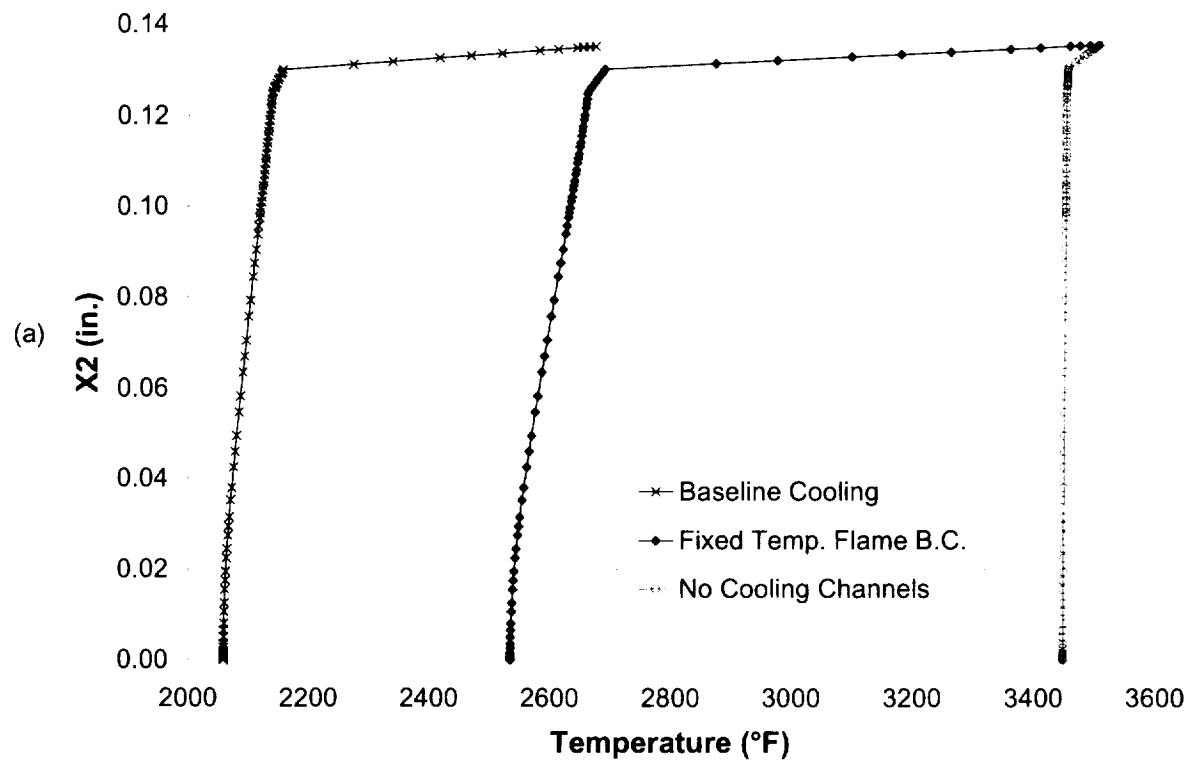


Figure 22: (a) Through-thickness temperature under flame, (b) Temperature along top and bottom of plate. Effects of cooling channel presence and flame boundary condition are illustrated.

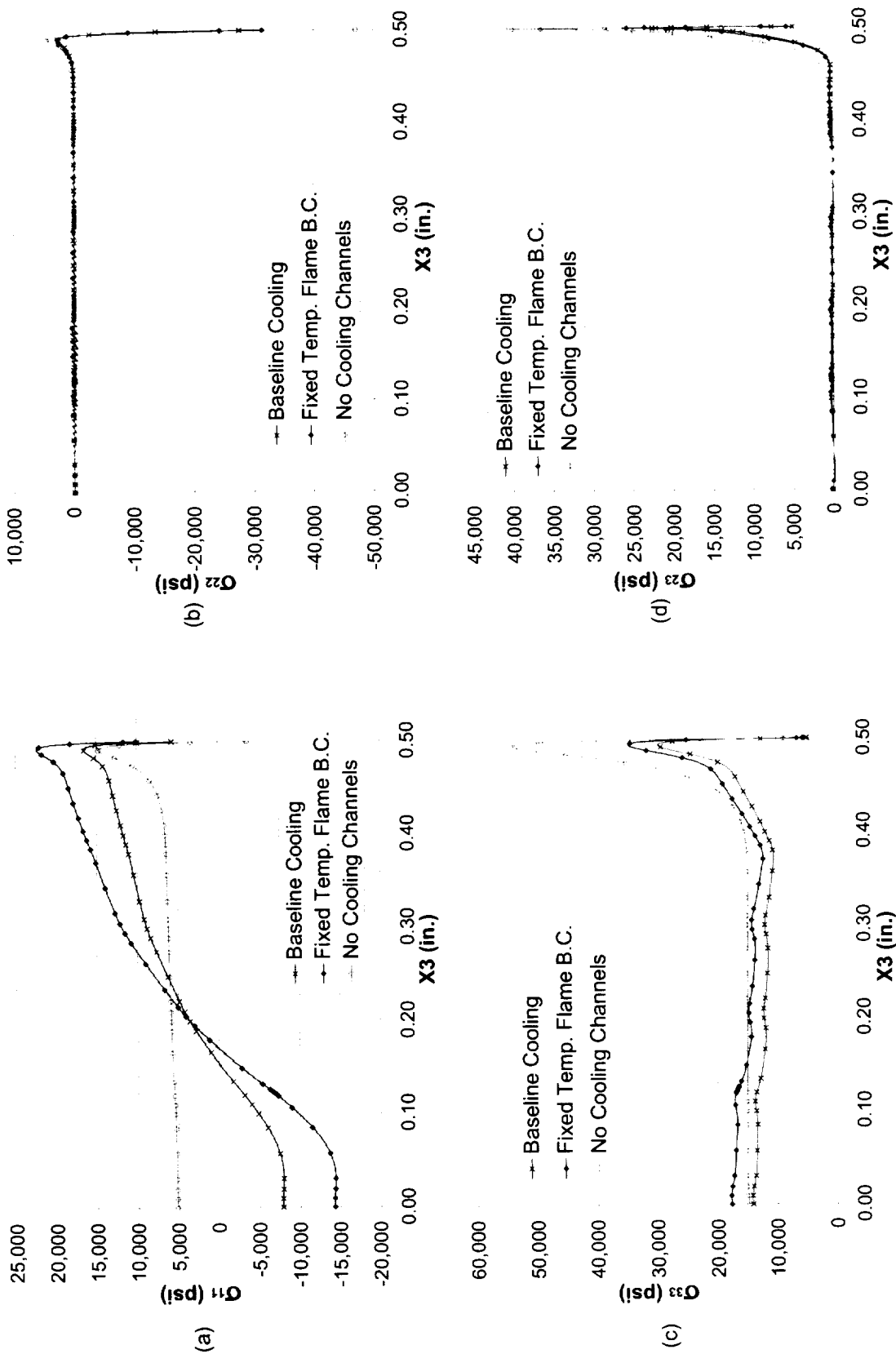


Figure 23: (a) σ_{11} in substrate along substrate/bondcoat interface, (b) σ_{22} in substrate along substrate/bondcoat interface, (c) σ_{33} in substrate along substrate/bondcoat interface, (d) σ_{23} in substrate along substrate/bondcoat interface. Effects of cooling channel presence and flame boundary condition are illustrated.

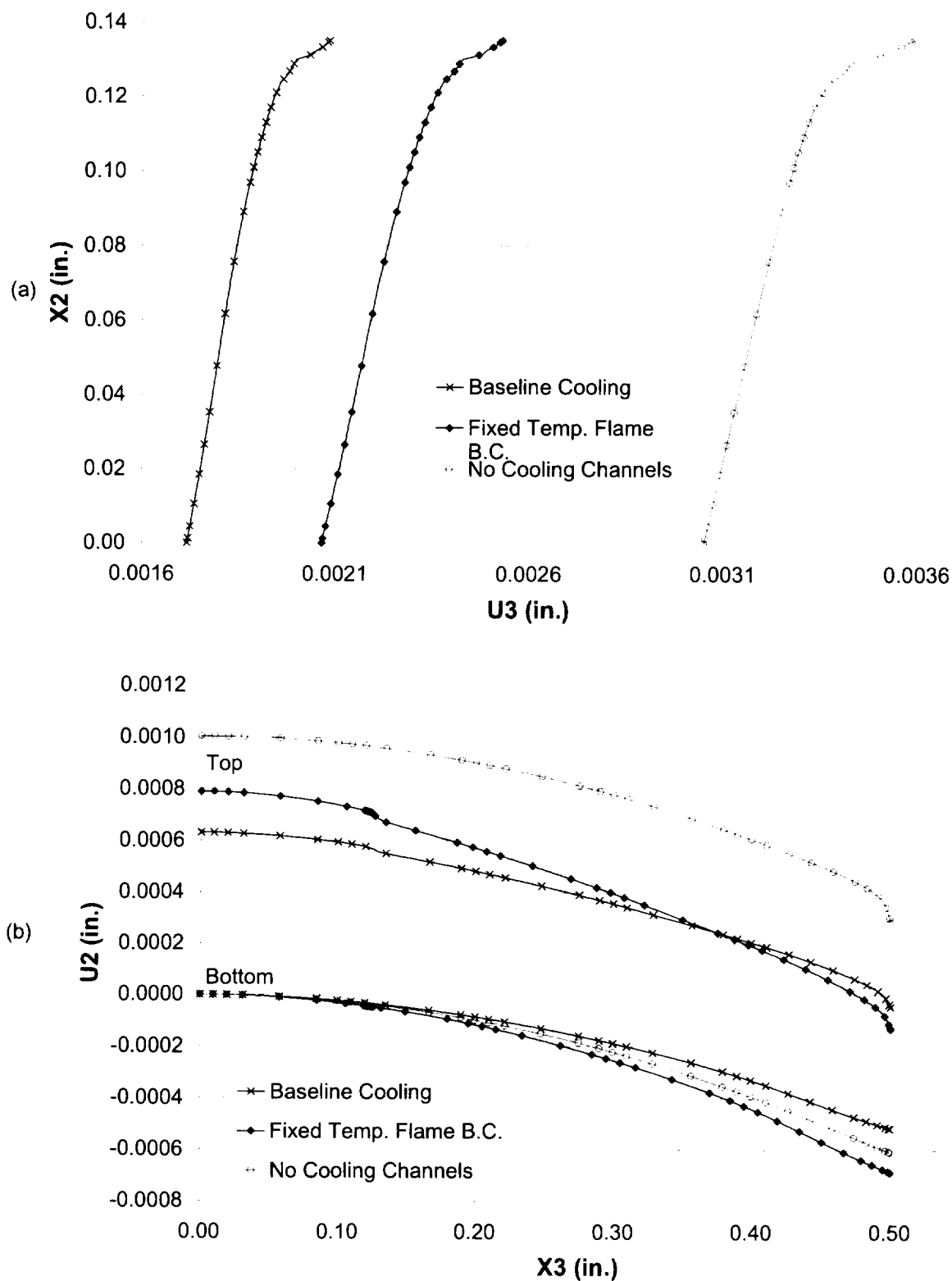


Figure 24: (a) Through-thickness x_3 -direction displacement at the free edge, (b) x_2 -direction displacement along the top and bottom of the plate. Effects of cooling channel presence and flame boundary condition are illustrated.

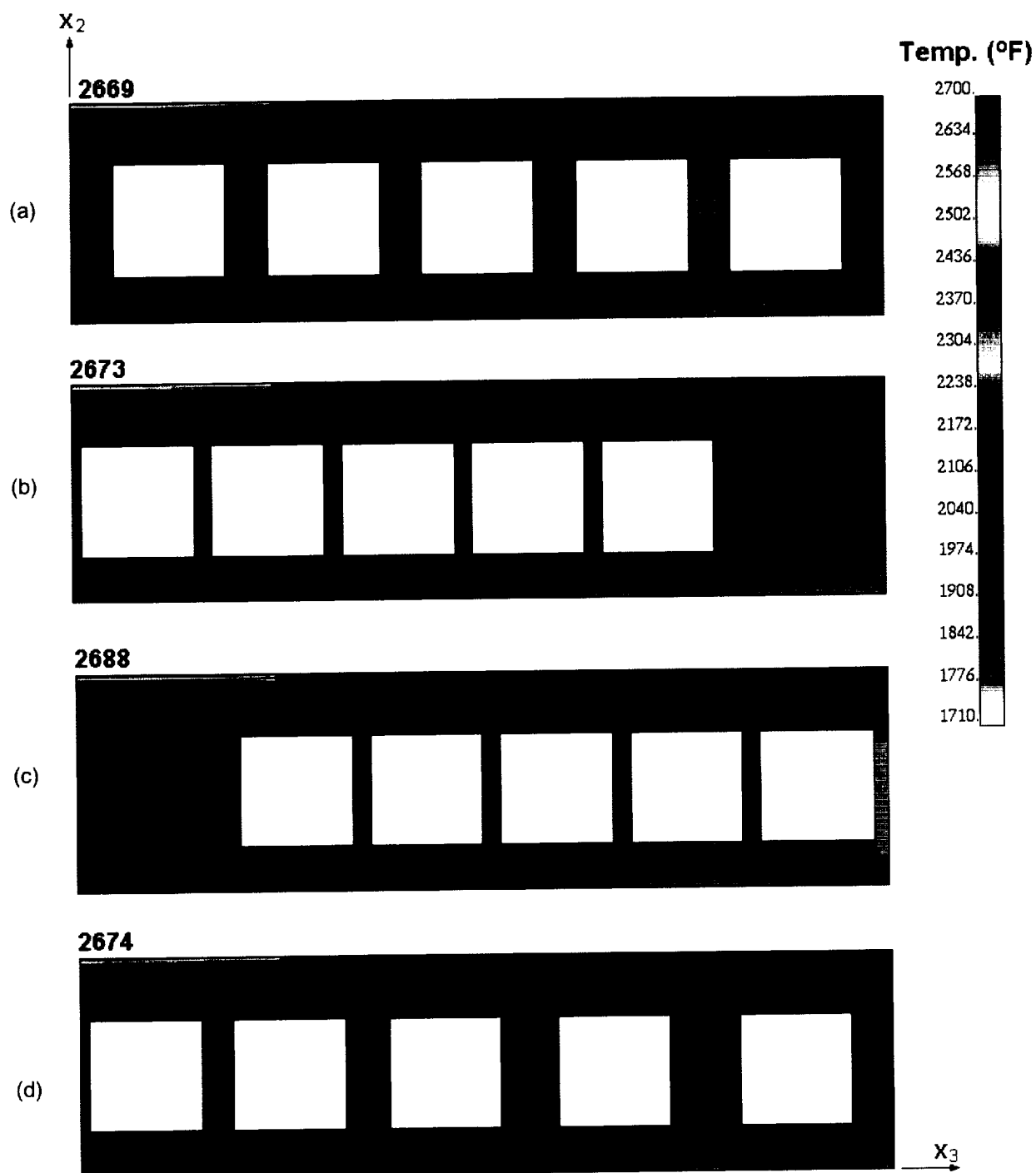


Figure 25: Temperature fields for plates with cooling channels: (a) in the baseline configuration, (b) shifted left, (c) shifted right, and (d) with linear spacing.

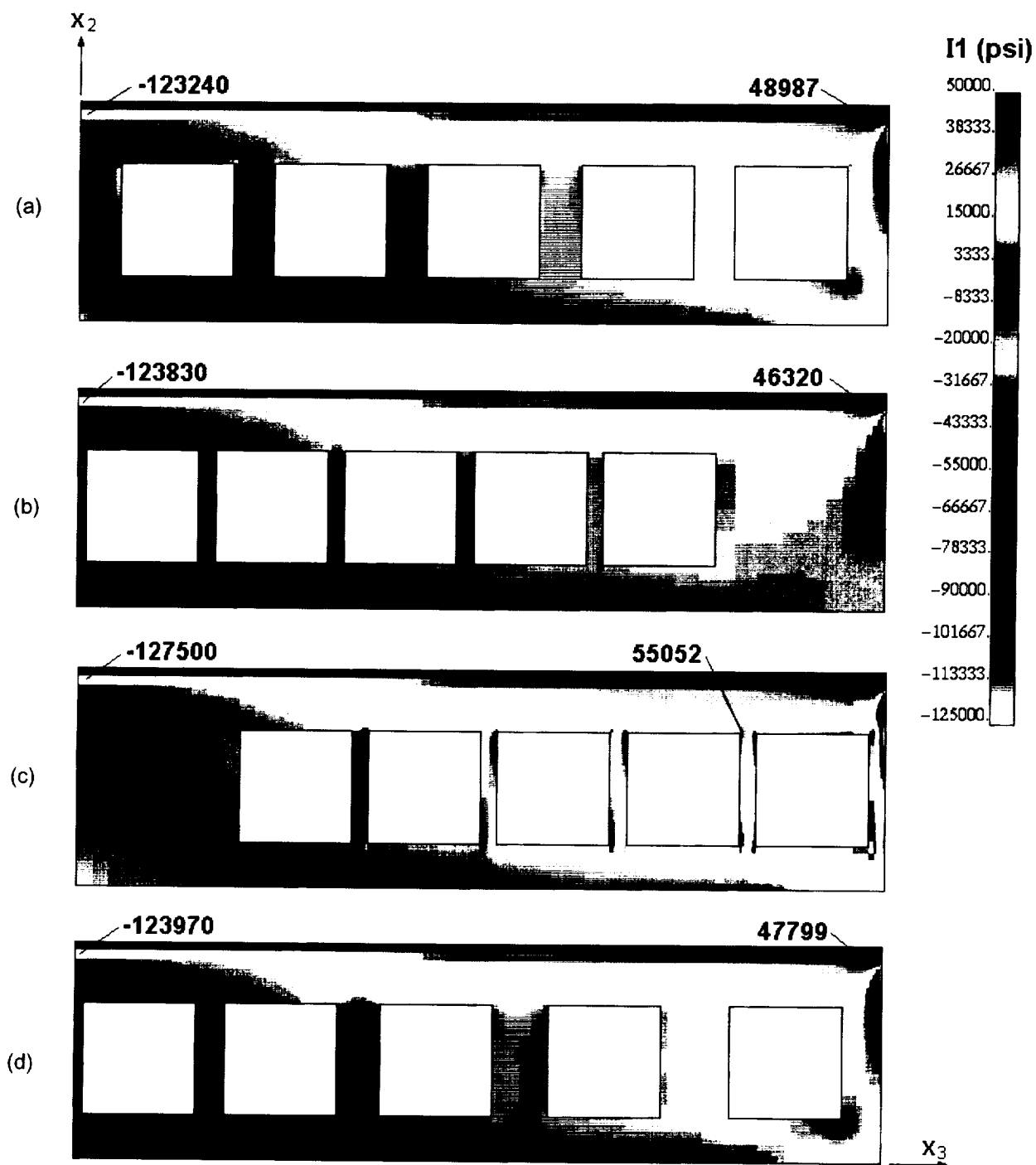


Figure 26: I_1 stress invariant fields for plates with cooling channels: (a) in the baseline configuration, (b) shifted left, (c) shifted right, and (d) with linear spacing.

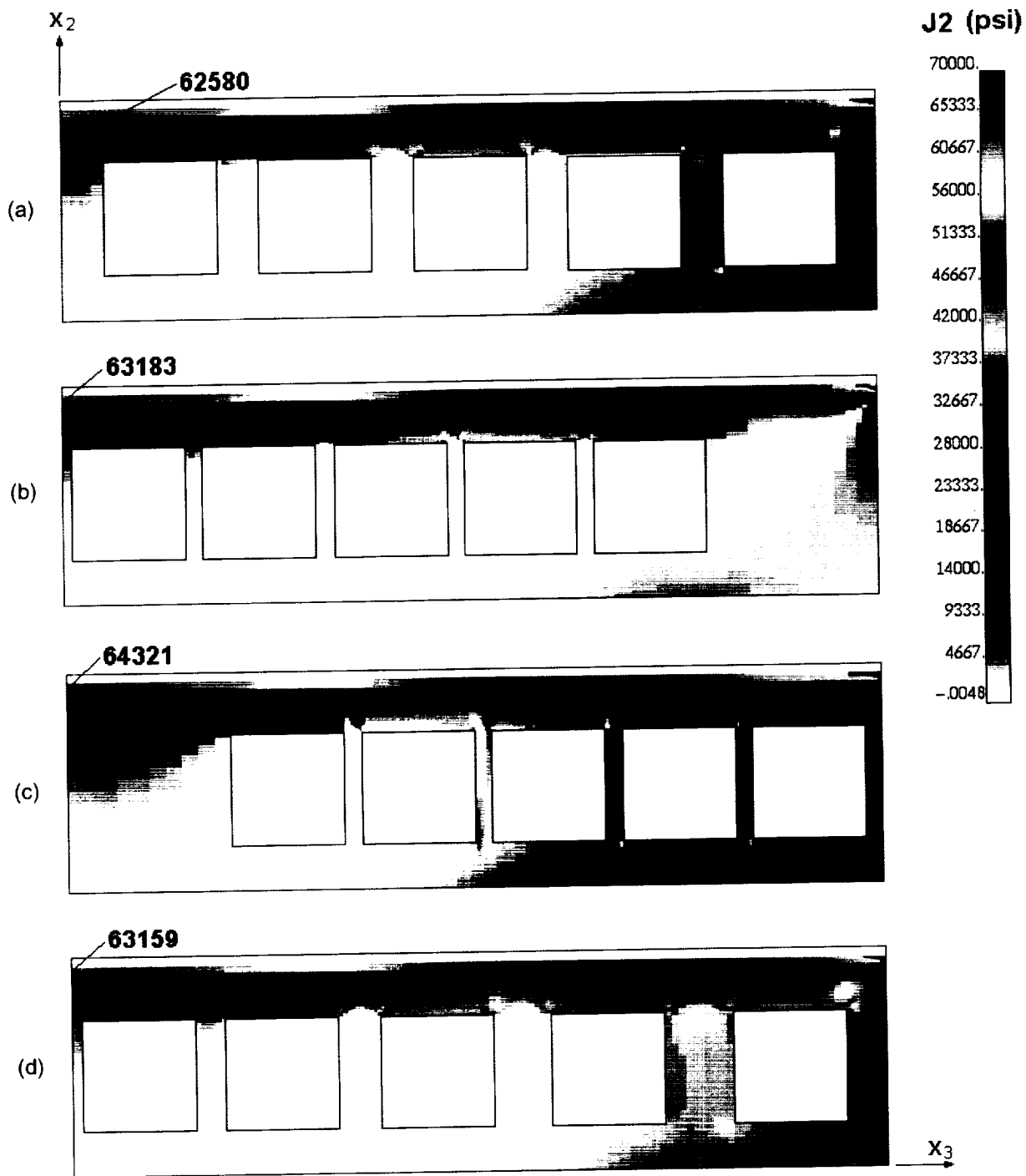


Figure 27: J_2 stress invariant fields for plates with cooling channels: (a) in the baseline configuration, (b) shifted left, (c) shifted right, and (d) with linear spacing.

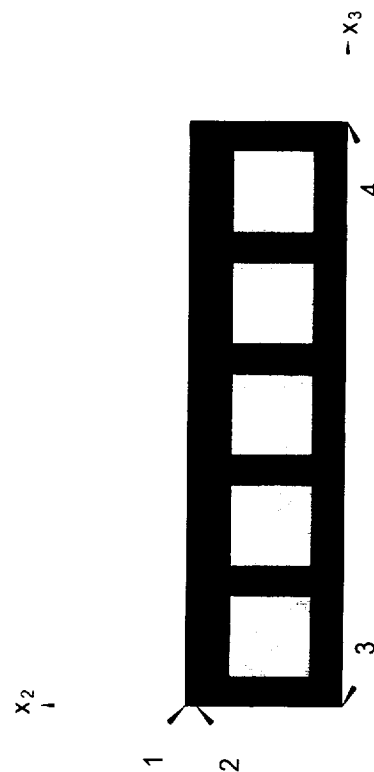
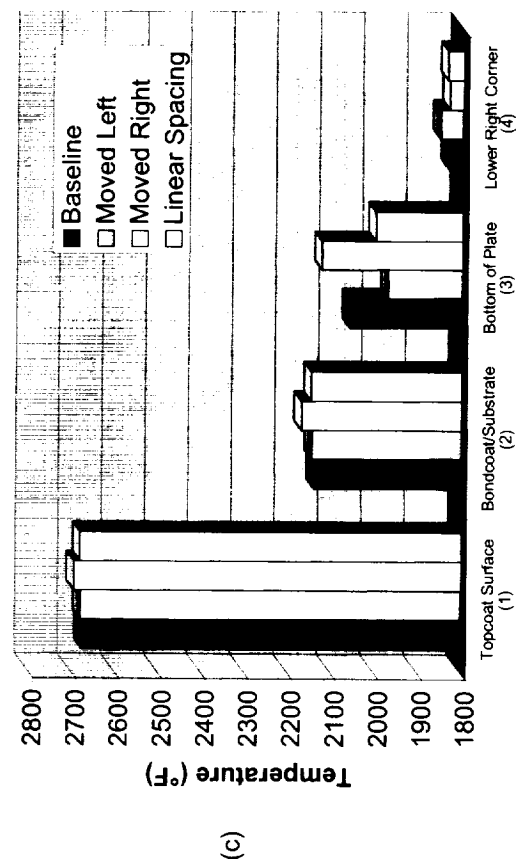
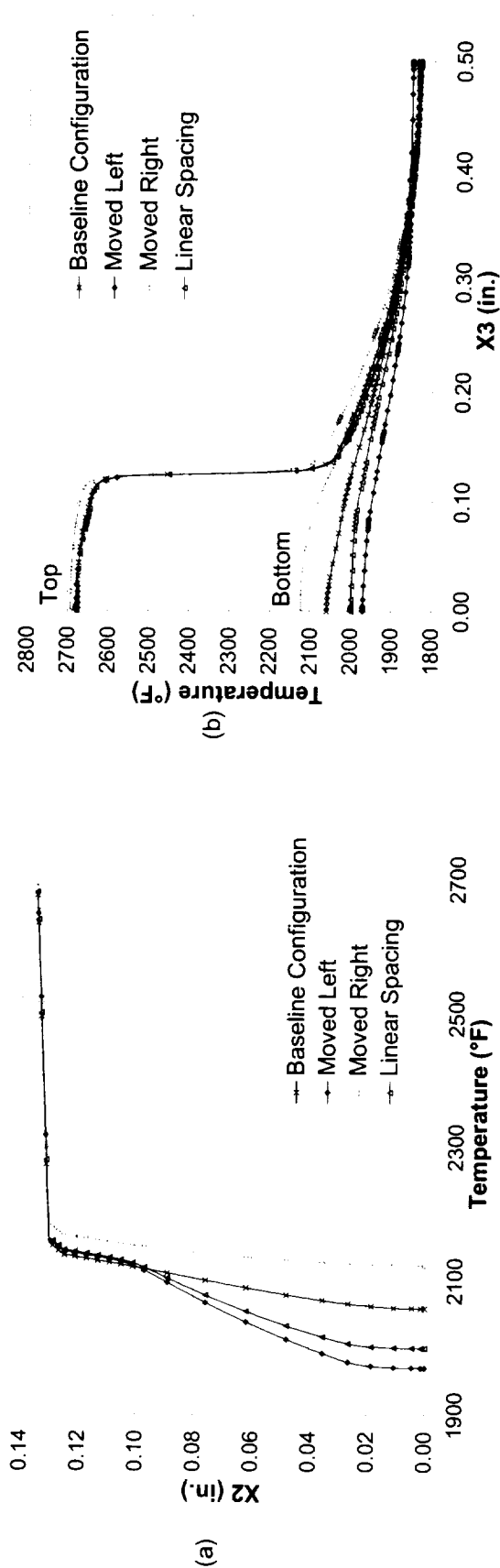


Figure 28: (a) Through-thickness temperature under flame, (b) Temperature along top and bottom of plate, (c) Comparison of temperatures at various locations in plate. Effect of shifting the channels horizontally is illustrated.

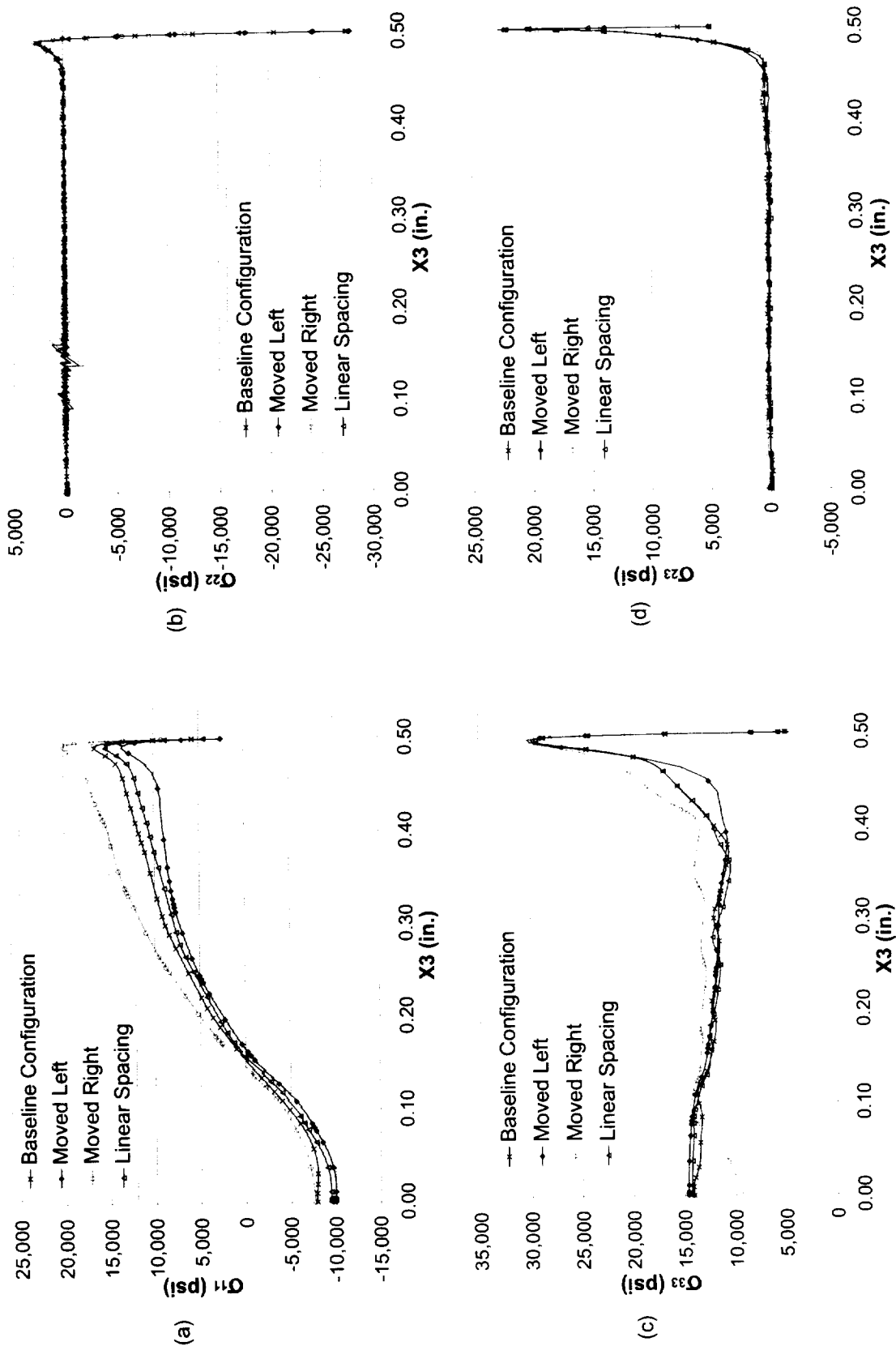


Figure 29: (a) σ_{11} in substrate along substrate/bondcoat interface, (b) σ_{22} in substrate along substrate/bondcoat interface, (c) σ_{33} in substrate along substrate/bondcoat interface, (d) σ_{23} in substrate along substrate/bondcoat interface. Effect of shifting the channels horizontally is illustrated.

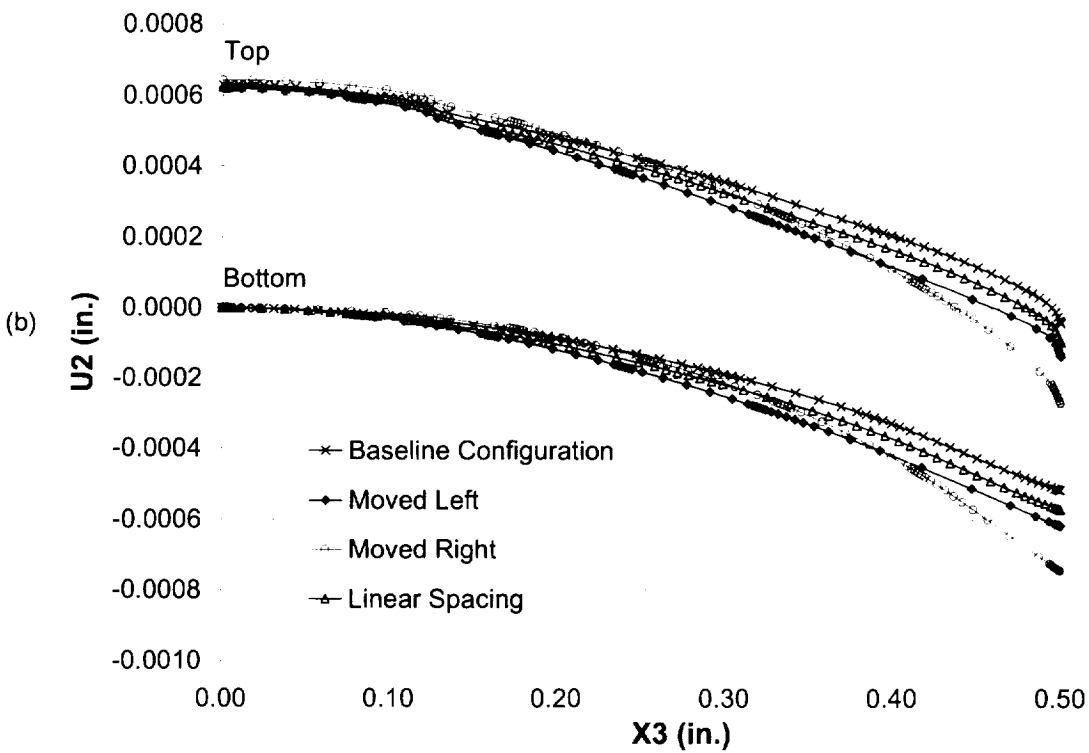
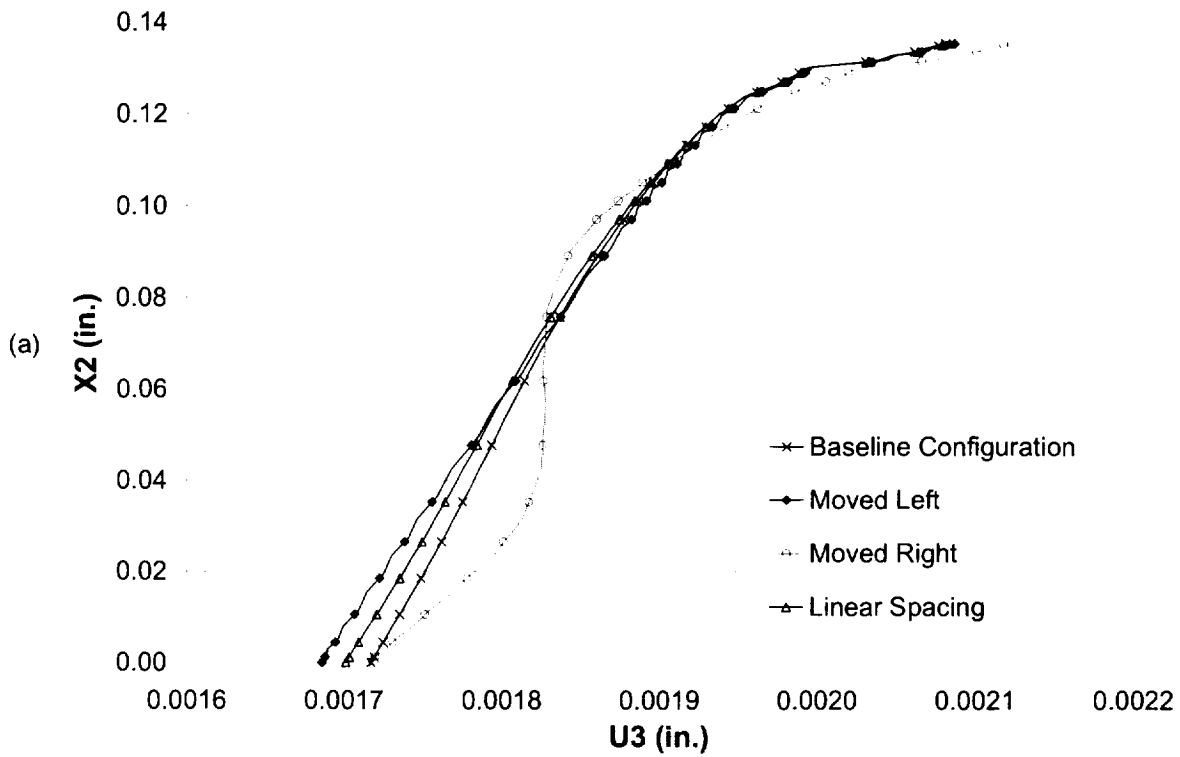


Figure 30: (a) Through-thickness x_3 -direction displacement at free edge of plate, (b) x_2 -direction displacement along top and bottom of plate. Effect of shifting the channels horizontally is illustrated.

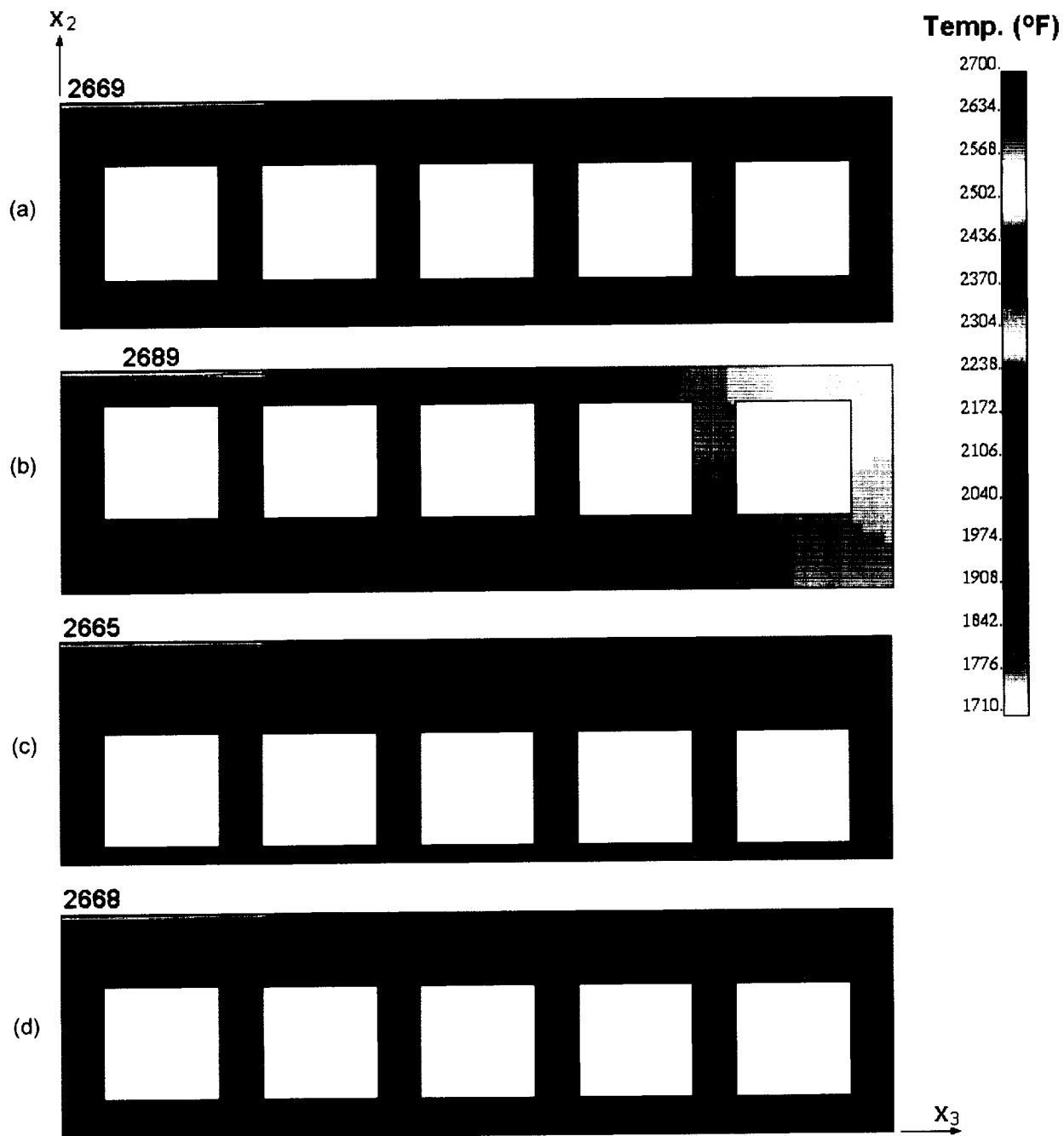


Figure 31: Plate temperature fields for: (a) baseline configuration, (b) cooling channels shifted up, (c) cooling channels shifted down, and (d) minimum bending vertical cooling channel location.

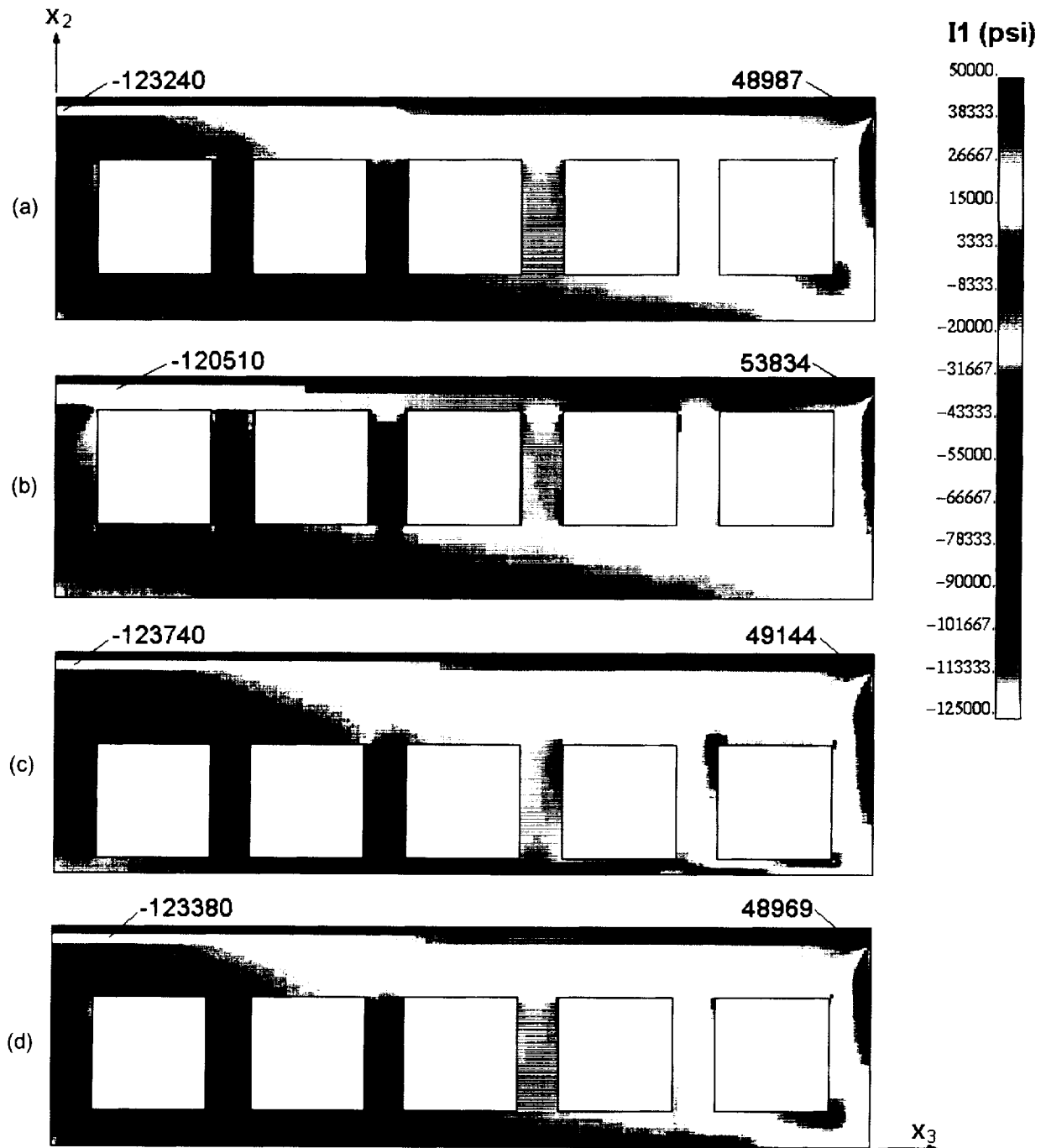


Figure 32: Plate I_1 stress invariant fields for: (a) baseline configuration, (b) cooling channels shifted up, (c) cooling channels shifted down, and (d) minimum bending vertical cooling channel location.

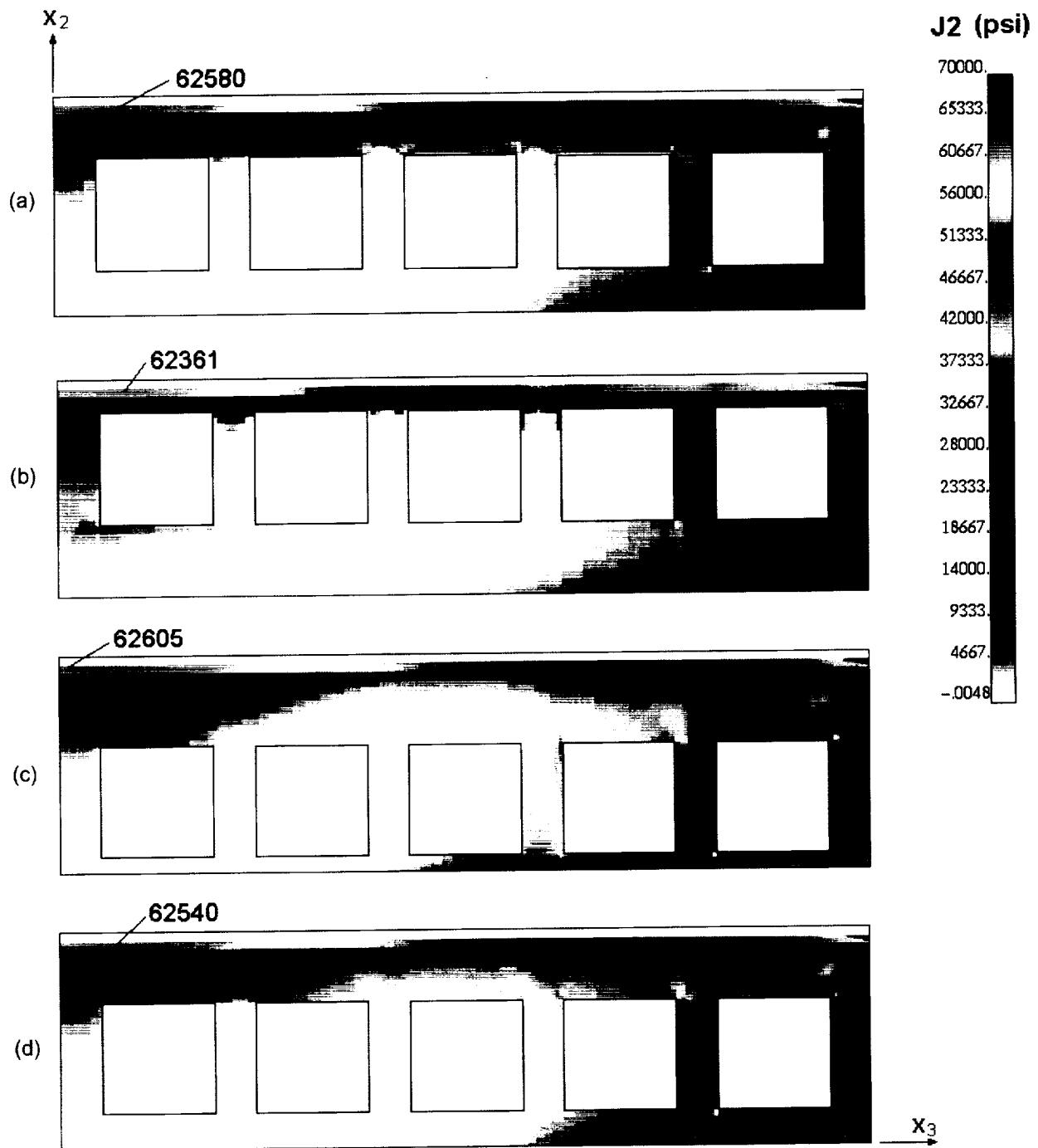


Figure 33: Plate J_2 stress invariant fields for: (a) baseline configuration, (b) cooling channels shifted up, (c) cooling channels shifted down, and (d) minimum bending vertical cooling channel location.

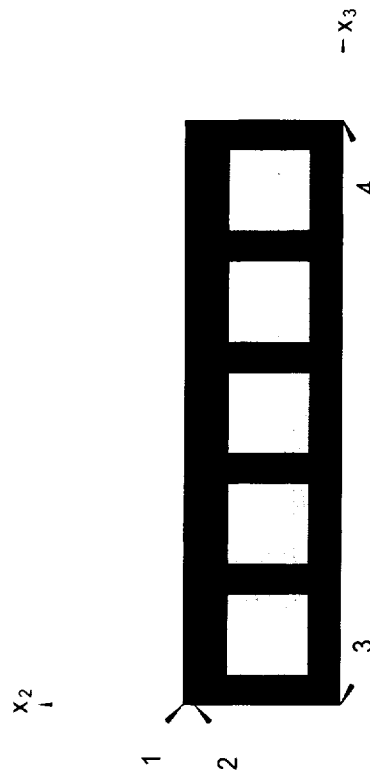
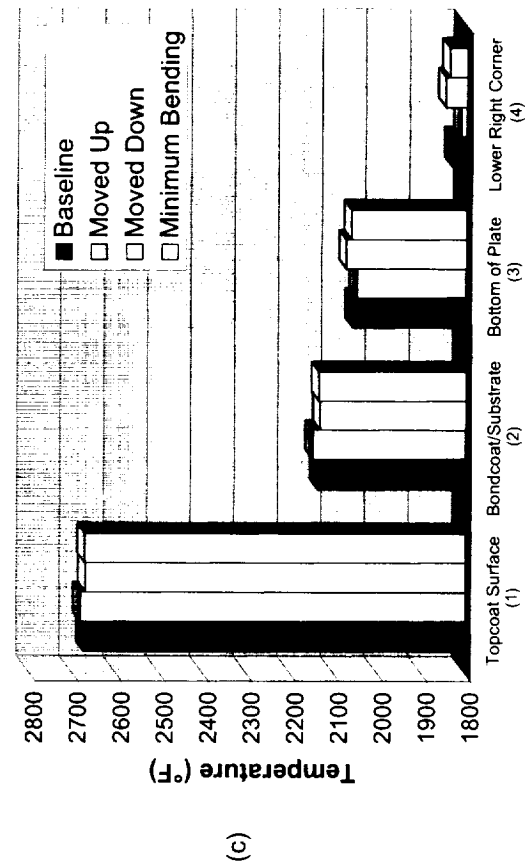
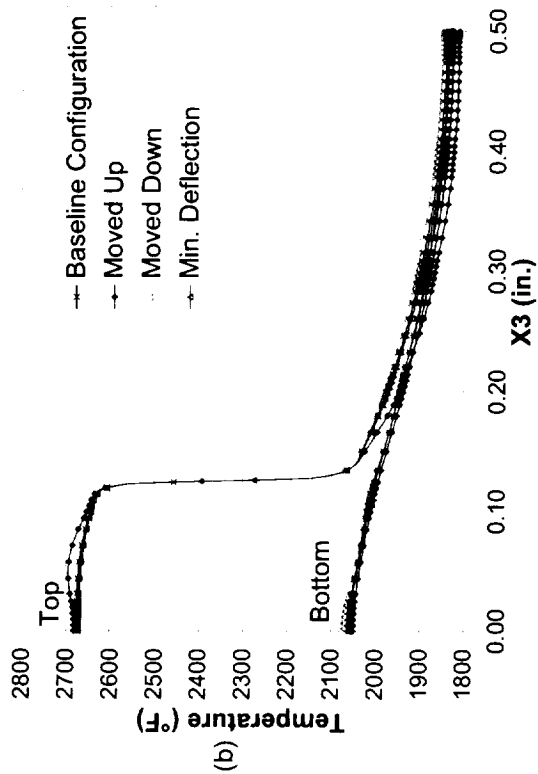
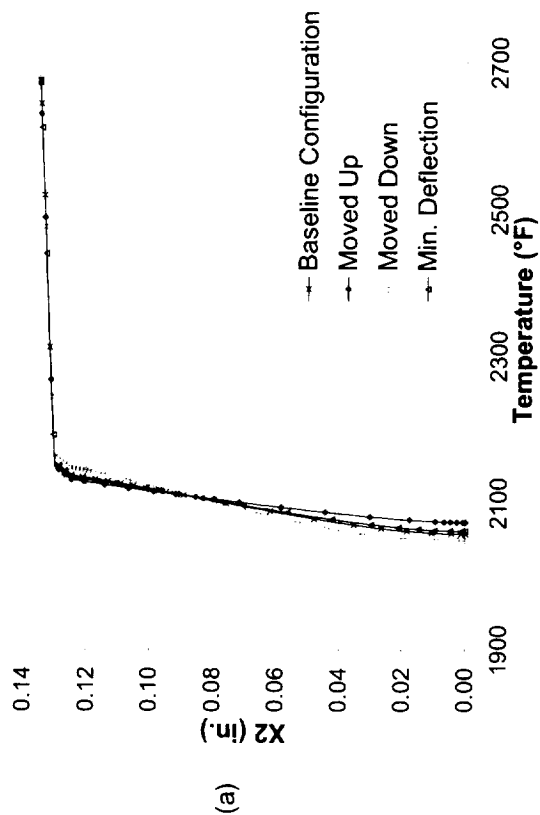


Figure 34: (a) Through-thickness temperature under flame, (b) Temperature along top and bottom of plate, (c) Comparison of temperature at locations within plate. Effect of shifting the channels vertically is illustrated.

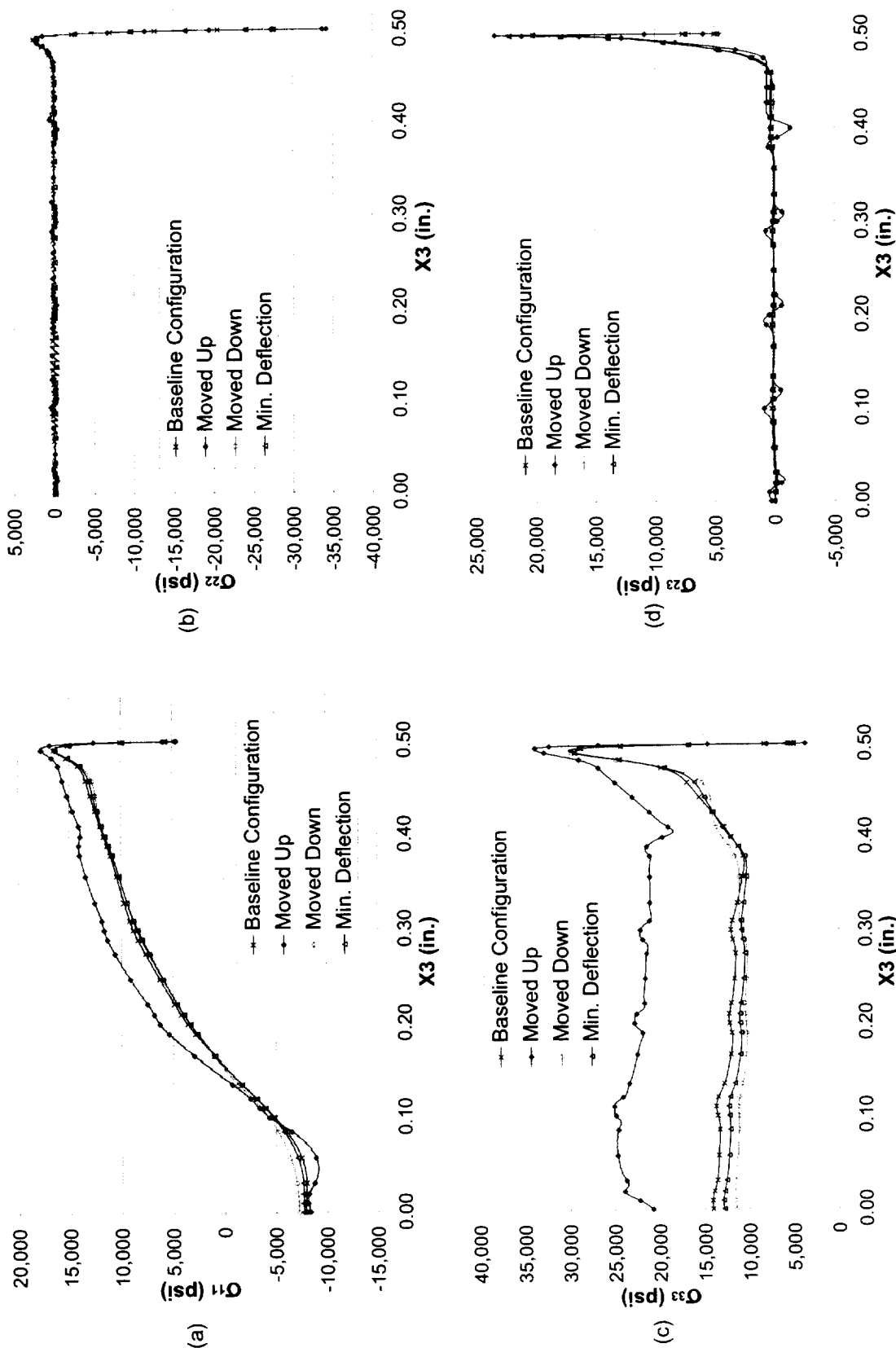


Figure 35: (a) σ_{11} in substrate along substrate/bondcoat interface, (b) σ_{22} in substrate along substrate/bondcoat interface, (c) σ_{33} in substrate along substrate/bondcoat interface, (d) σ_{23} in substrate along substrate/bondcoat interface. Effect of shifting the channels vertically is illustrated.

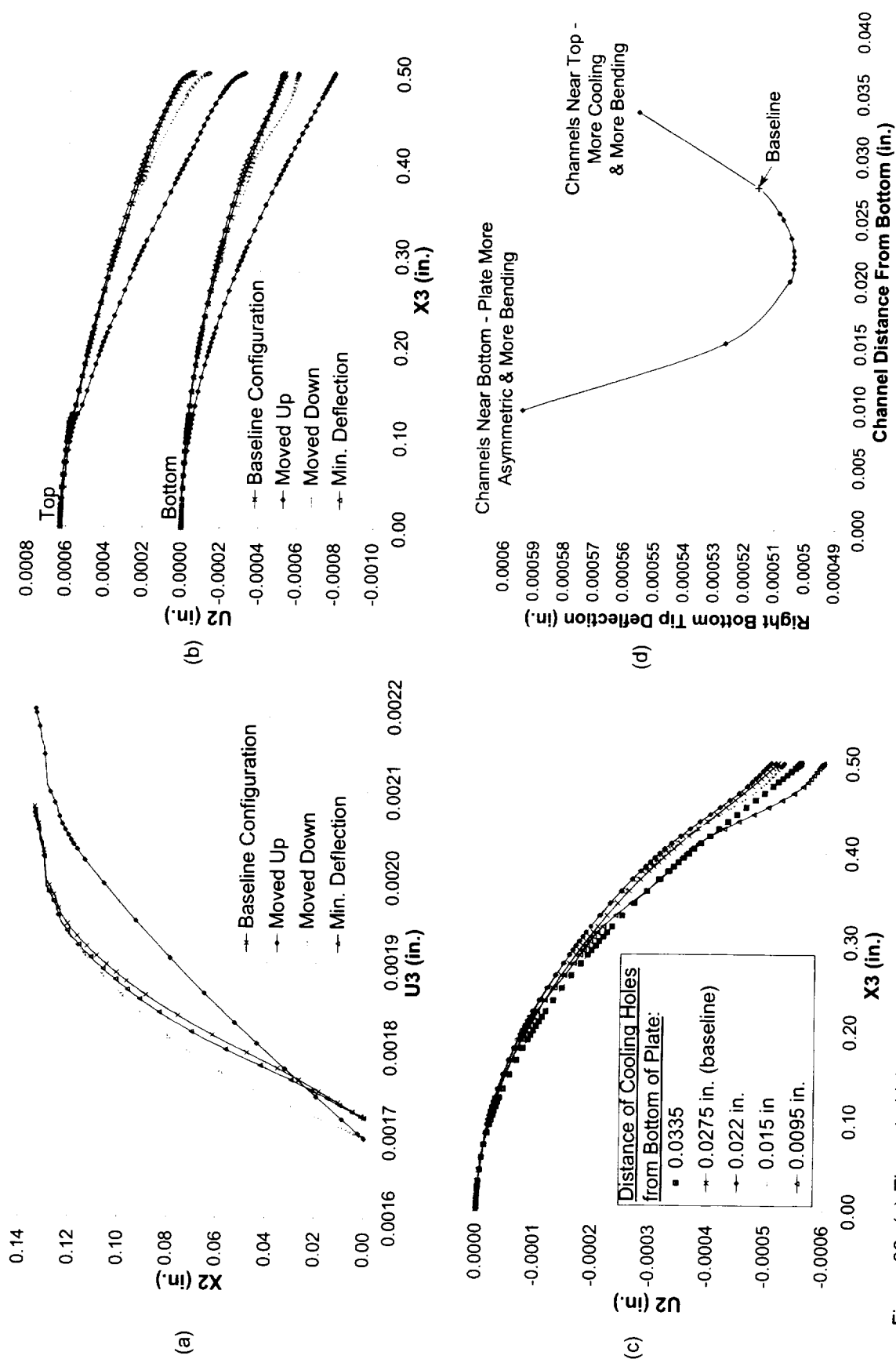


Figure 36: (a) Through-thickness x_3 -direction displacement at free edge of plate, (b) x_2 -direction displacement along top and bottom of plate, (c) x_2 -direction displacement along bottom of plate, (d) x_2 -direction displacement of plate's right bottom corner. Effect of shifting the channels vertically is illustrated.

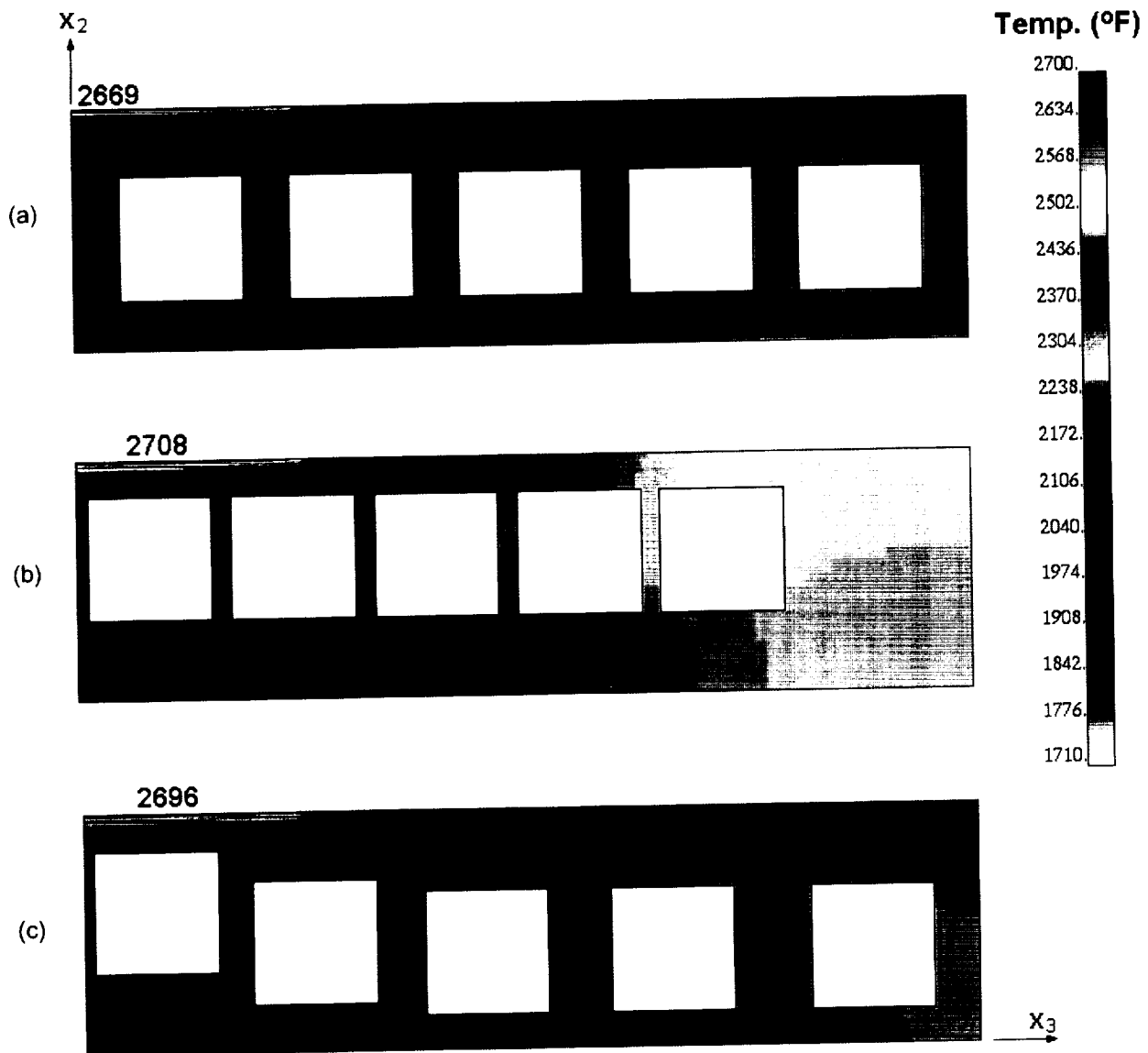


Figure 37: Plate temperature fields for: (a) baseline configuration, (b) cooling channels shifted up and to the left, and (c) cooling channels arranged both horizontally and vertically.

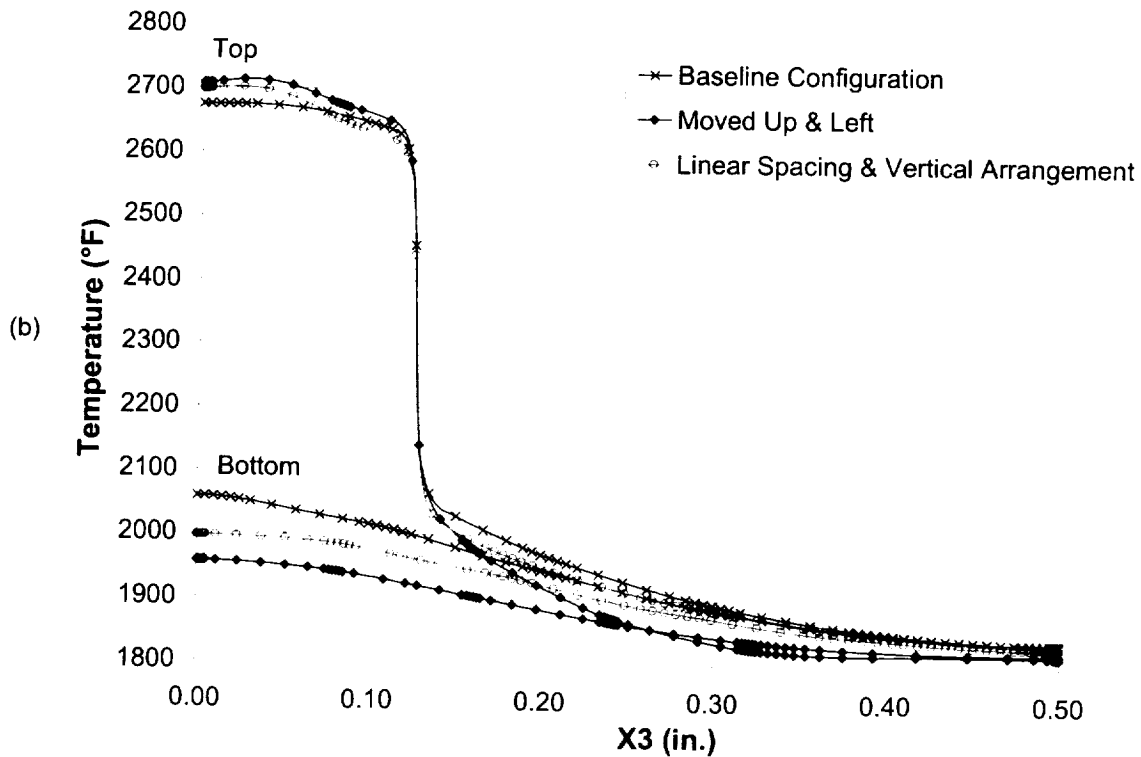
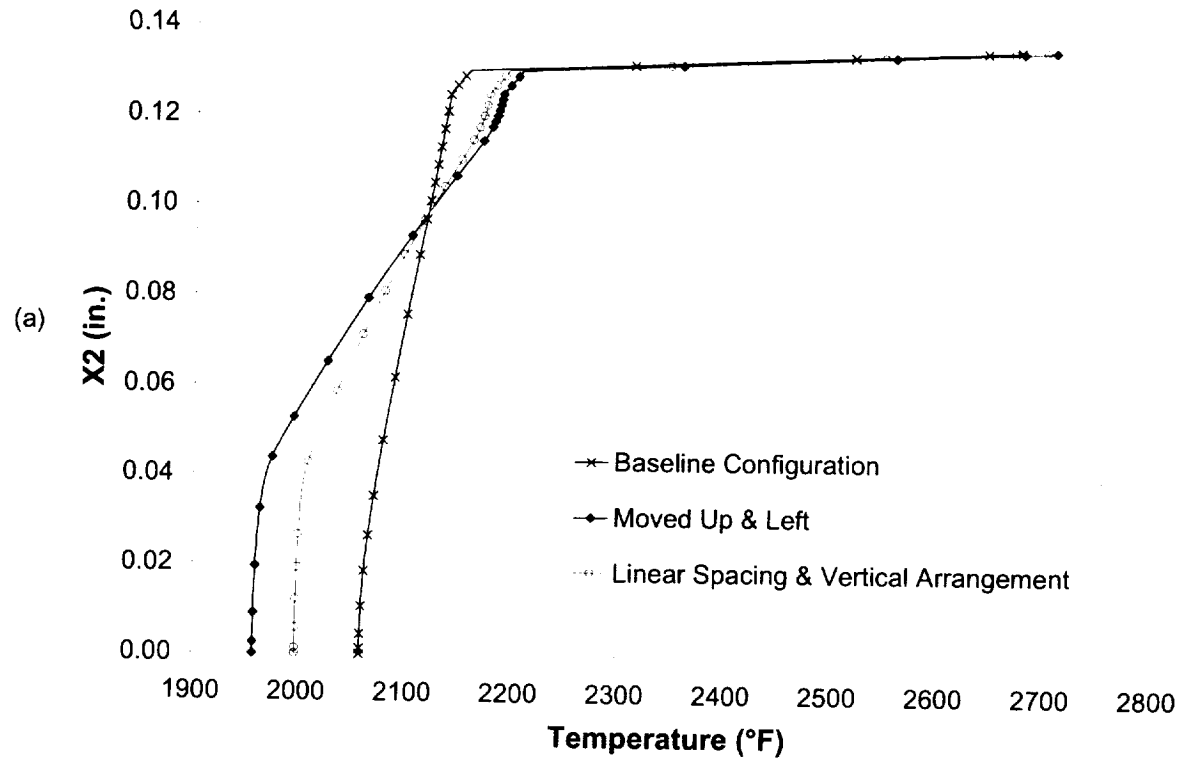


Figure 38: (a) Through-thickness temperature under flame, (b) Temperature along top and bottom of plate. Effect of horizontal and vertical channel arrangement is illustrated.

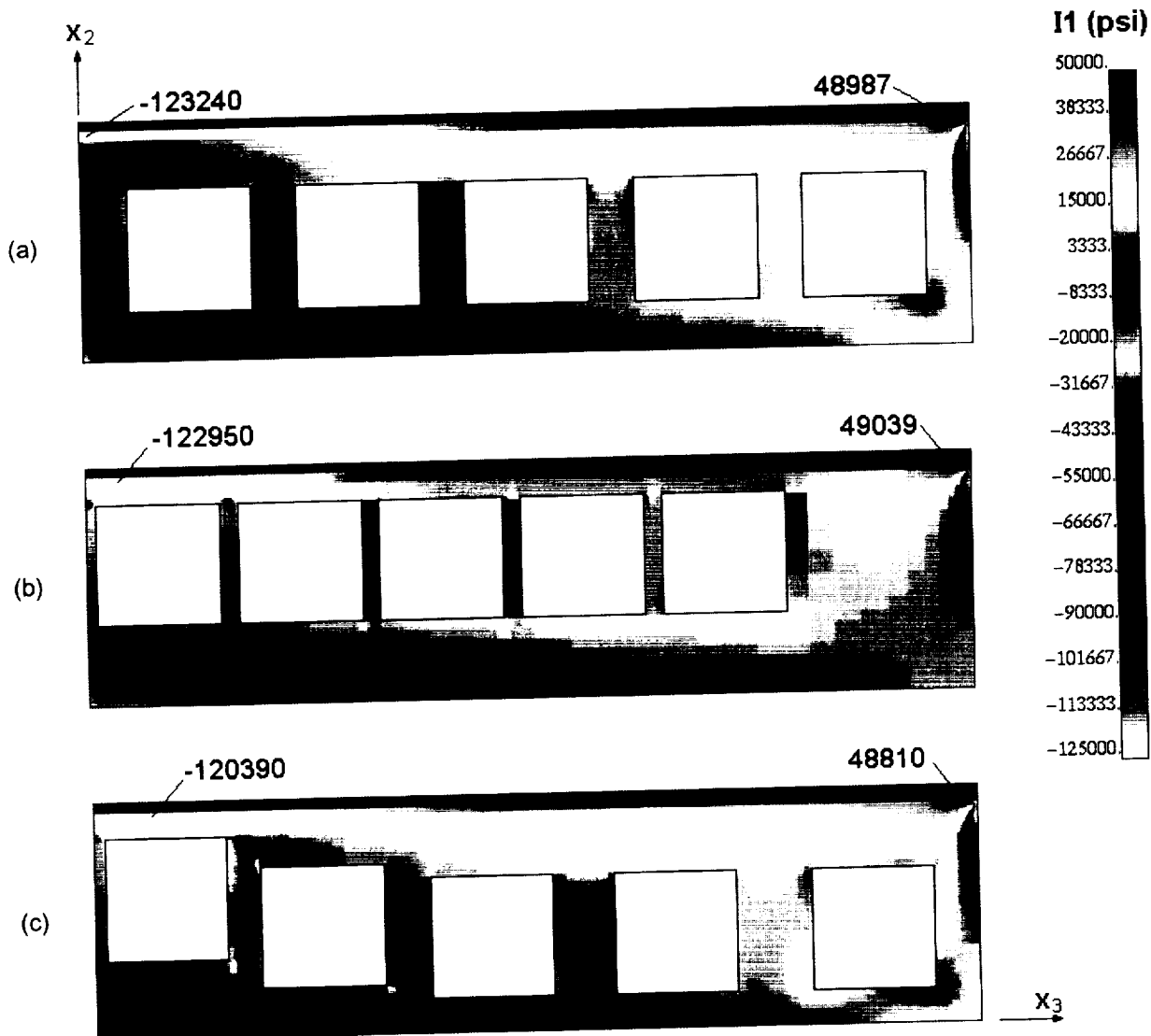


Figure 39: Plate I_1 stress invariant fields for (a) baseline configuration, (b) cooling channels shifted up and to the left, and (c) cooling channels arranged both horizontally and vertically.

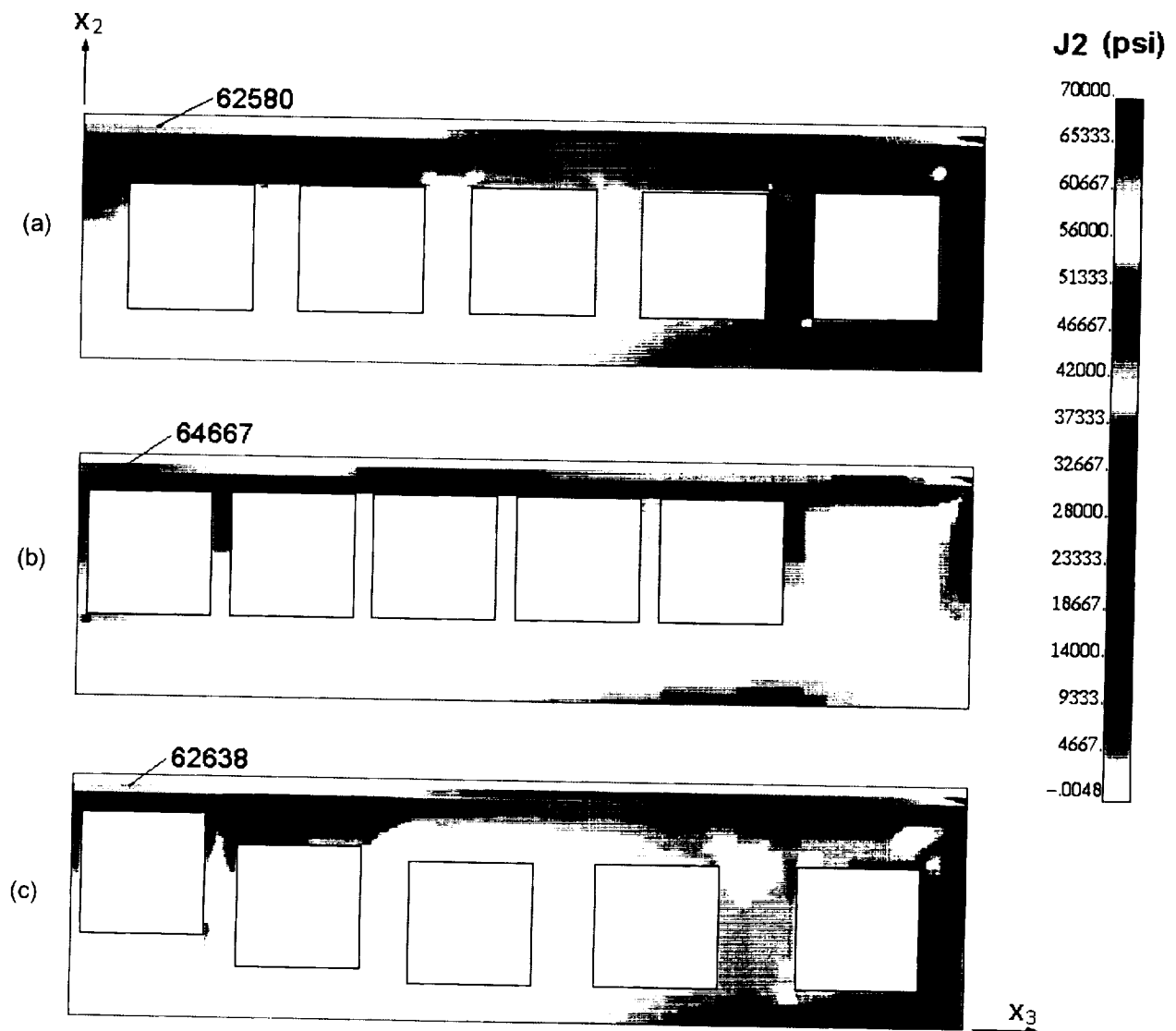


Figure 40: Plate J_2 stress invariant fields for: (a) baseline configuration, (b) cooling channels shifted up and to the left, and (c) cooling channels arranged both horizontally and vertically.

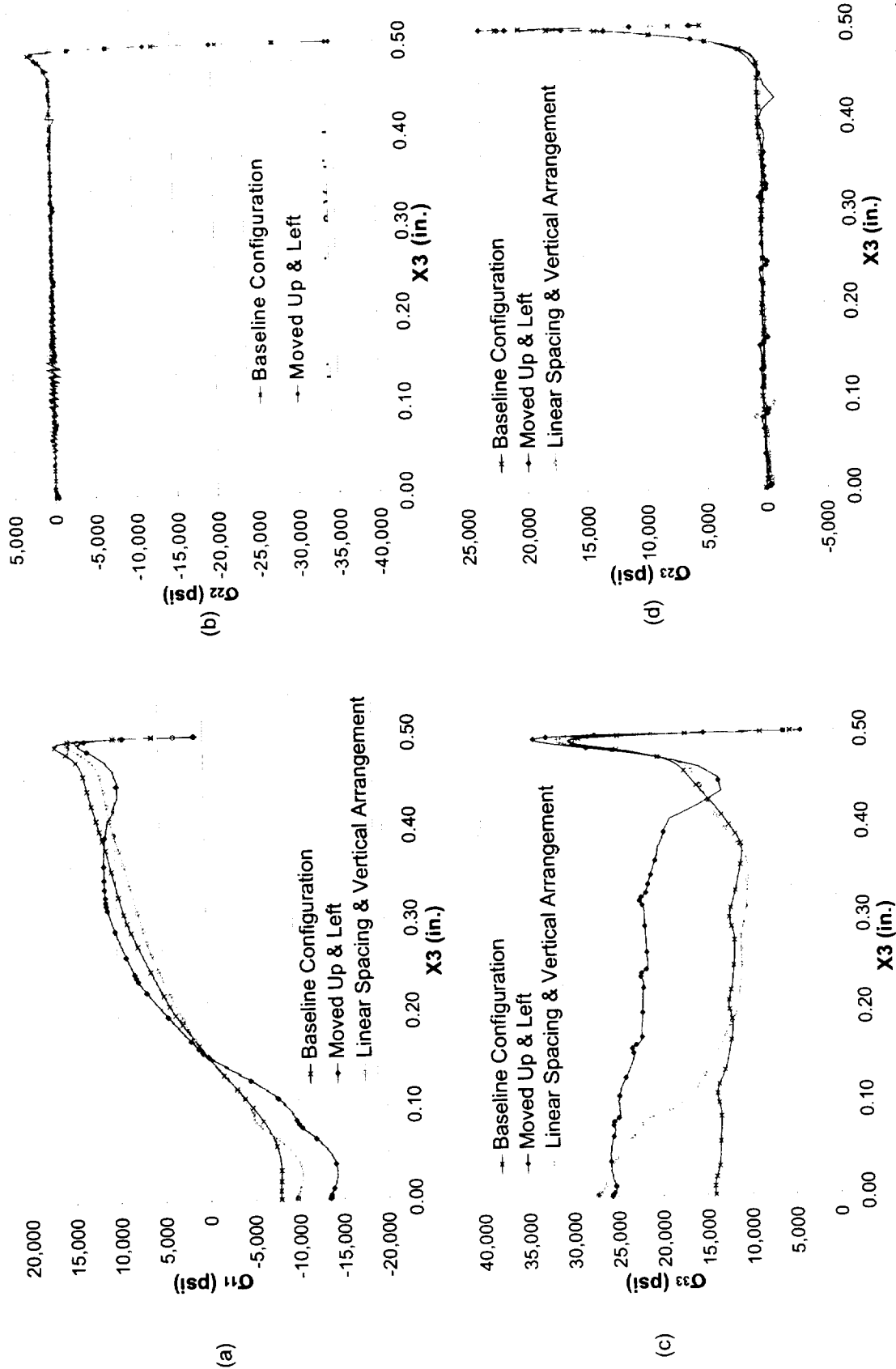


Figure 41: (a) σ_{11} in substrate along substrate/bondcoat interface, (b) σ_{22} in substrate along substrate/bondcoat interface, (c) σ_{33} in substrate along substrate/bondcoat interface and (d) σ_{23} in substrate along substrate/bondcoat interface. Effect of horizontal and vertical channel arrangement is illustrated.

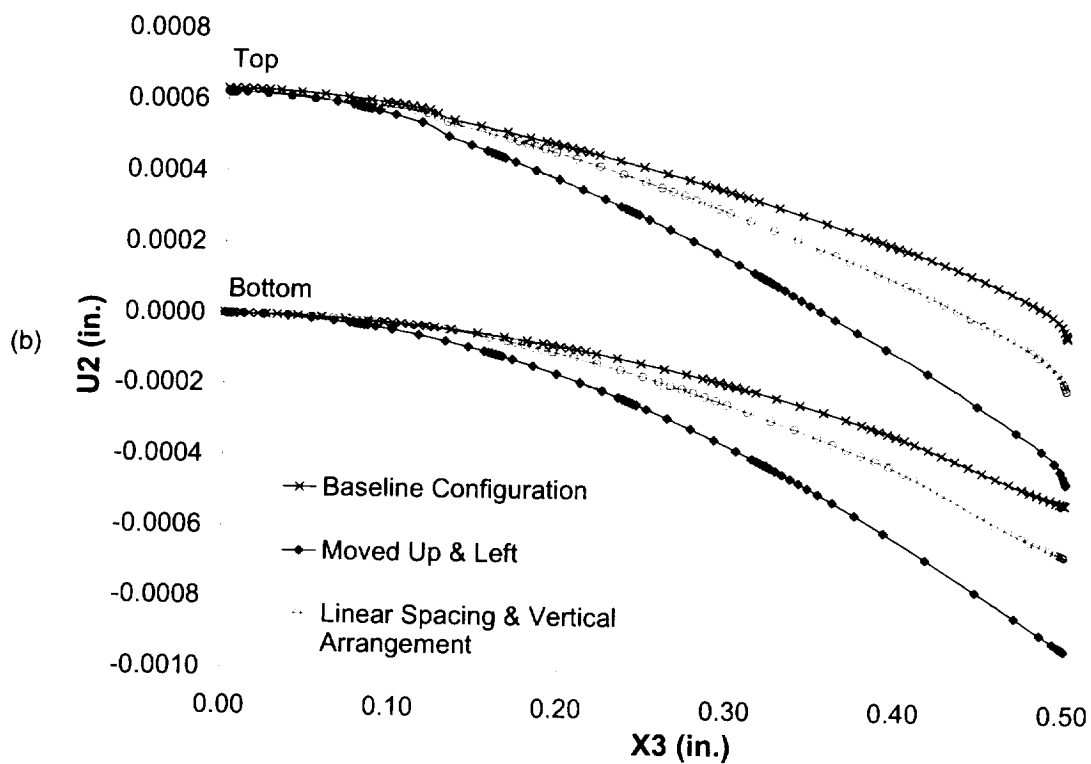
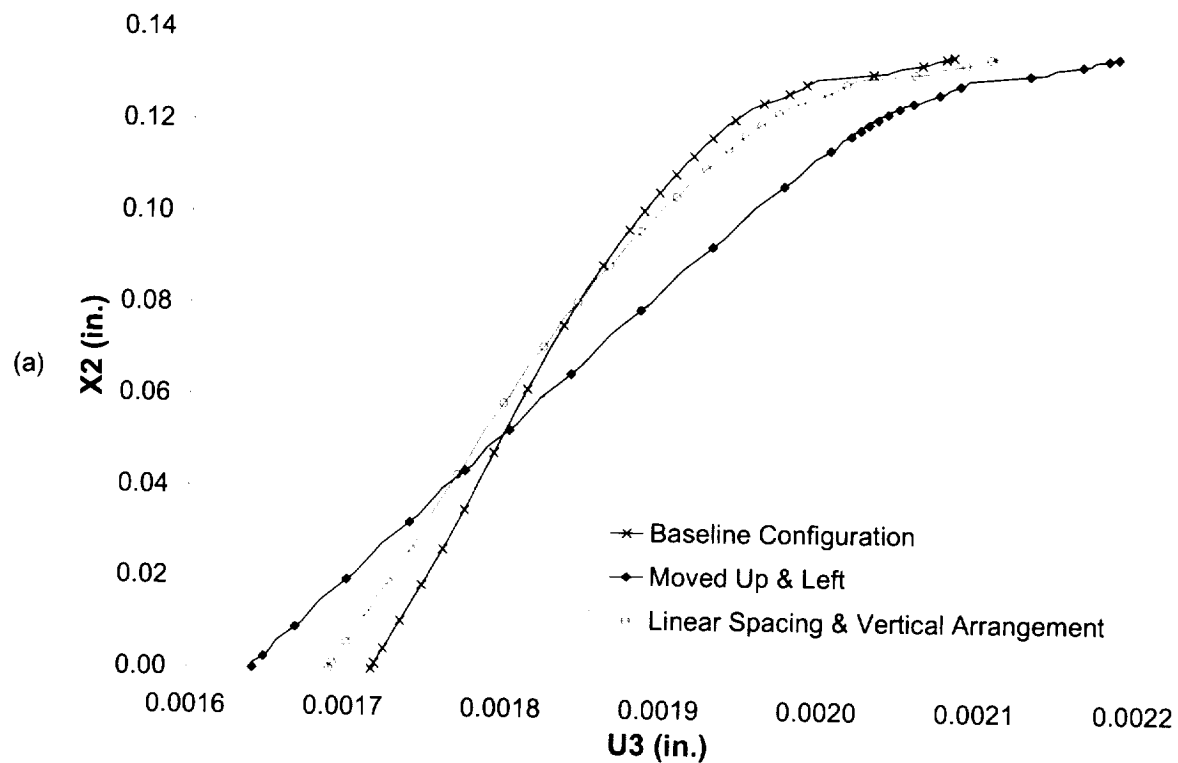


Figure 42: (a) Through-thickness x_3 -direction displacement at free edge of plate, (b) x_2 -direction displacement along top and bottom of plate. Effect of horizontal and vertical channel arrangement is illustrated.

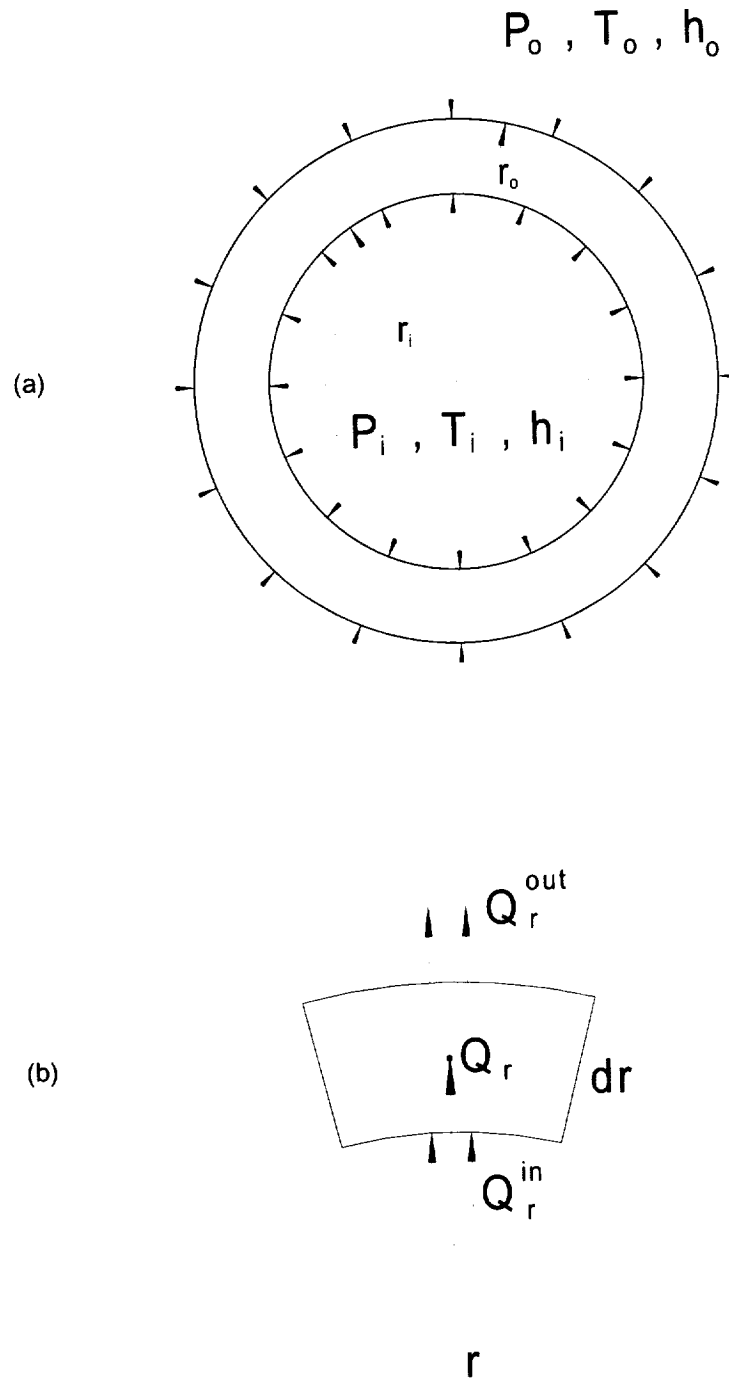


Figure 43: Analytical cylinder problem: (a) boundary conditions, and (b) differential volume element.

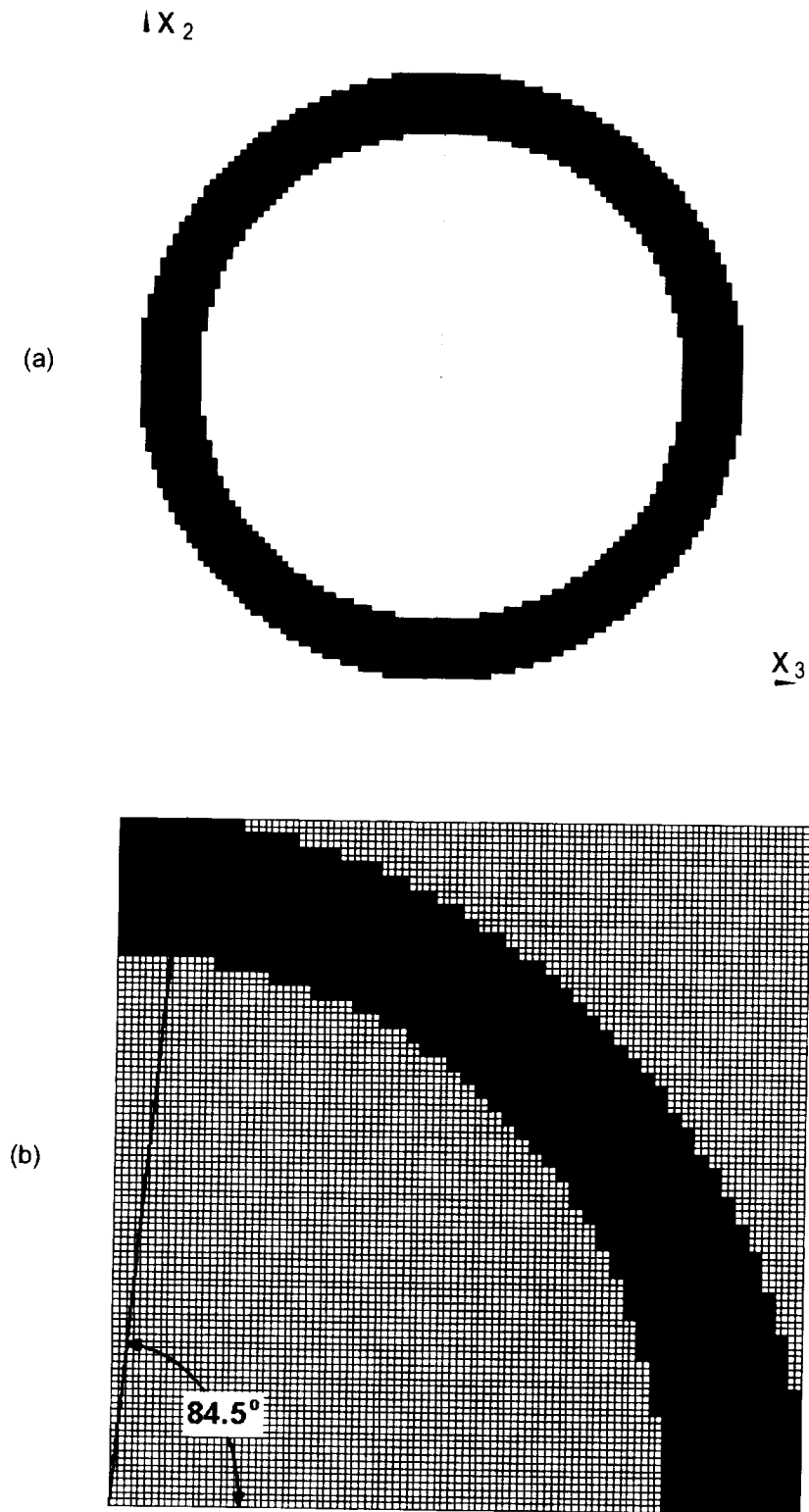


Figure 44: Idealized Cylinder HOTFGM geometry: (a) entire cylinder, and (b) 1/4 Cylinder HOTFGM analysis geometry.

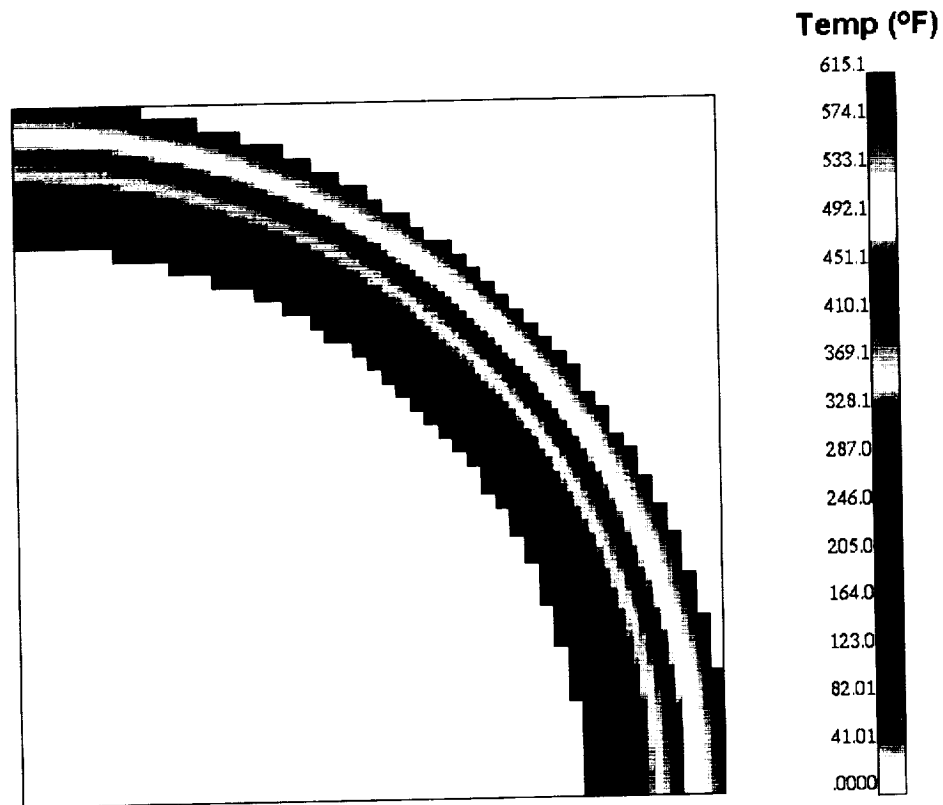


Figure 45: HOTFGM simulated temperature field in cylinder.

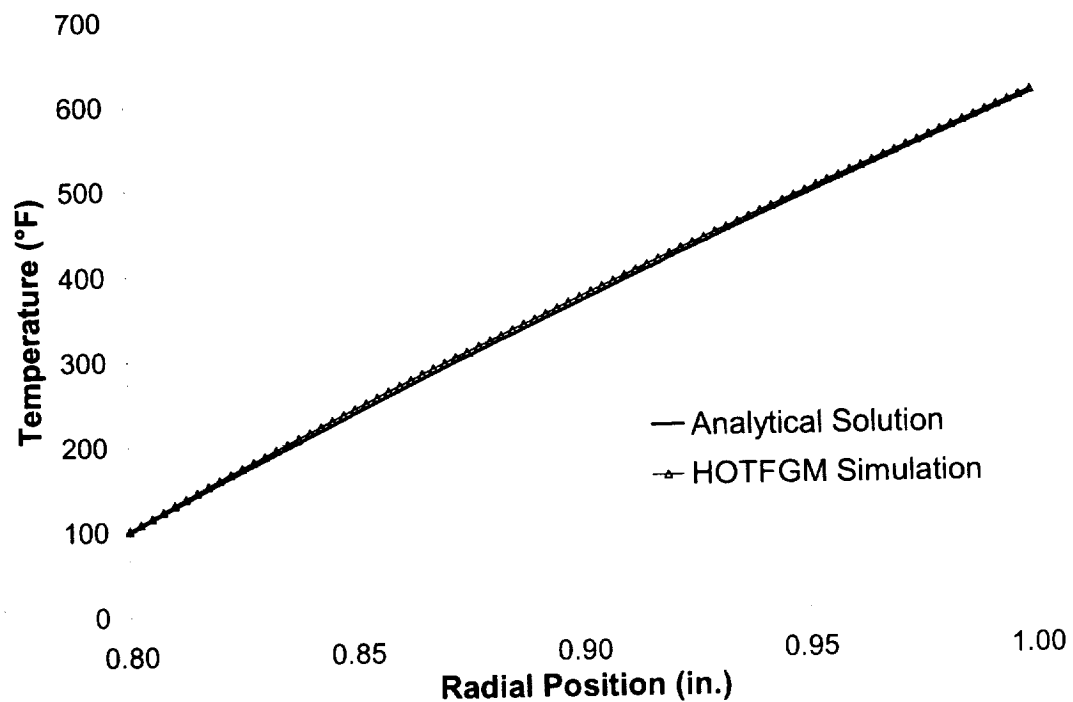


Figure 46: Comparison of the HOTFGM simulation and the analytical solution of the through-thickness temperature distribution in the cylinder.

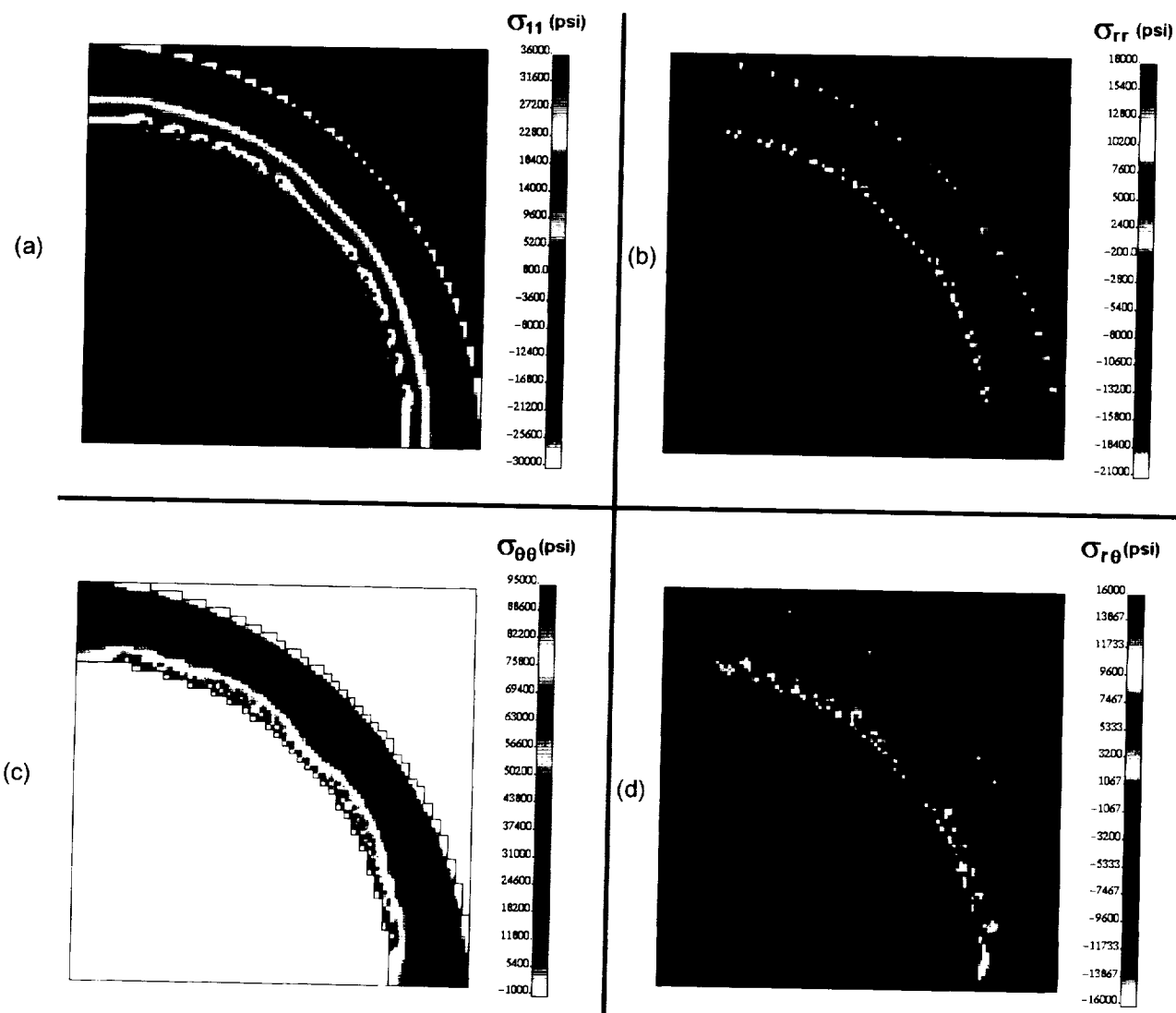


Figure 47: (a) Longitudinal, (b) radial, (c) hoop, and (d) in-plane shear stress field results within the cylinder simulated by HOTFGM.

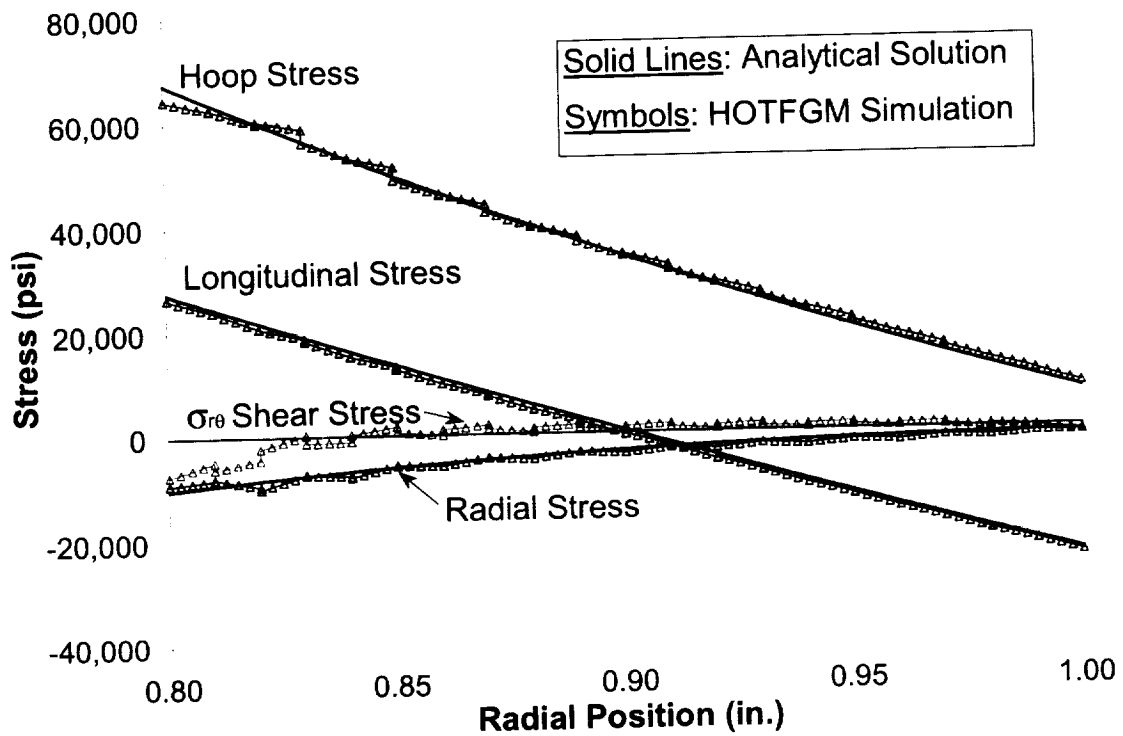


Figure 48: Comparison of the HOTFGM simulation and the analytical solution for through-thickness temperature distribution in the cylinder.

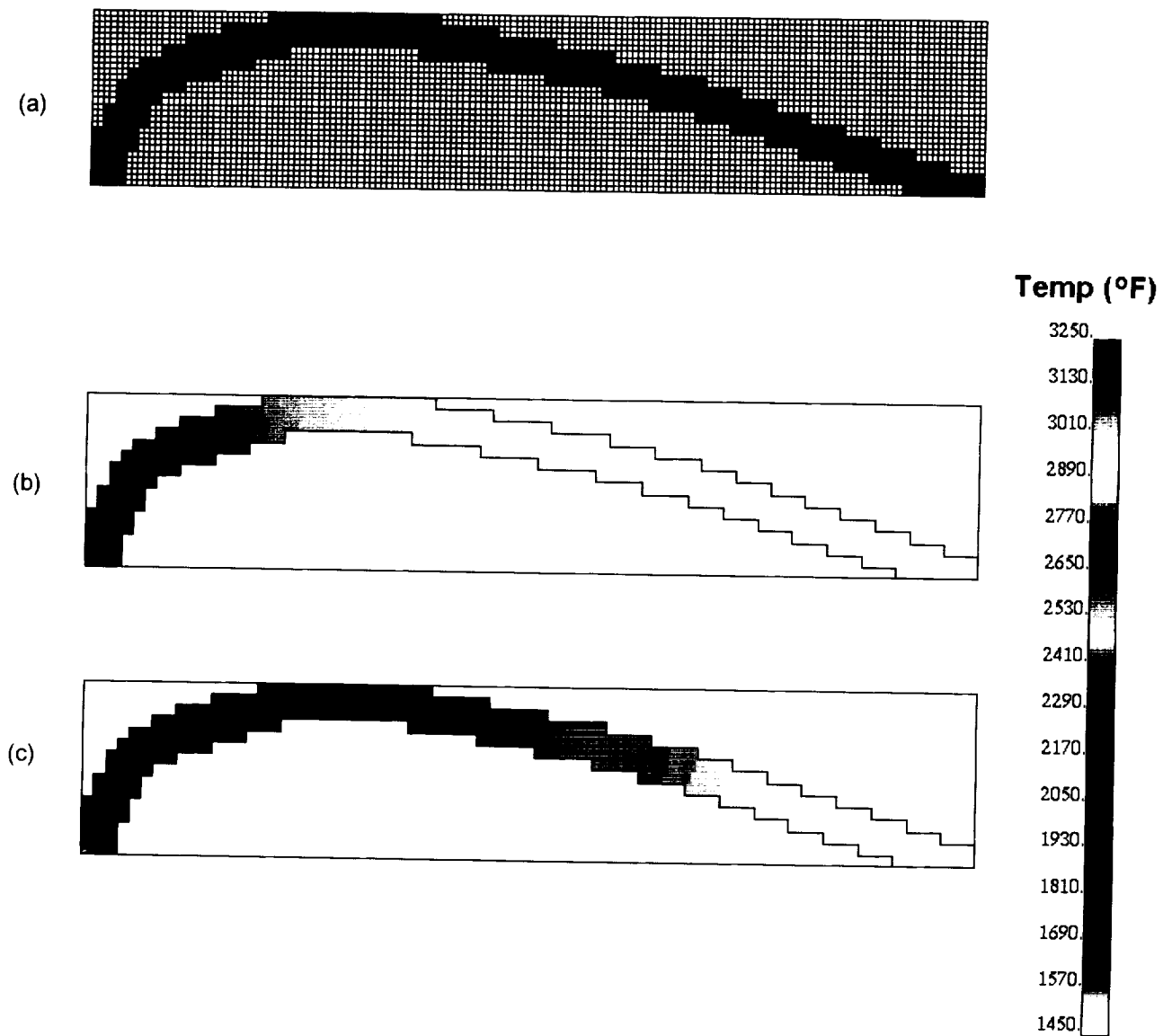


Figure 49: HOTFGM simulation of an airfoil cross-section. (a) Subcell grid, (b) simulated temperature field with no internal cooling, and (c) simulated temperature field with internal cooling.

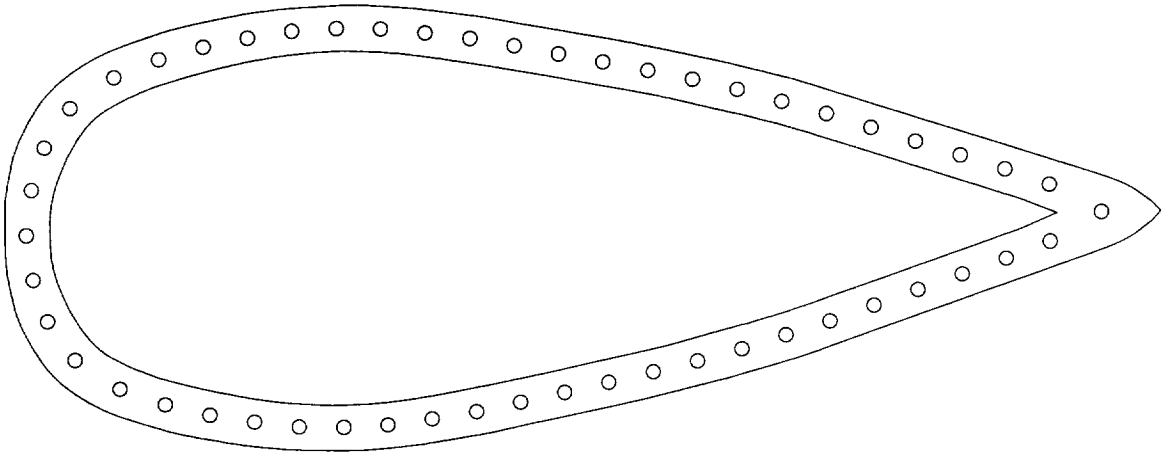


Figure 50: Diagram of an airfoil with inter-wall cooling channels that could be modeled using HOTFGM.

REPORT DOCUMENTATION PAGE			Form Approved OMB No. 0704-0188	
Public reporting burden for this collection of information is estimated to average 1 hour per response, including the time for reviewing instructions, searching existing data sources, gathering and maintaining the data needed, and completing and reviewing the collection of information. Send comments regarding this burden estimate or any other aspect of this collection of information, including suggestions for reducing this burden, to Washington Headquarters Services, Directorate for Information Operations and Reports, 1215 Jefferson Davis Highway, Suite 1204, Arlington, VA 22202-4302, and to the Office of Management and Budget, Paperwork Reduction Project (0704-0188), Washington, DC 20503.				
1. AGENCY USE ONLY (Leave blank)	2. REPORT DATE January 2001	3. REPORT TYPE AND DATES COVERED Technical Memorandum		
4. TITLE AND SUBTITLE Thermo-Elastic Analysis of Internally Cooled Structures Using a Higher Order Theory		5. FUNDING NUMBERS WU-708-31-13-00		
6. AUTHOR(S) Steven M. Arnold, Brett A. Bednarczyk, and Jacob Aboudi				
7. PERFORMING ORGANIZATION NAME(S) AND ADDRESS(ES) National Aeronautics and Space Administration John H. Glenn Research Center at Lewis Field Cleveland, Ohio 44135-3191		8. PERFORMING ORGANIZATION REPORT NUMBER E-12633		
9. SPONSORING/MONITORING AGENCY NAME(S) AND ADDRESS(ES) National Aeronautics and Space Administration Washington, DC 20546-0001		10. SPONSORING/MONITORING AGENCY REPORT NUMBER NASA TM-2001-210702		
11. SUPPLEMENTARY NOTES Steven M. Arnold, NASA Glenn Research Center; Brett A. Bednarczyk, Ohio Aerospace Institute, 2001 Aerospace Parkway, Brook Park, Ohio 44142; and Jacob Aboudi, Tel-Aviv University, Tel-Aviv, Israel. Responsible person, Steven M. Arnold, organization code 5920, 216-433-3334.				
12a. DISTRIBUTION/AVAILABILITY STATEMENT Unclassified - Unlimited Subject Categories: 39 and 24 Available electronically at http://gltrs.grc.nasa.gov/GLTRS This publication is available from the NASA Center for AeroSpace Information, 301-621-0390.			12b. DISTRIBUTION CODE	
13. ABSTRACT (Maximum 200 words) This paper presents the results of a study on the thermomechanical behavior of internally cooled silicon nitride structures. Silicon nitride is under consideration for elevated temperature aerospace engine applications, and techniques for lowering the operating temperature of structures composed of this material are under development. Lowering the operating temperature provides a large payoff in terms of fatigue life and may be accomplished through the use of thermal barrier coatings (TBC's) and the novel concept of included cooling channels. Herein, an in-depth study is performed on the behavior of a flame-impinged silicon nitride plate with a TBC and internal channels cooled by forced air. The analysis is performed using the higher order theory for functionally graded materials (HOTFGM), which has been developed through NASA Glenn Research Center funding over the past several years. HOTFGM was chosen over the traditional finite element approach as a prelude to an examination of functionally graded silicon nitride structures for which HOTFGM is ideally suited. To accommodate the analysis requirements of the internally cooled plate problem, two crucial enhancements were made to the two-dimensional Cartesian-based version of HOTFGM, namely, incorporation of internal boundary capabilities and incorporation of convective boundary conditions. Results indicate the viability and large benefits of cooling the plate via forced air through cooling channels. Furthermore, cooling can positively impact the stress and displacement fields present in the plate, yielding an additional payoff in terms of fatigue life. Finally, a spin-off capability resulted from inclusion of internal boundaries within HOTFGM; the ability to simulate the thermo-elastic response of structures with curved surfaces. This new capability is demonstrated, and through comparison with an analytical solution, shown to be viable and accurate.				
14. SUBJECT TERMS Thermal analysis; Deformation; Elasticity; Ceramics; Parametric study			15. NUMBER OF PAGES 80	
			16. PRICE CODE A05	
17. SECURITY CLASSIFICATION OF REPORT Unclassified	18. SECURITY CLASSIFICATION OF THIS PAGE Unclassified	19. SECURITY CLASSIFICATION OF ABSTRACT Unclassified	20. LIMITATION OF ABSTRACT	